National Technnical University of Athens
School of Mechanical Engineering
Parallel CFD & Optimization Unit

Prediction of Aerodynamically Induced Noise in Automotive HVAC Systems

Diploma Thesis

Konstantinos Mikedis

Academic Supervisor:
Kyriakos C. Giannakoglou, Professor NTUA

Industrial Supervisor:
Antoine Delacroix, Manager TME

Athens, February 2023

Acknowledgements

Arriving at the completion of my thesis, which also marks for me the end of a long chapter, I would like to thank those people who helped make it possible.

First and foremost I would like to express my gratitude to professor Kyriakos Giannakoglou, for giving me the opportunity to conduct my diploma thesis project as part of an industrial internship. I thank him for being always available to discuss the progress of my work, for his continuous advice and the meticulous proofreading of the thesis text.

I feel the need to thank everyone I had the chance to work with during my internship at Toyota, starting with my manager Antoine Delacroix whose experience and pragmatic judgement have been greatly contributing factors to the completion of my project. Special thanks goes to graduate engineer George Smyrlis, who was there from the beginning, on a daily basis, to provide feedback and discuss the progress of my work. I would also like to thank senior engineer Pablo Fernandez, for his valuable help and suggestions.

I would also like to thank Dr. Evangelos Papoutsis-Kiachagias, member of the PCOpt/NTUA research team, for investing his valuable time in providing me with technical support, regarding OpenFOAM.

I could not conclude this segment without mentioning my friends and family, who have stood by me, in good and bad, for the duration of my studies. Each of them has contributed their part in making for a nice journey. Τους ευχαριστώ.

National Technical University of Athens
School of Mechanical Engineering
Parallel CFD & Optimization Unit

Prediction of Aerodynamically Induced Noise in Automotive HVAC Systems

Diploma Thesis

Konstantinos Mikedis

Academic Supervisor: Kyriakos C. Giannakoglou, Professor NTUA

Industrial Supervisor: Antoine Delacroix, Manager TME

Athens, February 2023

Abstract

The progress towards quieter passenger vehicles has given prominence to sources of acoustic annoyance in the cabin previously considered irrelevant, as is the case with Heating Ventilation and Air Conditioning (HVAC) systems. This has led automotive manufacturers to explore numerical methods for noise prediction, with the potential to be incorporated into the design process of such systems, offering an assessment of acoustic performance at a development stage.

A significant portion of HVAC-generated noise is the aerodynamic sound generated by the unsteady flow inside its components, on which the present work focuses, for which numerical prediction falls under the scope of computational aeroacoustics. It is especially challenging since it deals with two physical disciplines of different natures, that is acoustics and fluid mechanics. Numerical approaches to such problems usually fall into two categories, direct ones, treating both physical disciplines using the same global model, and hybrid ones, treating flow and acoustics separately, with models tailored to each.

In this work, a direct approach was implemented, based on compressible unsteady computational fluid dynamics (CFD), to resolve simultaneously, on the same domain, both sound propagation and the flow responsible for its generation. For that matter, the OpenFOAM® CFD toolbox was used, in addition to utilities, developed in the Python™ programming language, for post-processing the acoustic signals computed via unsteady CFD.

To evaluate the accuracy of the proposed direct numerical method, a benchmark case is adopted based on production HVAC ducts. A real-world measurement setup is devised and implemented, on which noise measurements are performed emulating different operating conditions.

The direct method is first applied to a simplified HVAC case adopted from literature, followed by the aforementioned production case. Numerical sound predictions show an acceptable correlation with experimental values and other published works.

A major part of the work for the present thesis was carried out during a six-month long internship at Toyota Motor Europe (TME) in Brussels, Belgium.

Εθνικό Μετσόβιο Πολυτεχνείο
Σχολή Μηχανολόγων Μηχανικών
Μονάδα Παράλληλης Υπολογιστικής Ρευστοδυναμικής & Βελτιστοποίησης

Πρόλεξη Αεροδυναμικά Επαγόμενου Θορύβου σε Συστήματα Κλιματισμού Αυτοκινήτων

Διπλωματική εργασία

Κωνσταντίνος Μικέδης

Ακαδημαικός Επιβλέπων: Κυριάκος Χ. Γιαννάκογλου, Καθηγητής ΕΜΠ

Βιομηχανικός Επιβλέπων: Antoine Delacroix, Manager TME

Αθήνα, Φεβρουάριος 2023

Περίληψη

Η συνεχόμενη βελτίωση της ακουστικής συμπεριφοράς των επιβατικών αυτοκινήτων φέρνει στο προσκήνιο πηγές ηχητικής όχλησης μικρής, μέχρι τώρα, σημασίας, όπως τα συστήματα κλιματισμού. Αποτέλεσμα, το ενδιαφέρον πολλών αυτοκινητοβιομηχανιών για υπολογιστικές μεθόδους πρόβλεψης θορύβου, ικανών να προσφέρουν χρήσιμες πληροφορίες για τα χαρακτηριστικά τέτοιων συστημάτων, ακόμα και κατά τη φάση σχεδιασμού.

Σημαντικό μέρος του παραγόμενου θορύβου σε συστήματα κλιματισμού οφείλεται στη ροή αέρα εντός τους, και στον επαγόμενο ήχο από αυτή, όπου εστιάζεται και η παρούσα διπλωματική εργασία. Η μελέτη και προσομοίωση αυτού του αντικειμένου υπάγεται στον κλάδο της Υπολογιστικής Αεροακουστικής και είναι ιδιαίτερα απαιτητική, καθώς πραγματεύεται δύο διαφορετικούς φυσικούς μηχανισμούς σε σύζευξη, ήτοι την ακουστική και την αεροδυναμική. Οι υπολογιστικές μέθοδοι πρόβλεψης αεροδυναμικά επαγόμενου ήχου χωρίζονται σε δύο γενικές κατηγορίες, τις άμεσες (direct) μεθόδους, στις οποίες οι δύο κλάδοι αντιμετωπίζονται από κοινού, με το ίδιο μοντέλο, και στις υβριδικές (hybrid), στις οποίες ακουστική και αεροδυναμική επιλύονται με εξειδικευμένα μοντέλα καθεμιά.

Στην παρούσα εργασία υλοποιείται μία άμεση προσέγγιση, βασισμένη σε μεθόδους Υπολογιστικής Ρευστοδυναμικής για συμπιεστές μη-μόνιμες ροές, για την ταυτόχρονη επίλυση, σε κοινό υπολογιστικό χωρίο, της ροής που είναι υπεύθυνη για την παραγωγή και τη διάδοση του ήχου. Για αυτόν τον σκοπό, γίνεται χρήση του ανοιχτού λογισμικού OpenFOAM® και υπολογιστικών εργαλείων που αναπτύχθηκαν σε γλώσσα Python™, τα δεύτερα για τη μετα-επεξεργασία των ηχητικών σημάτων που υπολογίζονται από την επίλυση των χρονικά μ-μόνιμων εξισώσεων ροής.

Με στόχο την αξιολόγηση των αριθμητικών προβλέψεων, προτείνεται και υλοποιείται μια πειραματική διάταξη για τη λήψη ηχητικών μετρήσεων σε αγωγούς συστημάτων κλιματισμού επιβατικών αυτοκινήτων. Μέσω αυτής, λαμβάνονται μετρήσεις σε πραγματικό αγωγό αυτοκινήτου, εξομοιώνοντας διαφορετικές καταστάσεις λειτουργίας.

Η προτεινόμενη αριθμητική μέθοδος εφαρμόζεται πρώτα σε μία απλοποιημένη γεωμετρία αγωγού κλιματισμού εκ της βιβλιογραφίας και ύστερα στην προαναφερθείσα πραγματική γεωμετρία. Τα παραγόμενα αποτελέσματα παρουσιάζουν συσχέτιση με τα αντίστοιχα πειραματικά.

Το μεγαλύτερο μέρος του έργου για την εκπόνηση της παρούσας εργασίας πραγματοποιήθηκε κατά την εξάμηνη πρακτική άσκηση στην Toyota Motor Europe (TME) στις Βρυξέλλες.

Contents

Abbreviations

BEVs	Battery Electric Vehicles
CAA	Computational Aeroacoustics
CFD	Computational Fluid Dynamics
DFT	Discrete Fourier Transform
DNC	Direct Noise Computation
EVs	Electric Vehicles
HEVs	Hybrid Electric Vehicles
FEM	Finite Element Method
FVM	Finite Volume Method
HVAC	Heating Ventilation and Air-Conditioning
(ID)DES	(Improved Delayed) Detached Eddy Simulation
LBM	Lattice-Boltzmann
LES	Large Eddy Simulation
LHS	Left-Hand Side
N-S	Navier-Stokes
NTUA	National Technical University of Athens
PCOpt	Parallel CFD & Optimization Unit
PSD	Power Spectral Density
RANS	Reynolds-Averaged Navier-Stokes
RHS	Right-Hand Side
SPL	Sound Pressure Level
TKE	Turbulent Kinetic Energy
TME	Toyota Motor Europe
w.r.t.	with respect to

Chapter 1

Introduction

In recent times, an increasing focus of automotive manufacturers on improving the noise performance of their production vehicles is being observed [1, 2]. Following a general trend towards more efficient and quieter internal combustion engine technology and amid the noticeable proliferation of electric vehicles (EVs) in some parts of the world, reducing sources of acoustic annoyance in passenger vehicles is becoming ever more important for perceived vehicle quality [1].

From the perspective of passenger experience, such sources include, but are not limited to, powertrain, exhaust, Heating Ventilation and Air-Conditioning (HVAC), external wind and road noise [2]. Regarding the HVAC system and, specifically, in the case of EVs such as Battery Electric Vehicles (BEVs) and Hybrid Electric Vehicles (HEVs), there are situations where it might constitute the dominant source of interior noise, notably when the vehicle is stationary (fig. 1.1). Therefore, aiming at reducing the HVAC system's noise emissions inside the cabin becomes an essential part of EV development.

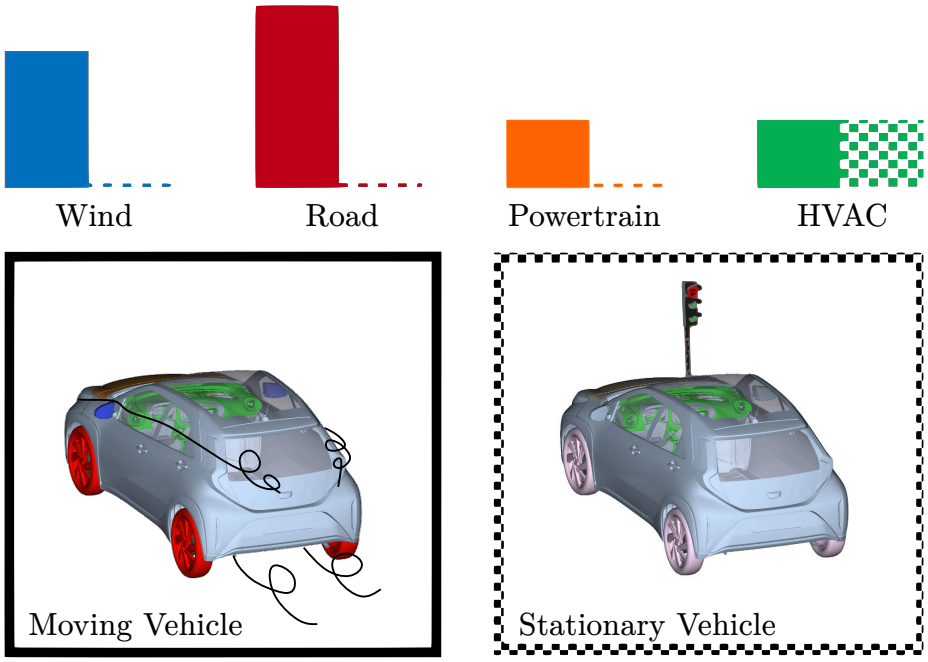

Figure 1.1: Rough estimate of EV Cabin noise composition on moving (left) and stationary (right) vehicles. HVAC Noise stays practically unchanged in both conditions. (from TME)

1.1 Vehicle cabin HVAC noise

As a first step towards optimizing vehicle HVAC acoustic performance, a method for its accurate prediction is needed. During vehicle development stages, a simulation technique for interior HVAC noise could provide early feedback to engineers and designers, before the prototype stage, thus reducing product development cycle time [3].

HVAC noise can be divided into different categories based on its nature, the most prominent of which are (fig. 1.2) [1]:

- *Aerodynamic Noise:* produced as a result of the airflow and its interactions with HVAC components
- *Harmonic noise:* generated by mechanical vibrations of components such as the blower motor, transmitted through solid parts and emitted as airborne sound inside the cabin

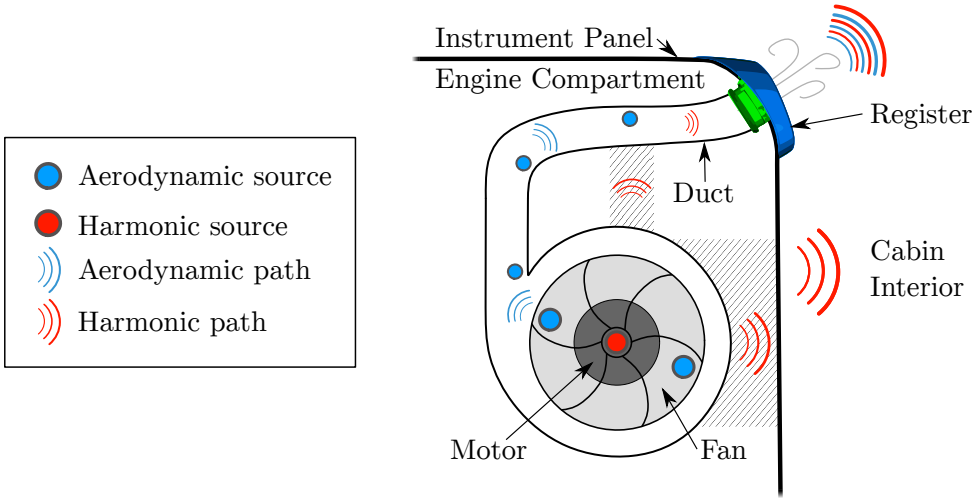

Figure 1.2: Generation of harmonic and aerodynamic noise by the HVAC unit and transmission paths towards the cabin interior. Aerodynamic noise is generated in regions where airflow is observed, inside the ducts and the fan casing, and transmitted mainly through the ducting. Harmonic noise is generated mainly by motor vibrations and transmitted through the mounting brackets and other rigid connections.

A distinction should be made between the terms *sound* and *noise*. *Sound* is used to describe pressure perturbations moving through a transmission medium in general, whereas *noise* suggests unwanted sound. In what follows, those two terms are often used interchangeably.

1.2 Aerodynamic noise in Automotive HVAC Systems

Aerodynamic sound is usually defined as sound generated by unsteady flows [4], where turbulent and vortical flow structures, caused by flow instabilities or interactions of the medium with solid bodies, generate pressure perturbations, i.e. sound, that travel

through a transmission medium [5] (fig. 1.3). In the case of air, sound propagates with a speed of around 343 $^{m}/_{s}$ at ambient conditions.

Unsteadiness in the flow can either be due to broadband turbulence, consisting of vortical structures in a wide range of length and time scales or of tonal character, with a prominent frequency, caused by vortex shedding effects or rotating components (fans, blowers etc.) [6].

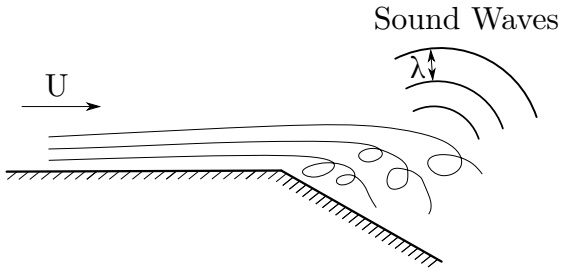

Figure 1.3: Sound generation by unsteady flow structures in the presence of solid walls.

Aerodynamic HVAC noise can further be divided into two categories, *duct flow noise* and *fan noise* [2] the former being related to the airflow inside the system's duct network, whereas the latter to rotating blower parts. Both are generally of broadband nature. *Fan noise* is also expected to contain tonal components dictated by its blade pass frequency (BPS), although, it has been shown that their contribution is usually of minimal significance [2]. Due to limiting constraints such as lack of space, the ducting system has to be as compact as possible, leading to designs with sharp angles and abrupt cross-section changes. Those features contribute significantly to unsteady phenomena in the flow, in turn, acting as sources of noise [2].

The human ear is especially sensitive to sounds of frequencies ranging from several hundred Hz to around 5 kHz (fig. 1.4). Consequently, it is rational to focus on that range, when developing a method to predict and reduce HVAC cabin noise. Since, as discussed above, HVAC noise sources are generally of a broadband nature, it is fair to assume that any meaningful reduction in noise levels would be generally uniform, unless exceptional flow structures develop, contributing to increased noise emission outside the range of focus.

The present thesis focuses solely on aerodynamic noise generated by flow interaction with stationary geometries, thus fan noise falls out of its scope.

1.3 CAA approaches for HVAC Noise - Literature Survey

Any computational aeroacoustics (CAA) approach, should be concerned both with the flow responsible for generating sound as well as its propagation. This task is inherently difficult, mainly for two reasons. First and foremost, the two disciplines exhibit greatly different characteristics, such as length and time scales [5, 9–11] (see section 3.1), especially in low-Mach numbers. Moreover, in many applications, while sound generation is concentrated in specific regions in the flow, sound propagation needs to be resolved up to the farfield [10], calling for large simulation domains.

Existing CAA methods can generally be divided into two categories (fig. 1.5) [10]:

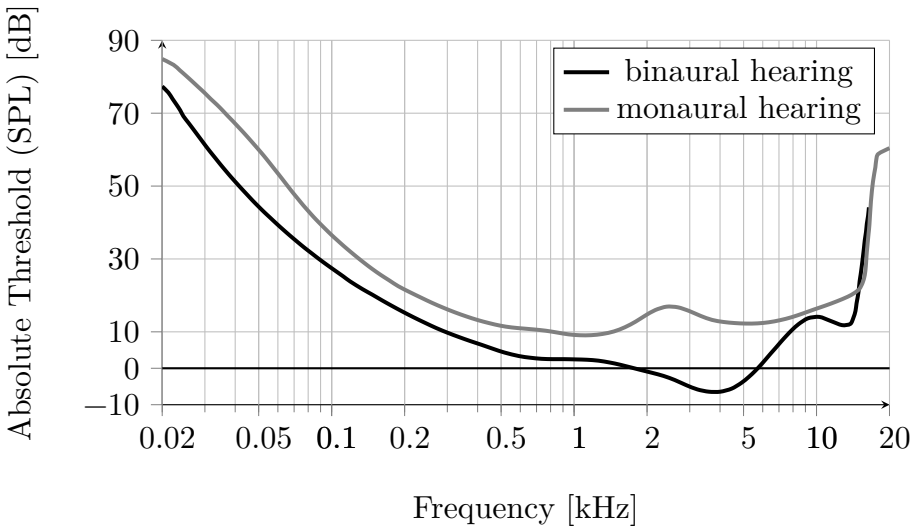

Figure 1.4: Hearing threshold as a function of frequency, for binaural (both ears) [7] and monaural (single ear) [8] hearing.

– *Direct Noise Computation* (DNC) methods (see chapter 3), employ unsteady compressible computational fluid dynamics to compute the noise-generating structures of the flow, which are inherently unsteady [11], while simultaneously resolving acoustics, allowed for by the compressible formulation. Such methods are the most accurate, since they do not use any models for sound, except in some cases a turbulence model for the flow [10]. However, their exact nature renders them computationally intensive.

– *Hybrid Methods* aim to decouple sound generation from sound propagation [11], exploiting the absence of sound-to-flow feedback in most relevant engineering applications [10], as is the case in HVAC flows. They are then treated separately, using a method tailored to the particularities of each physical discipline (flow and acoustics). The generation information is passed from the flow solution, using acoustic analogies or statistical models, to an acoustic solver, of lower cost, responsible for its propagation to the farfield. Such methods are generally more versatile and adaptable to each specific application [10], as a tradeoff for inaccuracies introduced by their governing assumptions. A brief note on such methods can be found in section 2.3.

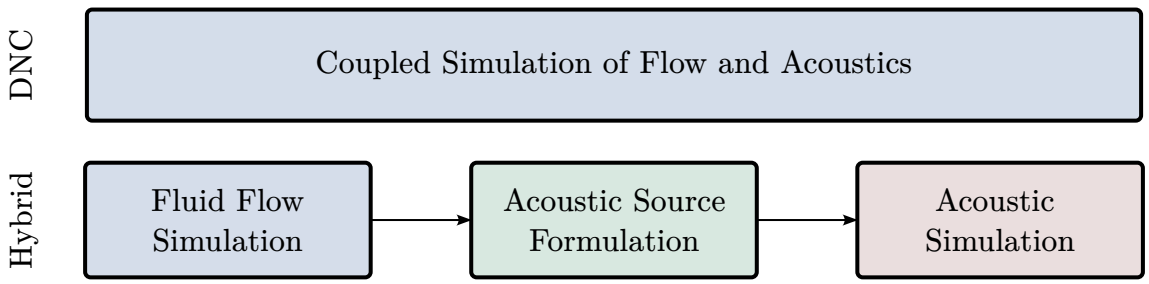

Figure 1.5: Different treatment of flow and acoustics by direct and hybrid methods.

The present work was focused on the DNC approach, which was applied to two different cases. In addition, some investigations were undertaken using Hybrid methods,

however, without any coherent results to date.

A concise summary of numerous publications in which different methods of both categories are applied can be found in the introductory chapter of [12]. In what follows, some examples of applications of DNC and Hybrid approaches in HVAC systems relevant to the present work are cited.

1.3.1 Related works on DNC

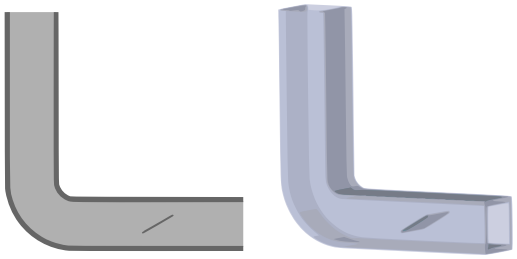

Figure 1.6: The Simplified HVAC Geometry proposed by Jäger et al. [13].

In 2008 Jäger et al. [13] performed sound and PIV measurements on a simplified HVAC geometry, which have since been used as a benchmark for various CAA-related works [14–18]. In the same publication, they managed to acquire sufficient results for the pressure fluctuations at the duct walls, using both a Finite-Volume DES and a Lattice-Boltzman (LBM) based DNC approach. Pérot et al. [18] used an LBM approach to calculate the sound at the farfield of the simplified HVAC case, while Kierkegaard et al. [14] also achieved a good prediction using an FVM LES approach. Gren et al. [19] performed a farfield noise prediction on an isolated HVAC duct of a production car, using an FVM LES approach, however without comparing the results to experimental measurements. Pérot et al. [20] extended the same LBM, method applied in [18], to the full duct network of a production car's HVAC system yielding good correlation with experimental measurements on the same geometry. Sah et al. [6] used an FVM DES approach for simulating the sound produced by flow inside a complete HVAC system, including the rotating fan, which correlated well to measurements in the near-field.

1.3.2 Related works on Hybrid Methods

In 2006, Mohamud and Johnson [21] used Broadband Noise Source (BNS) models, based on steady-state RANS-based CFD, to estimate the broadband turbulence-driven noise, using statistical models and turbulent quantities. Using this method, they proposed a redesign of an HVAC duct geometry, which significantly reduced the predicted broadband noise. However, such approaches do not provide any insight into tonal noise and are incapable of predicting sound at receiver locations [21].

Several approaches using unsteady CFD have been applied to the simplified HVAC case proposed in [13], in order to predict sound in the farfield. Caro et al. [16], based on the work of [13], used an FVM DES CFD solution to define volume-distributed sources, based on Lighthill's acoustic analogy. The acoustic propagation was then solved in the frequency domain, up to the farfield, in an FEM context. Wiart et al. [17], using a similar approach, compared methods for the coupling between the flow and acoustic problems, derived from Lighthill's and Mohring's acoustic analogies. Kierkegaard et al. [14] applied a hybrid method using an FVM approach based on acoustic perturbation equations, which were solved in the time domain, on the same mesh as the underlying incompressible CFD simultaneously with its solution, thus alleviating the need for storage and FFT conversion of flow data. Finally, Martínez-Lera et al. [15] used a hybrid approach utilizing incompressible CFD with a DDES turbulence model, from which

only the wall pressure was used to define acoustic sources, through a method based on Curle's analogy. In this scope, acoustics are modelled as a boundary value problem, based on the homogenous Helmholtz equation in the frequency domain, with tailored boundary conditions. Acoustic propagation to the farfield was then solved using both Finite-Element and Boundary-Element approaches.

1.4 Thesis Structure

The main purpose of the present thesis is to investigate the performance of CAA methods, for noise prediction in automotive HVAC systems. More specifically, it focuses on aerodynamic noise generated by the flow inside stationary components of HVAC systems and the numerical modelling of its generation and propagation. Under this scope, a DNC approach is drawn and then implemented using OpenFOAM [22] on two separate test cases. Computed results are also compared to real-world measurements, obtained through a hereby devised setup.

The present text is structured as follows:

- Chapter 2: Some key aspects of aerodynamic noise and its modelling relevant to HVAC applications are outlined. First, the fundamental properties of sound transmission in the air are discussed, thereafter focusing on low-Mach number flows, pertinent to HVAC systems. Moreover, the noise-generating character of unsteady flows is highlighted, by invoking acoustic analogies. Finally, a brief note on Hybrid Methods is made, based on preceding remarks.

- Chapter 3: The DNC Approach based on a Finite-Volume framework used for this thesis is formulated. This includes the governing equations, discretisation schemes and other considerations specific to CAA simulations using unsteady CFD for compressible fluids, such as the treatment of non-physical boundaries.

- Chapter 4: The Discrete Fourier Transform process is presented, which is used to perform analysis of sound signals from numerical and experimental investigations. On that basis, a method for extracting the acoustic components from DNC simulations is detailed, having previously commented on the need for such a method.

- Chapter 5: A new setup is proposed for measurements of aerodynamic noise on production vehicle HVAC blowers. The setup layout is illustrated and used to produce sound measurements of a production part, in different configurations, to act as a reference for DNC predictions.

- Chapter 6: The DNC approach of chapter 3 is applied first on a test case based on published research with available real-world measurements and then on the production part of chapter 5.

- Chapter 7: Conclusions are drawn from the work performed and proposals for future work on the topic are stated.

Chapter 2

Aerodynamic Noise

The present chapter discusses some key aspects of aerodynamic noise, in the scope of automotive Heating Ventilation and Air-Conditioning (HVAC) systems. In particular, a mathematical model governing airborne sound is introduced and some key aspects of noise generated by turbulent flows are discussed. Moreover, different types of aerodynamic sound sources are presented and related to specific regions of a generic HVAC duct configuration. Finally, a brief reference is made to hybrid CAA methods, and their possible applications in HVAC noise prediction.

2.1 Airborne Acoustics

The term sound is used to describe oscillations in elastic media, eg. fluids and flexible solids. In the case of fluids, sound involves time-dependent changes in density and pressure that propagate through them. Airborne acoustic disturbances are generally of small amplitude. A flow field that includes sound propagation can be interpreted as a superposition of an acoustic disturbance field (p', ρ') to an ambient state, which is the undisturbed flow state $(p_0, \rho_0, T_0, \mathrm{u}_0)$ (i.e. in the absence of said disturbances) [23],

$$p = p_0 + p' \quad \rho = \rho_0 + \rho' \tag{2.1}$$

The equation that describes the propagation of acoustic waves, in a uniform medium, assuming isentropic propagation [5] and adopting the acoustic linearization approximation, is the linear wave equation [23]:

$$\frac{\partial^2 p'}{\partial x_i^2} - \frac{1}{c^2}\frac{\partial^2 p'}{\partial t^2} = 0 \tag{2.2a}$$

$$p' = c^2 \rho', \quad c^2 = \left(\frac{\partial p}{\partial \rho}\right)_0 \tag{2.2b}$$

The speed of sound is defined in eq. (2.2b), as the partial derivative of pressure w.r.t. density, at ambient conditions. To demonstrate the physical standing of sound, the case of a single harmonic source is assumed, for which eq. (2.2a) yields the following analytical solution:

$$p' = \mathrm{Re}\left\{|P|\, e^{i[k(x-ct)+\phi_0]}\right\} \tag{2.3}$$

This expression describes the acoustic disturbance attributed to a monochromatic[1] wave, of frequency f, travelling towards the $+x$ direction of a cartesian coordinate system.

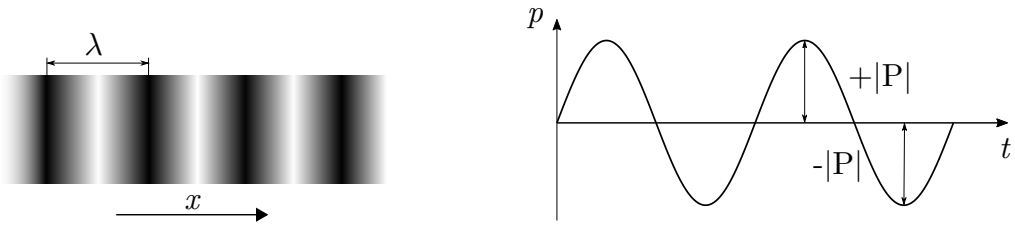

Figure 2.1: Monochromatic plane wave propagating towards the $+x$ direction (left) and acoustic pressure time series at a specific x location along the propagation path (right).

Figure 2.1 shows the successive regions of compression and detension of the fluid, which are manifested as regions of high and low pressure and density respectively. k denotes the wavenumber, defined as:

$$k = \frac{2\pi}{\lambda}$$

with λ being the acoustic wavelength. The relation between the speed of propagation c, the wavelength λ and the acoustic frequency f follows:

$$\lambda = \frac{c}{f} \tag{2.4}$$

Furthermore, the complex acoustic amplitude can be defined, as:

$$\tilde{p}' = |P|\, e^{i(kx+\phi_0)} \tag{2.5}$$

wherein $|P|$ is the amplitude of the pressure disturbance, and ϕ_0 the initial phase constant.

A useful way to quantify sound, i.e. the pressure fluctuations observed at any point in space, is the Sound Pressure Level (SPL) scale[2], which is logarithmic, and measured in decibels [4, 24, 25]. This is given by:

$$\mathrm{SPL(dB)} = 20 \log_{10}\left(\frac{p_{rms}}{p_{ref}}\right) \tag{2.6}$$

It is defined using the acoustic root-mean-squared (RMS) pressure (2.7a) and a reference pressure, the latter being equal to 2×10^{-5} Pa for measurements in the air [24, 25]. The RMS pressure is defined as the square root of the mean squared pressure [25]:

$$p_{rms} = \sqrt{\overline{p^2}} \tag{2.7a}$$

$$\overline{p^2} = \lim_{T\to\infty}\left[\frac{1}{T}\int_{t_0}^{t_0+T} {p'}^2(t)\, dt\right] \tag{2.7b}$$

[1] Consisting of a single frequency component.

[2] When this metric is used to characterise the overall pressure fluctuations at one receiver, not distinguishing between different frequency components, the Overall Sound Pressure Level (OSPL) notation is commonly used.

In the case of a monochromatic harmonic plane sound wave, such as the one depicted in fig. 2.1, acting as the sole sound source, the p_{rms} value equals $\sqrt{0.5|P|^2} \approx 0.707|P|$, where $|P|$ stands for the wave's pressure amplitude.

SPL measures are appropriate for comparing different sound measurements, due to their logarithmic nature, since p_{rms} values usually exhibit a wide range of orders of magnitude. Another feature, which can be derived easily from eq. (2.6), is that doubling the acoustic amplitude will result in an increase of approximately 6 dB in the SPL scale, regardless of the absolute value.

2.2 Aerodynamic Noise in Low Mach Number Flows

Flows in HVAC systems, exhibit Mach numbers in the range of 0 to 0.05, therefore they can be characterized as low Mach. Furthermore, due to complex geometry and the presence of rotating parts, such flows are in the fully turbulent regime. These two attributes are relevant when attempting to perform aeroacoustic simulations, as they dictate the physical length scales involved.

As shown by A. N. Kolmogorov [26], the ratio of the largest L to the smallest η turbulent length scales, in locally isotropic turbulence, follows

$$\frac{L}{\eta} \sim \mathrm{Re}^{3/4} \tag{2.8}$$

By invoking Taylor's hypothesis for turbulent time scales, the eddy passing frequency, which can act as an approximation to a representative eddy frequency, can be derived as $f = U_c/l$, where U_c the convective flow velocity and l the turbulent length scale. Owing to (2.8) and given the coincidence[3] of the eddies frequency (U_c/l) with the sound frequency (c/λ) generated by said eddies [5, 10], a correlation of the flow Reynolds number with the aerodynamic sound bandwidth becomes evident. In other words, higher Reynolds number flows, result, in general, in a broader bandwidth of aerodynamic sound [5].

Since the acoustic wavelength is dictated by the frequency and the speed of sound through the known formula $c = f\lambda$, while the turbulent length follows $U_c = fl$, a discrepancy arises between the length scales of the two disciplines in question, namely acoustics and hydro/aerodynamics. It can be shown that the ratio of acoustic wavelength λ to the turbulent length scale l pertaining to its generating mechanism, is inversely proportional to the flow Mach number [4, 5, 9, 10]:

$$\frac{\lambda}{l} \sim \mathrm{M}^{-1} \tag{2.9}$$

As a result, any numerical approach aiming at capturing the sound generated and emitted by turbulent low Mach number flows should be able to resolve a wide range of flow length scales, while accurately resolving acoustic propagation, which involves much larger length scales.

[3] Such an assumption is not always true, as shown in [5], however, it is invoked here for proof of concept.

2.2.1 Lighthill's acoustic analogy

In 1952 Lighthill proposed an equation to describe the process of sound generation in a region of turbulent flow. [5, 27]. Lighthill's wave equation (2.10), as it is known, is derived directly from the Navier-Stokes equations. It is often called *Lighthill's acoustic analogy* because it treats the sound-generating region as if it contains sound waves propagating as though they were in the surrounding undisturbed fluid [5]. This is expressed by the global use of the far-field speed of sound c_∞ as the propagation velocity, in

$$\frac{\partial^2 \rho'}{\partial t^2} - c_\infty^2 \frac{\partial^2 \rho'}{\partial x_j^2} = \frac{\partial^2 T_{ij}}{\partial x_i \partial x_j} \tag{2.10}$$

The RHS in the above expression consists of the partial spatial derivative of the Lighthill tensor, defined as

$$T_{ij} = \rho v_i v_j + (p - p_\infty) - (\rho - \rho_\infty) c_\infty^2 \delta_{ij} - \sigma_{ij} \tag{2.11}$$

where δ_{ij} denotes the Kronecker delta, σ_{ij} the **viscous** stress tensor and v_i the ith component of the velocity field. The LHS is similar to the linearized wave equation (2.2a), with the density disturbance ρ' being the dependent variable.

2.2.2 Curle's acoustic analogy

Curle [28] further extended Lighthill's theory to incorporate the effect of **stationary** solid boundaries in sound generation. Using Curle's acoustic analogy, the acoustic density fluctuations at location $\mathbf{x}$ and time t, owing to a flow field p, u_i, ρ, can be calculated using

$$\begin{aligned} \rho'(\mathbf{x},t) c_\infty^2 = & \underbrace{\iint_S \left[\frac{\partial (\rho v_j)}{\partial \tau} \right]_{\tau=\tau^*} \frac{n_j}{4\pi |\mathbf{x}-\mathbf{y}|} \, dS(\mathbf{y})}_{\text{Monopoles}} \\ & \underbrace{- \frac{\partial}{\partial x_i} \iint_S \left[p_{ij} + \rho v_i v_j \right]_{\tau=\tau^*} \frac{n_j}{4\pi |\mathbf{x}-\mathbf{y}|} \, dS(\mathbf{y})}_{\text{Dipoles}} \\ & \underbrace{+ \frac{\partial^2}{\partial x_i \partial x_j} \iiint_V \left[T_{ij}(\mathbf{y},\tau) \right]_{\tau=\tau^*} \frac{1}{4\pi |\mathbf{x}-\mathbf{y}|} \, dV(\mathbf{y})}_{\text{Quadrupoles}} \end{aligned} \tag{2.12}$$

The stationary integration volume V consists of the sound-generating flow region, whereas S includes all solid boundaries within V, as well as the external boundary of V, in case those are present. Also, n corresponds to the outward normal vector to surface S, while the stress tensor[4] is defined as $p_{ij} = (p - p_\infty)\delta_{ij} - \sigma_{ij}$. It should be noted that the integrals in eq. (2.12) are computed w.r.t. vector $\mathbf{y}$ inside the volume V and evaluated at the retarded time $\tau = \tau^* = t - |\mathbf{x} - \mathbf{y}|/c_\infty$. The difference between t and

[4] Therefore the diagonal elements denote gauge pressure, relative to p_∞.

τ is the time it takes an acoustic perturbation to travel from its generation location $\mathbf{y}$ to the receiver $\mathbf{x}$.

Curle's analogy, as presented in eq. (2.12), has been formulated assuming a direct line of sight between every point in V and receiver location $\mathbf{x}$ and ignoring any indirect sound paths due to scattering effects [5]. In more complex geometries where those assumptions are invalid, alternative formulations [15, 29–32] can be used, employing Green's functions [5, 9, 10].

2.2.3 Categorization of noise sources

The three right-hand terms of eq. (2.12), can each be considered as a separate type of sound source, namely monopole, dipole and quadrupole-type sources[5].

Monopole sound sources are dependent on the temporal variation of the flux $\rho v_j n_j$ through the integration surface S. Therefore, they can be encountered in regions of rapidly alternating volumetric flow, such as exhaust pipes and vibrating surfaces [5, 25].

Dipole sound sources depend on the loading of, and the convected momentum through, surface S $(p_{ij} + \rho v_i v_j)$. In areas where surface S expresses solid impermeable boundaries, the term $\rho v_i v_j n_j$ vanishes thus rendering the fluid-solid force the only contributor. Dipole noise sources thus arise in areas where time-varying forces are applied on solid boundaries, such as turbulent wall interactions [25].

By employing the chain rule for the spatial derivative appearing in the second term,

$$\frac{\partial f(\tau^*)}{\partial x_i} = \frac{\partial \tau^*}{\partial x_i}\left[\frac{\partial f(\tau)}{\partial \tau}\right]_{\tau=\tau^*} \tag{2.13}$$

and given that $\tau^* = t - |\mathbf{x}-\mathbf{y}|/c_\infty$,

$$\frac{\partial \tau^*}{\partial x_i} = -\frac{(x_i - y_i)}{|\mathbf{x}-\mathbf{y}|c_\infty} \tag{2.14}$$

When the sound-generating region is acoustically compact, meaning that the distance between any two points in that region is negligible compared to their distance to the observer, the terms $(x_i - y_i)$ and $|\mathbf{x}-\mathbf{y}|$ can be approximated as x_i and $|\mathbf{x}|$ respectively, yielding an alternative, simplified form, of the dipole contribution:

$$\left(\rho'(\mathbf{x},t)c_\infty^2\right)_{dipole} \approx \frac{x_i}{4\pi|\mathbf{x}|^2 c_\infty}\iint_S \left[\frac{\partial p_{ij} n_j}{\partial \tau}\right]_{\tau=\tau^*} dS(\mathbf{y}) \tag{2.15}$$

The above expression shows that dipole noise is attributed solely to changes in the net surface force $p_{ij}n_j$, including both isotropic pressure and viscous stresses.

Quadrupole sound sources appear in areas of intense shear in fluids, such as in the case of a jet, discharging into an otherwise quiescent fluid [25]. The driving mechanism of such sources is usually fluctuating stresses in the shear layer, arising from turbulent mixing of fluid regions with greatly different velocities [10, 25]. Following a similar approach to the one employed for deriving eq. (2.15) presented in [5], a similar relation can be derived for the quadrupole contribution:

$$\left(\rho'(\mathbf{x},t)c_\infty^2\right)_{quadrupole} \approx \frac{x_i x_j}{4\pi|\mathbf{x}|^3 c_\infty}\iiint_V \left[\frac{\partial^2 T_{ij}}{\partial \tau^2}\right]_{\tau=\tau^*} dV(\mathbf{y}) \tag{2.16}$$

where T_{ij} stands for the Lighthill stress tensor defined in eq. (2.11). Lighthill [27] showed that in the case of negligible heat transfer within the flow, the stress tensor is equal to

$$T_{ij} = \rho v_i v_j + \mathcal{O}(M^2) \tag{2.17}$$

hence, the approximation of $T_{ij} = \rho v_i v_j$ is appropriate for low Mach number applications.

Furthermore, Curle [28] showed that the ratio of acoustic intensities[5] of quadrupolar to dipolar noise generated by turbulence near solid bodies, follows roughly

$$\frac{I_{quadrupole}}{I_{dipole}} \propto \left(\frac{U}{c_\infty}\right)^2 = M^2 \tag{2.18}$$

Hence, in low Mach number flows in the presence of solid boundaries, the contribution of the latter can be neglected.

2.2.4 Noise sources in HVAC Ducts

In the present section, the contribution of monopole, dipole and quadrupole noise in HVAC ducts is assessed. The following analysis can be a useful note for rationalizing the process of sound generation by unsteady flows and is presented here only as such[6].

In fig. 2.2, a simplified HVAC duct is illustrated. In order to identify any significant noise sources, Curle's analogy, as formulated in eq. (2.12), is applied. The external surface S consists of S_I corresponding to the inlet cross-section, parts of the duct walls denoted as S_W and a farfield boundary S_F, positioned sufficiently far from the duct outlet, so as to intersect only decayed, essentially quiescent, flow.

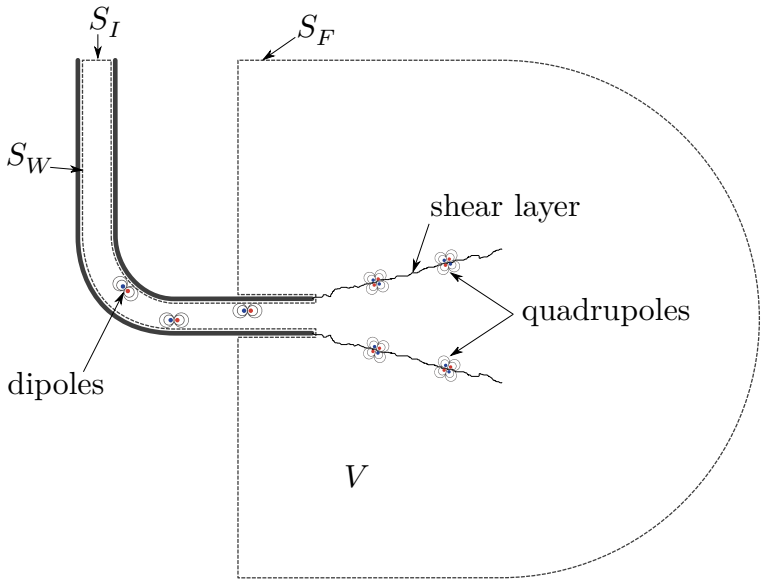

Figure 2.2: Noise source location in a simplified HVAC duct. Curle's analogy is applied by defining the surface S, which is comprised of the inlet surface S_I, parts of the internal and the external wall S_W and the farfield boundary S_F, the last being positioned far enough from the duct exit as to encounter only quiescent flow. The volume V is defined as the interior of S.

[5] Acoustic intensity is defined as acoustic energy per unit area.

[6] It is not required to derive the DNC approach of chapter 3, on which the thesis focuses.

Assuming a constant flow rate through surface S_I, any monopole source vanishes, for the temporal derivative appearing in the respective term of eq. (2.12) is zero. The same can also be extended to surfaces S_F and S_W. Additionally, for the sake of simplicity, the flow at the inlet S_I can be considered laminar, thus without any turbulent fluctuations, rendering the integrand of the dipole term of eq. (2.12) for S_I constant. Hence, the contribution to ρ' is also constant, thus not expressing sound. This of course is not usually the case, since a fan commonly precedes such ducts, causing turbulent inflow. Moreover, since the farfield boundary S_F effectively only encounters quiescent flow, any dipole contribution there is negligible.

All the previous remarks, combined with eq. (2.18), show that, for a typical HVAC duct operating with expected flow rates translating to $\mathrm{M} < 0.1$, only dipole noise is significant, and in particular the one attributed to solid surface loading.

2.3 Hybrid Approaches for Noise Computation - A Brief Note

In low-Mach number applications, such as in the case of HVAC systems, sound and the flow field responsible for its generation are one-way coupled, meaning that the effect the former exerts on the latter is insignificant [11]. This allows for hybrid approaches to sound prediction, in which the flow is simulated using CFD in order to define sound sources, which are then used as inputs for a separate, acoustic simulation [11]. More specifically, unsteady flow simulations can be used as a precursor step, to compute the space-time history of the flow field [11], which then gives rise, through methods based on acoustic analogies, to volume or surface-distributed sound sources. Using those as input, the sound propagation and radiation to the observers are then computed, by solving an appropriate acoustic wave equation, either in the frequency or time domain (examples [14–16]).

As will be discussed in section 3.1, DNC approaches, which are strictly based on unsteady compressible CFD [10], necessitate special treatment and are subject to stringent computational requirements, stemming from the concurrent simulation of both flow and acoustics. The most notable example is the need for high spatial resolution in all areas significant to sound propagation to the observer [30], most of which is non-important when it comes to aerodynamic sound generation. This is overcome by hybrid approaches, in which flow and acoustics are treated separately, with models better fitted for each discipline. Generally, the added cost from the solution of the acoustic problem is, usually, small compared to the unsteady flow simulation [29], therefore any reduction in the CFD cost, has the potential to decrease the total resources needed for CAA noise predictions.

Incompressible CFD simulations are also possible candidates for hybrid methods, at least for low-Mach number flows [11], and have been used in various instances [14, 15, 31, 33]. They offer the potential of further decreasing numerical complexity, as opposed to compressible CFD.

The final remark of section 2.2.4, i.e. that only solid surface loading is significant for noise generated in stationary HVAC ducts, allows, under conditions [15], for hybrid approaches based on Curle's [28] acoustic analogy, utilizing only pressure at solid walls to define sound sources for the acoustic problem [15, 30, 34]. This has the added benefit

that one only needs to store the pressure field at the solid boundaries to proceed from flow to the acoustic solution, further simplifying the process in terms of data storage [34].

An investigation of such methods was performed during this thesis, however without any presentable results to date.

Chapter 3

DNC using the Finite Volume Method

This chapter introduces the Direct Noise Computation approach for aerodynamic noise prediction, based on the finite volume method. First, the complexities of the approach are discussed and three key points are highlighted. This is followed by a brief description of the compressible Navier-Stokes equations i.e. the equations to be solved. Next, the need for high-fidelity turbulence modelling is discussed and the $k-\omega$ SST IDDES[1] model is presented. Finally, the discretization of the governing equations and the spatial and temporal resolution requirements are addressed. The approach was implemented using the OpenFOAM open-source CFD toolbox.

3.1 Introduction to Direct Noise Computation

DNC is a method that aims to predict both the aerodynamic/hydrodynamic and the acoustic field simultaneously, by directly solving the transient compressible Navier-Stokes equations [10, 35]. Under this approach, both the flow mechanisms responsible for sound generation and the propagating perturbations of pressure and density that make-up sound are resolved simultaneously, using CFD, in the same computational domain. The necessity for a compressible CFD formulation is dictated by the nature of sound since it's expressed by perturbations in the pressure and density fields.

Compared to other CFD applications, the DNC tends to be more computationally demanding and also less flexible in terms of numerical treatment [10]. This can generally be attributed to the following points [4]:

- **Scale disparity** As already discussed in section 2.2 and especially in the case of low-Mach number flows, acoustic length scales are usually much larger than hydro/aerodynamic ones, the range of interest of the latter also being wide. This in turn leads to bigger and more refined meshes. In addition, the ratio of mechanical to acoustic power in the flow is $P_{mech}/P_{acou} \approx 10^{-4}M^5$ [10, 27], thus numerical errors deemed acceptable when performing only aerodynamic CFD analyses are now comparable to the acoustic power.

[1] Improved Delayed Detached Eddy Simulation.

- **Distance to observers** Usually the objective of CAA simulations is to predict the sound at a receiver's location, which may be considerably far from the sound-generating region. Therefore, increased spatial and temporal resolution or low-dissipation and dispersion numerical schemes should be employed [10, 35], to prevent the decay of acoustic waves, which, as highlighted in the previous point, are expressed in much smaller power scales, compared to the main flow mechanisms.
- **Boundary treatment** Since the simulation domain needs to be finite, artificial far-field boundaries are used, such as in fig. 2.2, which do not correspond to physical surfaces, as opposed to wall-modelling boundaries. Sound waves should be able to pass through them unimpeded, however, that is not as straightforward as with the case of outflow in purely aerodynamic CFD simulations [4, 10], as sound may spuriously reflect, contaminating the solution. This problem is not limited only to farfield boundaries [10], in fact, it has been shown [36] that locally adapting discretization schemes can also generate spurious noise. (See section 3.5.2)

All of the above remarks generally lead to more computationally intensive numerical simulations, due to increased temporal and spatial discretization requirements, subject to additional difficulties due to the difference in nature of the two disciplines that are being simulated.

3.2 The unsteady Navier-Stokes equations for compressible flows

The underlying physical problem, of noise generation by turbulent flows, is governed by the unsteady compressible Navier-Stokes (N-S) equations, consisting of the continuity (3.1), momentum (3.2) and energy (3.3) conservation equations. They are introduced below, in conservative form, using the Einstein notation, whereby two repeating indices imply summation,

$$\frac{\partial \rho}{\partial t} = -\frac{\partial(\rho \upsilon_j)}{\partial x_j} \tag{3.1}$$

$$\frac{\partial(\rho \upsilon_i)}{\partial t} + \frac{\partial(\rho \upsilon_i \upsilon_k)}{\partial x_k} = \frac{\partial \tau_{ij}}{\partial x_j} - \frac{\partial p}{\partial x_i} + \rho g_i \qquad i = 1, 2, 3 \tag{3.2}$$

In the above expressions, p denotes the static pressure, υ_i the velocity vector, ρ the fluid density, g_i the gravitational acceleration vector and τ_{ij} the stress tensor. The energy equation follows, expressed with the specific total energy E, as the dependent variable [37]

$$\frac{\partial(\rho E)}{\partial t} + \frac{\partial(\rho \upsilon_j E)}{\partial x_j} = -\frac{\partial \dot{q}_{Sj}}{\partial x_j} + \frac{\partial(p \upsilon_j)}{\partial x_j} + \frac{\partial(\tau_{kj} \upsilon_k)}{\partial x_j} + \dot{q}_V + \rho g_l \upsilon_l \tag{3.3}$$

Here, $\dot{q}_{Si}$ represents the heat transfer flux by diffusion, and $\dot{q}_V$ any volumetric heat sources. The total energy is equal to $E = e + K$, with e standing for specific internal energy and K specific kinetic energy, the latter equal to $1/2 \upsilon_i \upsilon_i$.

Equation (3.3) can be further simplified, by neglecting the volumetric heat source term, the gravitational term, and the mechanical energy source term $\partial(\tau_{kj}v_k)/\partial x_j$, their contribution being deemed insignificant for low Mach number applications with negligible heat transfer. Furthermore, according to Fourier's law, and by assuming isotropic medium with a thermal conductivity coefficient k, the heat transfer term can be substituted by:

$$\dot{q}_{Sj} = -k\frac{\partial T}{\partial x_j} \tag{3.4}$$

Finally, the internal specific energy can be substituted by the specific static enthalpy variable, equal to $h = e + p/\rho$. Acknowledging all the assumptions made above, the energy equation can now be re-written in the form of

$$\frac{\partial(\rho h)}{\partial t} + \frac{\partial(\rho K)}{\partial t} + \frac{\partial(\rho v_j h)}{\partial x_j} + \frac{\partial(\rho v_j K)}{\partial x_j} - \frac{\partial p}{\partial t} = -k\frac{\partial^2 T}{\partial x_j^2} \tag{3.5}$$

with static specific enthalpy h, generally being a function of pressure and temperature $h = h(p, T)$ for Newtonian fluids [37]. It is reminded that K stands for the specific kinetic energy $K = 1/2 v_i v_i$.

For the system of eqs. (3.1), (3.2) and (3.5) to be closed, two additional relations between the flow variables are required. Those arise from fluid properties, and for the present work, the air is assumed to abide by the ideal gas law $\rho = p/RT$, as well as to follow $h = C_p T$ relating temperature and enthalpy. The specific heat at constant pressure C_p value is also considered fixed.

3.3 Turbulence Modelling

Since DNC is aiming to directly capture noise generation from the flow field, sufficient resolution of the transient flow structures, including turbulence, causing acoustic perturbations must be achieved. The most common methods for treating unsteady turbulent flow fields are *Direct Numerical Simulation*[2] (DNS) and *Averaging* methods [10].

- *Direct Numerical Simulation*[2] aims at fully resolving the whole turbulent spectrum, from the largest, all the way to the smallest turbulent eddies of length η (see section 2.2). Adequate spatial and temporal resolution to achieve that entails an extremely high computational cost, usually rendering such an approach prohibitive [10].

- *Averaging-filtering approaches* aim to redefine the mathematical model describing the flow, by introducing averaged-filtered flow variables, that do not contain small-scale high-frequency components, thus increasing the smallest scales that need to be resolved [10]. The non-resolved turbulence is then modelled, using statistical models, by modifying the flow equations. The most common averaging-filtering methods for unsteady flows are the Unsteady Reynolds-Averaged Navier-Stokes (URANS) method, the Large Eddy Simulation (LES) method and hybrids between the two.

[2]Should be distinguished from Direct Noise Computation (DNC) which is the subject of the present chapter.

Only averaged methods are used in this work, in which, essentially, part of the flow's total turbulent kinetic energy is resolved as turbulent fluctuations of the flow variables, present in the numerical solution, whereas the rest, which pertains to space and time scales smaller than some specified thresholds, is expressed using a model. This concept is illustrated in fig. 3.1, where the turbulent kinetic energy (TKE) spectrum, ranging from the largest eddies of characteristic length L, to the smallest η (see eq. (2.8)) is simplistically partitioned in resolved and modelled areas.

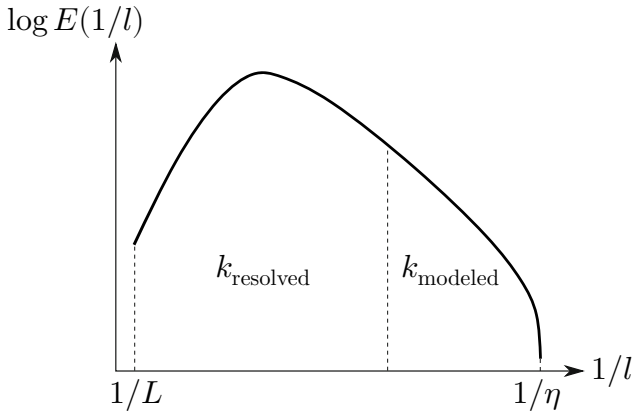

Figure 3.1: Turbulent energy density spectrum in logarithmic scale [38]. The horizontal axis corresponds to the characteristic turbulent length scale, commonly referred to as *wavenumber* [39], while the perpendicular one to energy density, as a function of the former. The area under the spectral function corresponds to turbulent kinetic energy k (symbolic representation).

3.3.1 A brief note on Large Eddy Simulation

Large Eddy Simulation (LES) is a computational approach that aims to separate turbulent flow structures based on their length and time scales, explicitly resolving the greater ones while modelling the effect that the smallest ones exert on the resolved flow, using a statistical *sub-grid scale model* [10, 39]. Subgrid scale turbulence is modelled as fully isotropic and exhibiting only dissipative character [10], therefore the modelled range should contain only smaller scales, to which those assumptions may apply. It is usually agreed [10] that at least $80 - 90\%$ of the total turbulent kinetic energy should be resolved, for accurate LES modelling [10].

The spatial threshold between resolved and modelled turbulence is defined with respect to a cut-off wavenumber κ_c inversely proportional to eddy length scale, related to a characteristic cut-off length $\overline{\Delta}$ by $\kappa_c = \pi/\overline{\Delta}$ [39]. The cut-off limit can either be defined explicitly or be an implicit result of the computational mesh sizing [10], limiting resolved turbulence to scales greater than the local cell size [3].

The main drawback of LES modelling is the great computational cost it entails [40]. That is especially prevalent in the case of wall-bounded flows, such as the ones encountered in HVAC ducts. It has been estimated [41], that in order to accurately resolve turbulent boundary layers using LES, the required number of points in three dimensions scales with

$$N_{xyz} \propto Re^{1.8} \tag{3.6}$$

[3] In the case of a Finite-Volume Formulation

The same requirement, gives a cost value of $Re^{2.2}$ for the inner region, whereas $Re^{0.5}$ for the outer region of the boundary layer respectively [10, 41]. Using LES models in areas where the dominant eddy sizes are comparable to the grid spacing, would result in violation of the assumptions that sub-grid scale models are based upon [41].

3.3.2 DES Family Models

Detached Eddy Simulation models essentially consist of hybrids between RANS and LES models, aiming to incorporate some advantages of both. The original DES97 model was presented by Spalart et. al. [42] in 1997. Their main feature is the use of a modified filter width $\overline{\Delta}$, to allow for RANS-like behaviour in near-wall regions, and LES behaviour elsewhere (fig. 3.2).

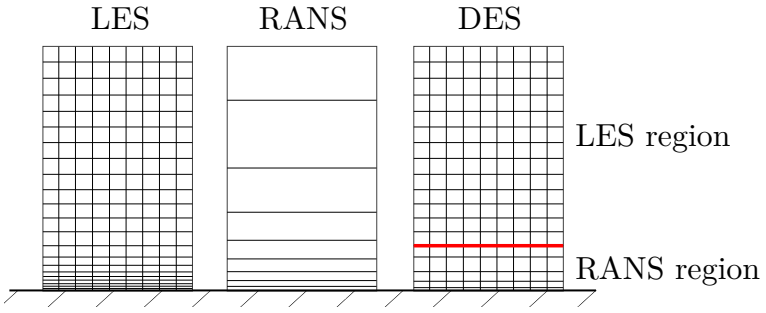

Figure 3.2: Typical example mesh of the LES RANS and DES approaches, in the near wall region. In the case of DES, RANS modelling is active in the near-wall region.

The length scale used in the original model is defined as [10, 42]

$$l_{DES} = \min\left(d_{wall}, C_{DES}\Delta\right) \tag{3.7}$$

where d_w the distance from the nearest wall, C_{DES} a model function, and Δ a quantity associated with the local mesh size. In areas close to the wall, with coarser meshes than intended for LES wall treatment, the d_{wall} scale is active and modelling is switched to RANS. In all other regions, provided a sufficient mesh resolution exists, the sub-grid scale regime is activated.

By treating the near-wall regions with the RANS regime, small-scale and high-frequency turbulent fluctuations, usually associated with the lower parts of turbulent boundary layers [43], are averaged out. That region can then be discretized to accurately capture the velocity gradient, as per usual in RANS Simulations[4]. In the case of aeroacoustic applications, such models can be adjusted in order for turbulent noise-generating flow structures to be treated by the LES regime, whilst RANS is applied elsewhere [40].

It should be noted that a less than sufficient mesh resolution combined with a DES model, might lead to under-prediction of sound, due to RANS dominance, resulting in poor capturing of significant noise-generating structures. To avoid this, mesh resolution metrics can be used to evaluate the suitability for capturing the intended range of sound-generating structures (see section 3.4.2).

[4]Including both High and Low Reynolds turbulence modelling

The k-ω IDDES Turbulence Model

The $k-\omega$ Improved Delayed Detached Eddy Simulation (IDDES) model [44] is a two-equation turbulence model of the DES family, developed from the $k-\omega$ SST [45] Reynolds averaged Stress (RAS) turbulence model. Compared to its precursor DES and DDES models, it has greater capabilities at resolving turbulence in the near wall region [46] and also manages to overcome the miss-match of Reynolds stress prediction in the transition region between RANS and LES regimes [44, 46], observed in those. Similar to RAS approaches, it models the effect of unresolved turbulent scales, by introducing an artificial viscosity term in the momentum equation, deemed eddy viscosity μ_t.

The model introduces two additional PDEs, to be solved on par with the N-S equations, one for the turbulent kinetic energy k, and one for the specific dissipation rate ω [44, 45]. The equations read

$$\frac{\partial \rho k}{\partial t}+\frac{\partial(\rho v_i k)}{\partial x_j}=\frac{\partial}{\partial x_j}\left(\left(\mu+\sigma_k \mu_t\right)\frac{\partial k}{\partial x_j}\right)+P_k-\rho\sqrt{k^3}/l_{IDDES} \tag{3.8}$$

$$\frac{\partial \rho \omega}{\partial t}+\frac{\partial(\rho v_i \omega)}{\partial x_j}=\frac{\partial}{\partial x_j}\left(\left(\mu+\sigma_\omega \mu_t\right)\frac{\partial k}{\partial x_j}\right)+\frac{2\left(1-F_1\right)\rho\sigma_{\omega_2}}{\omega}\left(\frac{\partial k}{\partial x_j}\cdot\frac{\partial \omega}{\partial x_j}\right)+\alpha\frac{\rho}{\mu_t}P_k-\beta\rho\omega^2 \tag{3.9}$$

In the above expressions, P_k denotes the turbulent production term, equal to

$$P_k=\max\left(\tau_{ij}^R\frac{\partial u_i}{\partial x_j}, 10C_\mu\rho k\omega\right) \tag{3.10}$$

where τ_{ij}^R stands for the Reynolds stress tensor, derived from the Boussinesq hypothesis [37]:

$$\tau_{ij}^R=\left(\mu_t\right)\left(\frac{\partial v_i}{\partial x_j}+\frac{\partial v_j}{\partial x_i}\right)-\frac{2}{3}\left(\rho k+\left(\mu_t\right)\frac{\partial v_k}{\partial x_k}\right)\delta_{ij} \tag{3.11}$$

In turn, eddy viscosity μ_t is calculated from

$$\mu_t=\frac{\alpha_1 k}{\max(\alpha_1\omega, F_1 S_t)} \tag{3.12}$$

where S_t stands for the magnitude of the strain rate tensor $S_{ij}=0.5(\partial_{x_i}v_j+\partial_{x_j}v_i)$.

Switching between LES and RANS modes is accomplished through the variation of the characteristic length scale of the model l_{IDDES} which is defined as follows:

$$l_{IDDES}=l_{RANS}\tilde{f}_d+(1-\tilde{f}_d)l_{LES} \tag{3.13}$$

$\tilde{f}_d$ stands for an empirical blending function, exhibiting values between 0, where the model operates in the full LES regime, and 1, where it switches to the RANS mode. The characteristic length of the LES regime is defined as

$$l_{LES}=C_{DES}\Delta \tag{3.14}$$

C_{DES} standing for a model function, and Δ being related to the geometry and mesh through

$$\Delta=\min\left[C_w\max\left(d_w, h_{max}\right), h_{max}\right] \tag{3.15}$$

Here, h_{max} stands for the maximum edge length of the cell, whereas d_w for the distance to the nearest wall. For the RANS regime, the according length l_{RANS} is defined as

$$l_{RANS} = \frac{\sqrt{k}}{C_\mu \omega} \tag{3.16}$$

The remaining model constants and functions appearing in all of the above expressions are omitted here for the sake of simplicity and can be found in [44].

The effect of unresolved turbulence on the flow is accounted for by adding the turbulent viscosity term μ_t to the dynamic viscosity μ. The effective viscosity $\mu_{eff} = \mu + \mu_t$ is then introduced in the stress tensor formulation, abiding by the Boussinesq hypothesis [37]:

$$\tau_{ij} = (\mu_{eff}) \left(\frac{\partial v_i}{\partial x_j} + \frac{\partial v_j}{\partial x_i} \right) - \frac{2}{3} \left(\rho k + \mu_{eff} \frac{\partial v_k}{\partial x_k} \right) \delta_{ij} \tag{3.17}$$

As for the energy equation, the increase in thermal conductivity attributed to turbulence is modelled by injecting the diffusion term of equation (3.5) with an additional turbulent conductivity coefficient. The new effective thermal conductivity, assuming isotropic contribution by unresolved turbulence, is then

$$k_{eff} = k + k_t = k + \frac{\mu_t}{Pr_t} \tag{3.18}$$

where Pr_t is a turbulent Prandtl number, usually given a value of 0.9 [37].

3.4 Resolution requirements

The spatial and temporal resolution requirements for a DNC model stem both from the acoustic and the aerodynamic part of the problem. Specifically, the computational mesh and the global temporal discretization should allow both for correct modelling of the flow structures responsible for generating sound, while at the same time avoiding distortion of the emitted sound waves. This is done based on a target frequency f_{target}, defined a priori, which acts as the main factor dictating spatial and temporal resolution.

3.4.1 Temporal resolution

Temporal resolution should be selected based on the expected frequencies of both turbulence and sound, which coincide, as discussed at the beginning of section 2.2. The theoretical maximum time step can be derived, according to the Nyquist criterion [47], as $\Delta t_{max} = 1/(2 f_{target})$. However, in practice, further refinement is needed to avoid the decay of the propagating sound and insufficient resolution of vortices. The values encountered in literature, usually are 8-12 times the targeted frequency [13, 16, 17, 19, 32]. Moreover, the convective Courant number should be close to unity to ensure the stability of the solution, unless implicit time advancement is selected, yielding more lenient requirements, usually aiming at Courant numbers in the range of 1 to 4 [13], with larger values at less critical regions. The timestep is selected constant, in order to facilitate the post-processing of pressure data at a later stage.

3.4.2 Spatial resolution

Selecting spatial resolution is naturally complicated since a wide range of length scales is involved in such problems, each significant in distinct possibly overlapping regions. Those include the boundary layer, sound-generating geometric fields and their proximity, and the sound transmission path towards the receiver probes.

As discussed in section 3.3.2, the use of DES models, simplifies wall treatment, as the small turbulent structures in those areas need not be captured. However, calculating a correct velocity profile for the near-wall region should be deemed important, to accurately capture separation effects [13], and the interaction of convected turbulence with the boundary layer. For that matter, the first cell layer is positioned at vertical distances of $y^+ \approx 1$ in wall units [13, 19, 32].

Sufficient resolution in the sound-generating regions is achieved implicitly, by using a criterion based on turbulent quantities. It aims to evaluate the ability of the DES family model to resolve a sufficient part of the turbulent kinetic energy (TKE) spectrum. The TKE resolved by the model is equal to [12]:

$$k_{res} = \frac{1}{2}\overline{v_i' v_i'} = \frac{1}{2}\left(\overline{v_i^2} - \bar{v}_i \bar{v}_i\right) \tag{3.19}$$

Given that the rest of it k_{mod} is modelled by the turbulence model, the ratio of resolved to total TKE can be calculated as

$$\Gamma_{RES} = \frac{k_{res}}{k_{res} + k_{mod}} \tag{3.20}$$

As stated in section 3.3.1, a percentage of at least 80% is generally considered acceptable, at least in the regions of interest for sound generation.

To evaluate the suitability of the mesh, an unsteady simulation needs to be performed, from which the Γ_{RES} field can be computed. If the resolution is not sufficient, the mesh can be refined and evaluated anew, using the same process

Finally, the computational mesh should be adequately refined on the sound path, from regions relevant to noise production, all the way to the locations where sound is to be sampled. Therefore, a minimum number of grid points per acoustic wavelength should be selected, based on the maximum targeted frequency. The values for the point-per-wavelength criterion encountered in similar studies, range from $n_{ppw} = 20 - 35$ [19, 40]

3.5 Discretization

3.5.1 Time advancement

Time advancement is performed using a second-order backward temporal discretization scheme [22]:

$$\left.\frac{\mathrm{d}\phi}{\mathrm{d}t}\right|_n = \frac{1}{\Delta t}\left(\frac{3}{2}\phi^n - 2\phi^{n-1} + \frac{1}{2}\phi^{n-2}\right) \tag{3.21}$$

The timestep Δt is explicitly selected and assumed **constant**, to facilitate the post-processing of the computed pressure signals at a later stage.

3.5.2 Spatial discretization

In RANS/LES hybrid simulations, special numerical schemes for the discretization of the momentum convection term have been proposed, in order to best adapt to the presence of the two different turbulence modelling regimes. Such methods usually employ an adaptive blending between central-difference and upwind schemes, the former active in LES regions, while the latter in RANS-treated ones [46]. However, it has been shown [36] that spurious noise may be generated in the transition interface between the two blended schemes, thus such methods should be avoided in DNC. Instead, the momentum convection term is discretized using a constant blend, between a second-order upwind scheme, and a central scheme. The factor is set to a constant value of 85% central difference contribution.

Gradient terms are discretized using the Gauss divergence theorem with linear interpolation, in OpenFOAM [22, 37] for the `rhoPimpleFoam` solver. Any other convection terms present in the model equations are discretized similarly to the momentum convection equation, using a constant blending factor.

3.6 Boundary treatment

As already mentioned at the beginning of this chapter, non-physical phenomena may arise in certain artificial surfaces of the computational domain, such as the inlet/farfield boundaries [9]. By nature, the finite-volume approach for the Navier-Stokes equations requires a finite computational domain [10]. In pure aerodynamic RANS simulations well-established outflow Neumann boundary conditions can sufficiently prevent flow reversal at the domain outlets (farfield), provided that the farfield boundary is sufficiently far from the region of interest in order not to interfere with critical flow regions. However, in turbulence resolving approaches, Neumann boundary conditions may introduce spurious vorticity, and thus sound sources[9]. Most importantly, farfield and inlet boundaries, if not treated properly, act as sound reflectors, possibly contaminating the flow field with non-physical sound components (fig. 3.3). [9, 10]. In summary, within the scope of DNC, when the aim is to simultaneously capture sound-generating flow structures and their resulting sound emission, special methods should be enforced, to counter the effect of artificial boundaries in the computational domain.

3.6.1 Artificial damping regions

A popular technique for treating the aforementioned issues is the ad-hoc introduction of artificial absorption (or damping) regions near the falsely reflecting boundaries [10, 14]. It involves the addition of a source term in the momentum equations, resulting to

$$\frac{\partial v_i}{\partial t} + \mathbf{L}(v_i) = -w\,\gamma\,(v_i - \tilde{v}_i) \tag{3.22}$$

where $\mathbf{L}$ denotes the standard spatial operators appearing in the momentum equation (3.2), γ is a non-negative scalar, w is the intensity scalar ranging in values from 0 to 1 and $\tilde{v}_i$ a time-averaged velocity field. When $\gamma w >> \epsilon$, and assuming a relatively uniform average field $\tilde{v}$ the right-hand term takes precedence, forcing the velocity field v towards its averaged counterpart $\tilde{v}_i$.

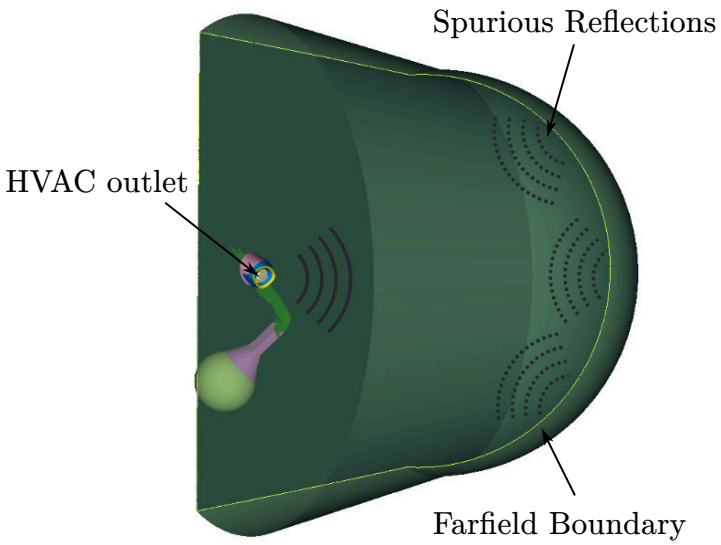

Figure 3.3: Spurious sound reflection at the farfield boundary of the computational domain.

The damping intensity w corresponds to a pre-defined scalar field in the computational domain, gradually increasing from 0 in the near field, meaning no attenuation, to 1 in the far field, where maximum damping is applied, as shown in fig. 3.4.

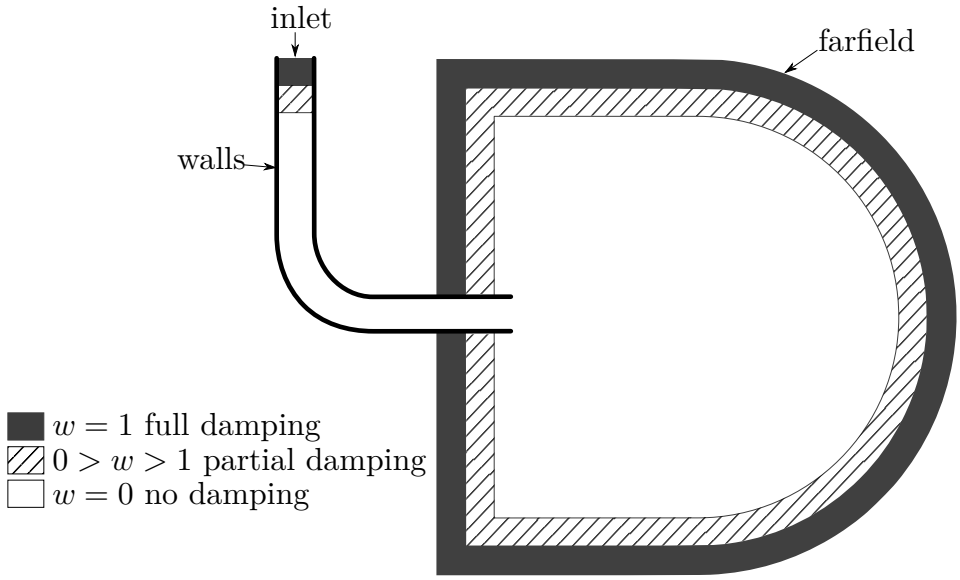

Figure 3.4: Distribution of the damping intensity field, near the farfield and inlet surfaces of the computational domain. Full damping is applied in the regions close to the surfaces ($w = 1$) whereas no damping ($w = 0$) is in the near-field. In the buffer zone between the two, intensity is increased linearly.

The averaged velocity $\tilde{v}$ for each cell is calculated using a rolling averaging window, based on the computed velocity values of the last N timesteps[5]:

$$\tilde{v}_i = \frac{1}{N} \sum_{n=1}^{N} v_i \tag{3.23}$$

[5]The timestep is set constant.

At the beginning of the simulation, where M<N timesteps have elapsed, M is used instead of N.

Choosing the weighting scalar γ and the length of the time averaging window for the calculation of $\tilde{v}$ is not straightforward. Too aggressive damping may act as a numerically imposed wall on the flow, causing sound reflection and flow reversal, especially in the case where the averaging process starts before the flow is fully developed. On the other hand, too lenient damping may fail to attenuate the transient scales approaching the boundary, thus allowing the aforementioned spurious phenomena to take place.

The window length $N \times \Delta t$ has to be greater than the periods of any significant acoustic perturbations, in order to average them out. For the present work, a length of 0.01 s was selected. The rationale for this was that it could dampen all fluctuations of characteristic frequency greater than 100 Hz, standing below the targeted frequencies of the investigated cases (see chapter 6). It was not chosen larger, to not artificially perpetuate the initial quiescent state in the farfield region and result in blocking the flow.

Some calibrating simulations were performed to determine an acceptable value for the intensity γ, however without being fully thorough. By setting it to an initially high value of 1.2×10^5, blocking of the flow was observed. By gradually decreasing it down to a value of 1×10^4, flow reversal and sound wave reflections vanished (see fig. 3.5).

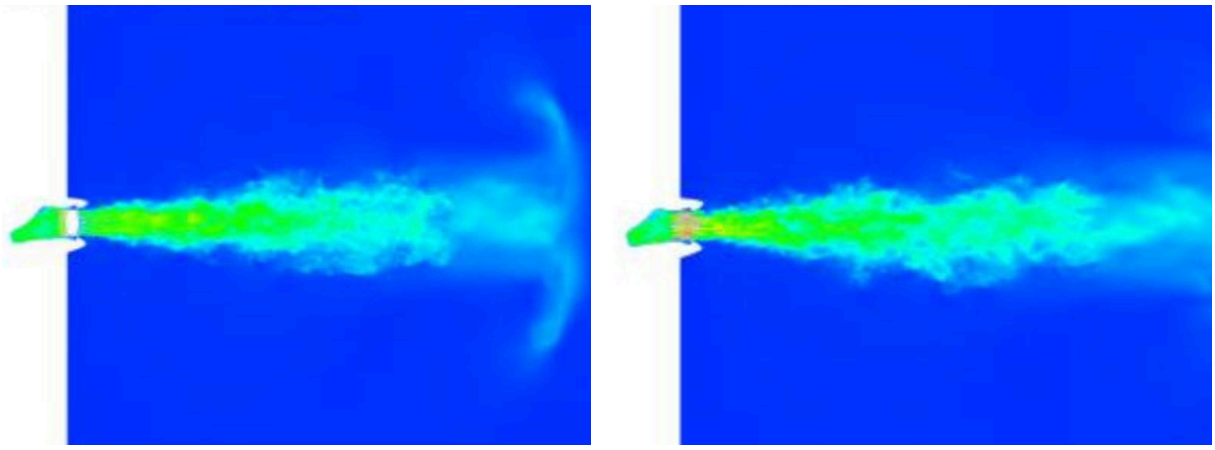

Figure 3.5: Velocity field for damping region intensity $\gamma = 1.2 \times 10^5$ (left) and 1×10^4 (right).

3.7 Summary of the mathematical model

At this point, the governing equations are presented in their final form, subject to all assumptions and simplifications made in the present Chapter.

The flow model is governed by five partial differential equations: continuity (3.24), momentum conservation (3.25), energy conservation (3.26) as well as the two equations of the $k-\omega$ SST IDDES turbulence model variables k (3.27) and ω (3.28) respectively.

$$\frac{\partial \rho}{\partial t} + \frac{\partial (\rho v_j)}{\partial x_j} = 0 \tag{3.24}$$

$$\frac{\partial(\rho v_i)}{\partial t} + \frac{\partial(\rho v_i v_k)}{\partial x_k} - \mu_{eff}\frac{\partial}{\partial x_j}\left(\frac{\partial v_i}{\partial x_j} + \frac{\partial v_j}{\partial x_i}\right) + \frac{2}{3}\left(\frac{\partial(\rho k)}{\partial x_i} + \mu_{eff}\frac{\partial^2 v_k}{\partial x_k \partial x_i}\right) + \frac{\partial p}{\partial x_i} = -w\gamma(v_i - \tilde{v}_i) \quad i = 1,2,3 \tag{3.25}$$

$$\frac{\partial(\rho h)}{\partial t} + \frac{\partial(\rho K)}{\partial t} + \frac{\partial(\rho v_j h)}{\partial x_j} + \frac{\partial(\rho v_j K)}{\partial x_j} - \frac{\partial p}{\partial t} + k_{eff}\frac{\partial^2 T}{\partial x_j^2} = 0 \tag{3.26}$$

$$\frac{\partial \rho k}{\partial t} + \frac{\partial(\rho v_i k)}{\partial x_j} = \frac{\partial}{\partial x_j}\left((\mu + \sigma_k \mu_t)\frac{\partial k}{\partial x_j}\right) + P_k - \rho\sqrt{k^3}/l_{IDDES} \tag{3.27}$$

$$\frac{\partial \rho\omega}{\partial t} + \frac{\partial(\rho v_i \omega)}{\partial x_j} = \frac{\partial}{\partial x_j}\left((\mu + \sigma_\omega \mu_t)\frac{\partial k}{\partial x_j}\right) + \frac{2(1-F_1)\rho\sigma_{\omega_2}}{\omega}\left(\frac{\partial k}{\partial x_j}\cdot\frac{\partial \omega}{\partial x_j}\right) + \alpha\frac{\rho}{\mu_t}P_k - \beta\rho\omega^2 \tag{3.28}$$

The terms appearing in the above equations are described in sections 3.2, 3.3 and 3.6.1.

3.7.1 Boundary conditions

The boundary surfaces appearing in a computational domain for a typical HVAC duct, such as the one illustrated in fig. 2.2, can be divided into three categories: those representing solid walls S_W, inlet surfaces S_I and farfield surfaces S_F. Boundary conditions for the model variables v_i p T k ω, can be globally defined for all surfaces, based on their respective types.

Velocity

At the inlet, a constant volumetric/mass flux, or a constant surface normal velocity is defined. Solid walls are treated using no-slip conditions, whereas a zero Neumann condition is imposed on the farfield boundaries, based on the assumption that the flow field is fully developed when reaching them. This condition should not normally be applied on high-resolution turbulent simulations, as it may incur inaccuracies [9], however owing to the absorption regions discussed in section 3.6.1, the flow is essentially quiescent before exiting the domain.

Pressure

A zero Neumann boundary condition is used for the static pressure field on the inlet and the solid walls, whereas the farfield static pressure is defined based on a constant imposed value for total pressure p_t:

$$p = p_t\left(1 + \frac{\gamma - 1}{2}M^2\right)^{\frac{-\gamma}{\gamma-1}} \tag{3.29}$$

where M stands for the local flow Mach number and γ for the ratio of specific heats, assumed equal to 1.4. The Mach number is calculated as $M = u/\sqrt{\gamma R_{specific} T}$ based on values from the previous solution step of the algorithm.

Temperature

A constant value Dirichlet boundary condition is enforced for the inlet value. A zero Neumann condition is used along the solid walls, effectively modelling all solid surfaces as adiabatic. Farfield surfaces are also treated with a zero Neumann condition, unless reversed[6] flow is observed in some farfield cells, in which the inlet constant value Dirichlet boundary condition is applied.

k and ω

The boundary conditions for the turbulence model variables at the solid walls S_W consist of Dirichlet boundary conditions, the values of which are defined based on High and Low-Re enabled wall functions. Their values are calculated using empirical models and based on boundary layer theory, as well as the height of the first cell in wall units. Their exact formulation is omitted here.

The inlet is treated with Dirichlet boundary conditions with values defined empirically. More precisely, estimates can be attained using eqs. (3.30a) and (3.30b) [37], based on a value for turbulent intensity I, which for flows of low turbulent content is usually estimated at $I < 0.01$ [37] and an estimate for the eddy viscosity ratio μ_t/μ.

$$k = \frac{1}{2} I^2 v_i v_i \tag{3.30a}$$

$$\omega = \rho \frac{k}{\mu} \left(\frac{\mu_t}{\mu} \right)^{-1} \tag{3.30b}$$

The farfield is treated with a zero Neumann boundary condition, unless flow reversal[6] is present, in which case the inlet Dirichlet boundary condition is applied on the affected farfield-adjacent cells.

3.7.2 Model solution

In the scope of the present thesis, the flow equations are solved using the finite-volume cell-centred based OpenFOAM [22] open-source CFD toolbox. More specifically, a steady-state RANS simulation is performed as a precursor step, to initialise the flow field. This is followed by the DNC, for which the complete transient problem is solved using the PIMPLE algorithm [37] for pressure correction, as implemented in the `rhoPimpleFoam` solver of OpenFOAM.

[6] Instead of the flow exiting, it enters the domain.

Chapter 4

Fourier Analysis and Wavenumber Filtering

In this chapter, some theoretical elements of the Fourier transform are presented and the mathematical tools required for processing computed sound signals to extract sound level-frequency spectra are derived. Furthermore, a method for separating acoustic and convective pressure fluctuations is presented which is to be used to process DNC simulation results, for the purpose of comparing them with experimental measurements. Based on those, a utility was developed in the Python™ programming language, which was used to post-process the acoustic results computed through the DNC method of chapter 3.

4.1 Fourier Transform

In many applications, a single metric to quantify sound, such as the SPL (see section 2.1), is not acceptable. As discussed in section 1.2, the sensitivity of the human ear varies greatly depending on frequency. Therefore, an insight into how acoustic energy is distributed throughout the acoustic spectrum could be advantageous, when aiming to quantify sound.

Any continuous time-dependent function $x(t)$, periodic or not, defined in the range $-\infty < t < +\infty$, can give rise to a complex-valued function $X(f)$, in the frequency range, $-\infty < f < +\infty$, called the Fourier transform of $x(t)$. The relationship between the two functions follows [24]:

$$X(f) = \int_{-\infty}^{+\infty} x(t) e^{-2\pi i f t}\, dt \tag{4.1a}$$

$$x(t) = \frac{1}{2\pi} \int_{-\infty}^{+\infty} X(f) e^{2\pi i f t}\, df \tag{4.1b}$$

Using eq. (4.1a), one can calculate the amplitude $|X(f)|$ and the phase angle ϕ for every frequency f, and thus decompose the initial signal $x(t)$ into an infinite number of

harmonic components,

$$x(t) = \int_{-\infty}^{+\infty} x(f,t)\,df = \int_{-\infty}^{+\infty} \left[|X(f)|\sin\left(2\pi t f + \phi_f\right)\right]\,df \tag{4.2}$$

4.1.1 Discrete Fourier Transform

In real-world applications, acoustic pressure time signals $p'(t)$, such as the ones computed by numerical simulation or extracted by digital recordings, are discrete and of finite length. Therefore, using eqs. (4.1) to perform a frequency analysis is not possible.

In that case, the Discrete Fourier Transform (DFT) can be used [48, 49]

$$\hat{p}'_j = \sum_{n=0}^{N-1} p'_n e^{-2\pi j n/N} \tag{4.3}$$

where j is the frequency index, n the discrete signal sample index and N the number of total samples (discrete values) in time. If the values correspond to times of constant[1] interval Δt, the sampling frequency can also be defined as

$$f_s = \frac{1}{\Delta t} \tag{4.4}$$

The frequencies f_j to which the $\hat{p}'_k$ values of eq. (4.3) correspond, are dictated by the number of the discrete signal values at the time domain, specifically:

$$f_j = \frac{j}{N\Delta t}, \qquad j = -N/2, \ldots, +N/2 \tag{4.5}$$

Hence, the theoretically maximum resulting frequency from DFT is equal to half the sampling frequency, i.e. $f_{max} = f_s/2 = 1/(2\Delta t)$. This relationship is known as the *Nyquist criterion* [24, 47]. In practice, for a decent representation of the harmonic decomposition by DFT, a sampling frequency of at least 8 times the maximum desired frequency should be pursued [24]. As one can observe from the above expression, frequencies f_k can attain negative values, however, for a real-valued sequence p', it can be shown that their respective harmonic domain sequence $\hat{p}'$ is zero-symmetric, i.e. $\hat{p}'_j = \hat{p}'_{j-N}$. Therefore, one only needs to compute and store $N/2 + 1$ values[2] to fully describe the spectral distribution of acoustic power.

An issue that arises when using the DFT, is the so-called *spectral aliasing* effect. This effect spuriously increases the values of the Fourier pressure components, usually in a wide range of frequencies, and is caused by the non-periodic nature of the input sequence[3] [49]. A possible solution involves preconditioning the sequence to which DFT is to be applied. [49].

Specifically, the signal is broken into L overlapping segments of length t_{seg} (or N_L samples) each. A window is applied to each segment, essentially zeroing out its beginning and end. The overlapping range is set equal to OL. The above process is illustrated in fig. 4.1. In the present work, the *Hanning* window [49] was used. The discrete window function, for a signal consisting of N_L samples, is defined in eq. (4.6).

[1] As is the case in the DNC approach used

[2] Including the zero frequency value.

[3] Note that the Fourier transform as described in the first part of this chapter applies only to periodic signals.

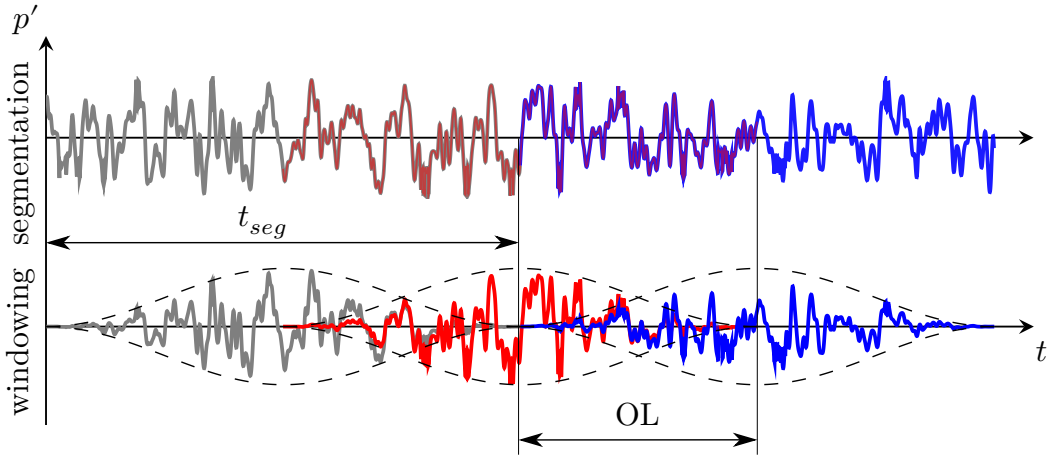

Figure 4.1: Representation of overlapping and windowing technique for avoiding spectral aliasing. From top to bottom: the signal is segmented in overlapping parts of length t_{seg} consisting of N_L samples each, with an overlap length of OL. Next, a window is applied to each segment.

$$w_n = \sin^2\left[\pi\frac{n}{N_L}\right] = \frac{1}{2}\left(1-\cos\left(2\pi\frac{n}{N_L}\right)\right) \qquad n = 0, 1, \ldots, N_L - 1 \tag{4.6}$$

In practice, windowing is performed simultaneously with the Discrete Fourier transform, and not as a separate step. The jth component of the weighted Fourier transform of acoustic pressure can be calculated through

$$(\hat{p}'_j)^2 = \sum_{l=1}^{L} \frac{\left(\sum_{n=0}^{N_L-1} p'_{ln} w_n e^{-2\pi i j n/N_L}\right)^2}{L\sum_{n=0}^{N_L-1} w_n^2} \tag{4.7}$$

It should be noted that any spectrum generated using eq. (4.7) is dependent on the sampling frequency, whereas the dependence on the sample size has been eliminated, owing to the denominator of eq. (4.7).

To allow for comparison of spectra generated using different sampling frequencies, the power spectral density metric is used, defined as

$$\mathrm{PSD}_j = 10\log_{10}\left(\frac{(\hat{p}'_j)^2}{p_{ref}^2 \cdot f_s}\right) \quad [\mathrm{dB/Hz}] \tag{4.8}$$

For reference, a similar quantity, without adjustment for the sampling frequency, is commonly referred to as *Autopower* in literature. Furthermore, since, as already discussed in section 1.2, hearing sensitivity is not equal throughout the acoustic spectrum, the *A-weighting* [50] function is used (fig. 4.2), which adjusts sound level values based on human perception. It essentially consists of a rough approximation of the curves presented in fig. 1.4 and is applied by addition to an acoustic spectrum.

In case the PSD scale needs to be used for comparison with sound spectra not adjusted for frequency resolution, the following formula can be used for conversion to Autopower PSD:

$$\mathrm{PSD}_j^x = \mathrm{PSD}_j^1 + 10\log_{10}(x) = 10\log_{10}\left(\frac{(\hat{p}'_j)^2\, x}{p_{ref}^2 \cdot f_s}\right) \quad [\mathrm{dB}] \tag{4.9}$$

where x stands for the frequency resolution.

To avoid any confusion, unless otherwise specified, all results that follow are given in the PSD scale, as per eqs. (4.7) and (4.8). In the case of A-weighted results, those will be marked with dB(A) units.

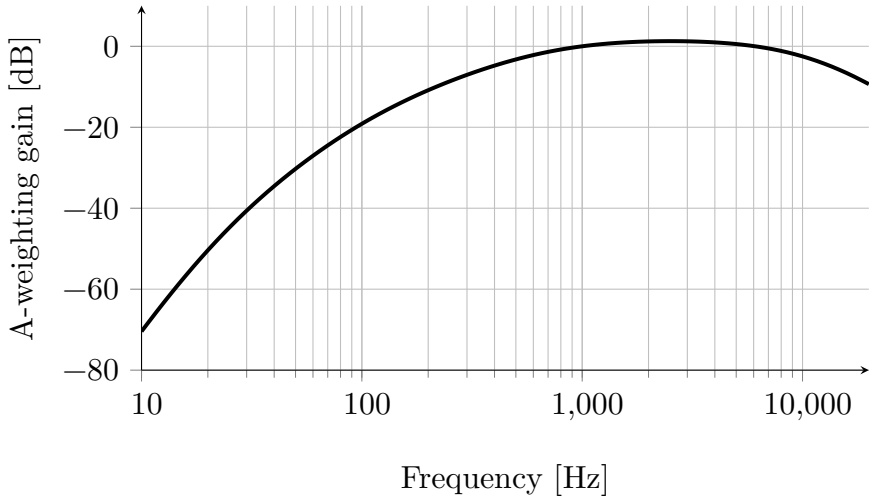

Figure 4.2: A weighting gain as defined by standard IEC 61672-1 [50].

It should be noted that the PSD metric, as defined above, essentially uses the amplitude $|\hat{p_j}'|$ of the harmonic components making up the total signal, instead of the RMS value employed in the definition of SPL eq. (2.6). However, any doubling of amplitude also accounts for approximately a 6 dB increase in the PSD scale, similar to SPL.

For conversion of narrowband spectra, i.e. with a constant frequency spacing, obtained using eqs. (4.7) and (4.8) to Octave spectra of fractional frequency bands, the reader is referred to appendix A.

4.2 Acoustic Pressure Extraction From DNC Using Wavenumber Filtering

The pressure field resulting from compressible DNC simulations, discussed in chapter 3, contains both convective pressure fluctuations, expressing convected flow structures and acoustic pressure fluctuations, expressing sound waves [51, 52]. In other words, pressure fluctuations in the field can be expressed as a superposition of two components

$$p' = p'_c + p'_a \tag{4.10}$$

where p'_c the convective component and p'_a the acoustic component. Note that in previous sections p' was used to describe only the acoustic part.

The p'_c component, usually referred to as *pseudo-sound*, is the result of the pressure gradients related to eddies being convected by the flow [53]. It is deemed *pseudo*, since it lacks some identifying characteristics of sound, such as that it does not respect the wave equation eq. (2.2a) [53]. Nevertheless, it is expressed in the same way, through fluctuations in the pressure field, and can be measured by microphones or even perceived by the human ear[4].

[4] An example is the throbbing sound heard on a windy day by turning the head towards the wind.

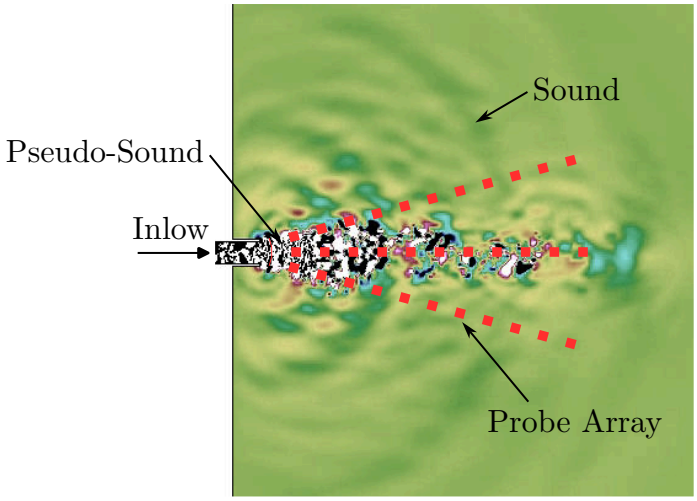

Figure 4.3: Pressure rate of change field. The discharge jet is dominated by pseudo-sound, whereas the outer regions contain mostly acoustic perturbations (sound). Probe arrays are radially positioned parallel to the direction of propagation of disturbances, inside the outflow jet and adjacent to it.

In the case of sound measurements inside a flow field, the placement of microphones will contribute to unsteady convected structures, hence influencing the recorded pseudo-sound. A solution is to introduce foam caps covering the microphones, essentially creating a zone of stationary flow close to it, allowing only sound waves to reach the sensor. For a comparison of numerical results with experimental measurements, it is therefore preferred to focus only on true sound. Thus, in the case of DNC, the acoustic perturbations need to be extracted from the raw computed pressure field.

The main distinction between sound and pseudo-sound comes from the speed of propagation characterizing them, which can be used to identify and separate them. For that matter, the wavenumber can be defined as

$$k = \frac{1}{\lambda} = \frac{f}{u} \tag{4.11}$$

where λ stands for the acoustic wavelength in the case of sound waves, f is the characteristic frequency and u is the speed of propagation of the perturbation. As already discussed in section 2.2 the frequencies of the two disciplines coincide. Acoustic perturbations (sound) propagate with the speed of sound $c \approx 343\ ^{m}/_{s}$, whereas pseudo-sound with the flow velocity, which falls in the range of $U = 0 - 20\ ^{m}/_{s}$ in most HVAC applications, leading to a ratio of wavenumbers $k_a/k_c < 0.1$.

To capture propagation velocity information of a disturbance inside the computational domain, one single pressure probe is not sufficient. For the present study, linear probe arrays were used (see fig. 4.3) parallel to the propagation direction of acoustic and convective perturbations, i.e. the exiting jet.

A two-dimensional Fourier transform on time and space can be performed on the pressure data sampled at the linear arrays of probes. The dimension of time will be transformed to frequency, whereas space to wavenumber, each with inverted units. Similar to eq. (4.7), for each line of probes, the 2D Fourier component can be calculated

through

$$(\breve{p}'_{jk})^2 = \sum_{l=1}^{L} \frac{\left(\sum_{m=0}^{M-1} \sum_{n=0}^{N_L-1} p'_{lnm} w_n w_m e^{-2\pi i \left(\frac{jn}{N_L} + \frac{km}{M} \right)} \right)^2}{L \sum_{n=0}^{N_L-1} \sum_{m=0}^{M-1} (w_n w_m)^2} \tag{4.12}$$

where N_L denotes the number of time instances (temporal samples) of one of the L segments, M the samples in space, i.e. the number of probes of the linear array in question, and $(\breve{p}'_{jk})^2$ the squared Fourier component corresponding to the jth frequency and kth resulting wavenumber. Symbols w_n and w_k denote the real-valued windowing functions in time and space respectively. Note that in the above formula and for the present work, only a single space window was used[5].

The resulting values can be converted to logarithmic units through

$$\mathrm{PSD}_{jk} = 10 \log_{10} \left(\frac{(\breve{p}'_{jk})^2 \Delta x \Delta t}{p_{ref}^2} \right) \tag{4.13}$$

with Δt the constant sampling timestep and Δx the spatial sampling step, which is the distance between two subsequent probes. It should be noted that the spatial resolution Δx, together with the number of spatial samples M used, defines the resolution of the resulting wavenumber space, similar to time and frequency. Therefore, the resulting discrete wavenumbers are given by

$$k_i = \frac{i}{M \Delta x}, \qquad i = -M/2, \ldots, +M/2 \tag{4.14}$$

Logarithmic PSD_{kj} values eq. (4.12) can then be plotted two-dimensionally, on a wavenumber-frequency axis system[6]. Notably, the gradient of a line in such a plot corresponds to perturbation propagation velocity, since $u = f/k$. Two examples are illustrated in fig. 4.4, marked with straight lines of gradients equal to the sound and pseudo-sound propagation velocities, of a typical HVAC blower flow, such as the one depicted in fig. 4.3.

The V-shaped region between two lines of gradients $\pm c + U$ corresponds to pressure fluctuations propagating with the local speed of sound. The pseudo-sound imprint can be located to the right, with a much smaller gradient. It is worth noting that in the right plot of fig. 4.4, generated from probes adjacent to the outflow jet, pseudo-sound is much weaker. The propagation speed expressed in that manner is sensitive to the direction with which their respective perturbations impinge on the linear array. For example, perturbations reaching the array perpendicularly will appear on the $k = 0$ line, since, for what the array probes sense, they are occurring simultaneously in all sensory points in space. Therefore, sound radiation from the jet downstream of the duct outlet will be registered propagating faster than sound.

By zeroing out the values outside the V-shaped area and performing an inverse DFT, the resulting frequency spectra at each probe can be obtained. Those will contain only sound information and can be used in comparison with experimental measurements as needed. The method presented here will be applied in section 6.2.

[5] Thus no summation for windows in space outside the fraction.

[6] Negative frequency components can be omitted because of symmetry around the zero frequency axis, as explained in section 4.2.

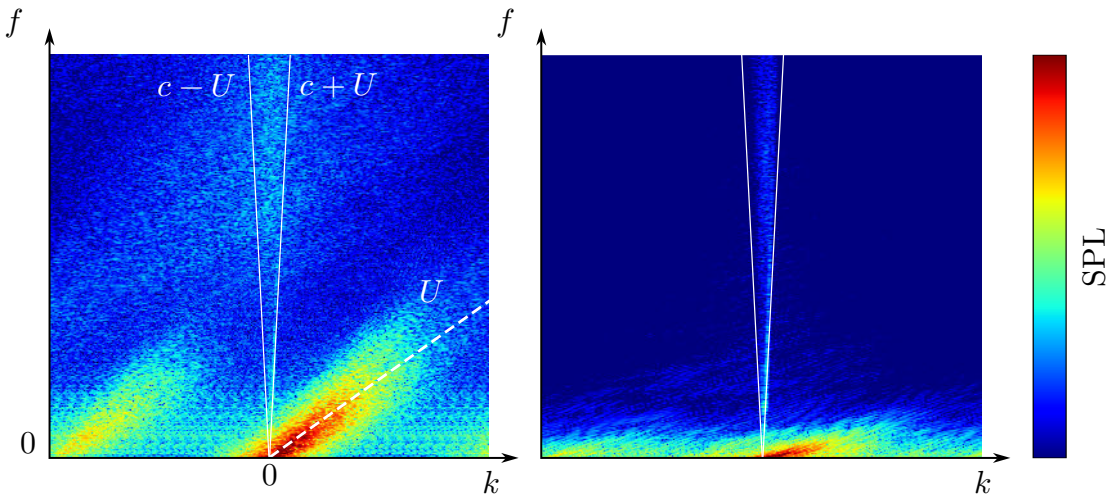

Figure 4.4: Frequency - Wavenumber plots of pressure data sampled at linear probe arrays. The left one corresponds to probe placement inside the outflow jet, whereas the right one to probe placement adjacent to the jet, as in fig. 4.3.

4.3 Development of a Post-Processing Utility

A utility named `SoundPostPy` was programmed in the Python™ programming language, using the in-built FFT capabilities of the SciPy [54] package, to post-process the sampled pressure field computed from the CFD simulation. The developed utility was benchmarked using professional signal-processing software, provided by TME.

It operates in two modes:

A Simple mode: The utility accepts as input pressure-time signals at isolated sampling probes, and converts them to PSD-frequency spectra, through the DFT process (see section 4.1.1)

B Filtering mode: The utility accepts as input pressure-time signals at linear probe arrays, filters out the pseudo-sound component, and converts them to PSD-frequency spectra through the DFT-based process described in section 4.2.

The numerical results presented in section 6.1 were obtained using mode A, whereas those of section 6.2 where linear probe arrays were used to filter out pseudo-sound, using mode B. The experimental results of chapter 5 were obtained using a separate commercial utility, provided by TME.

DNC Approach Summary

At this point, following the presentation of all steps required for the proposed numerical approach in chapters 3 and 4, they are summarised in a flow-chart format:

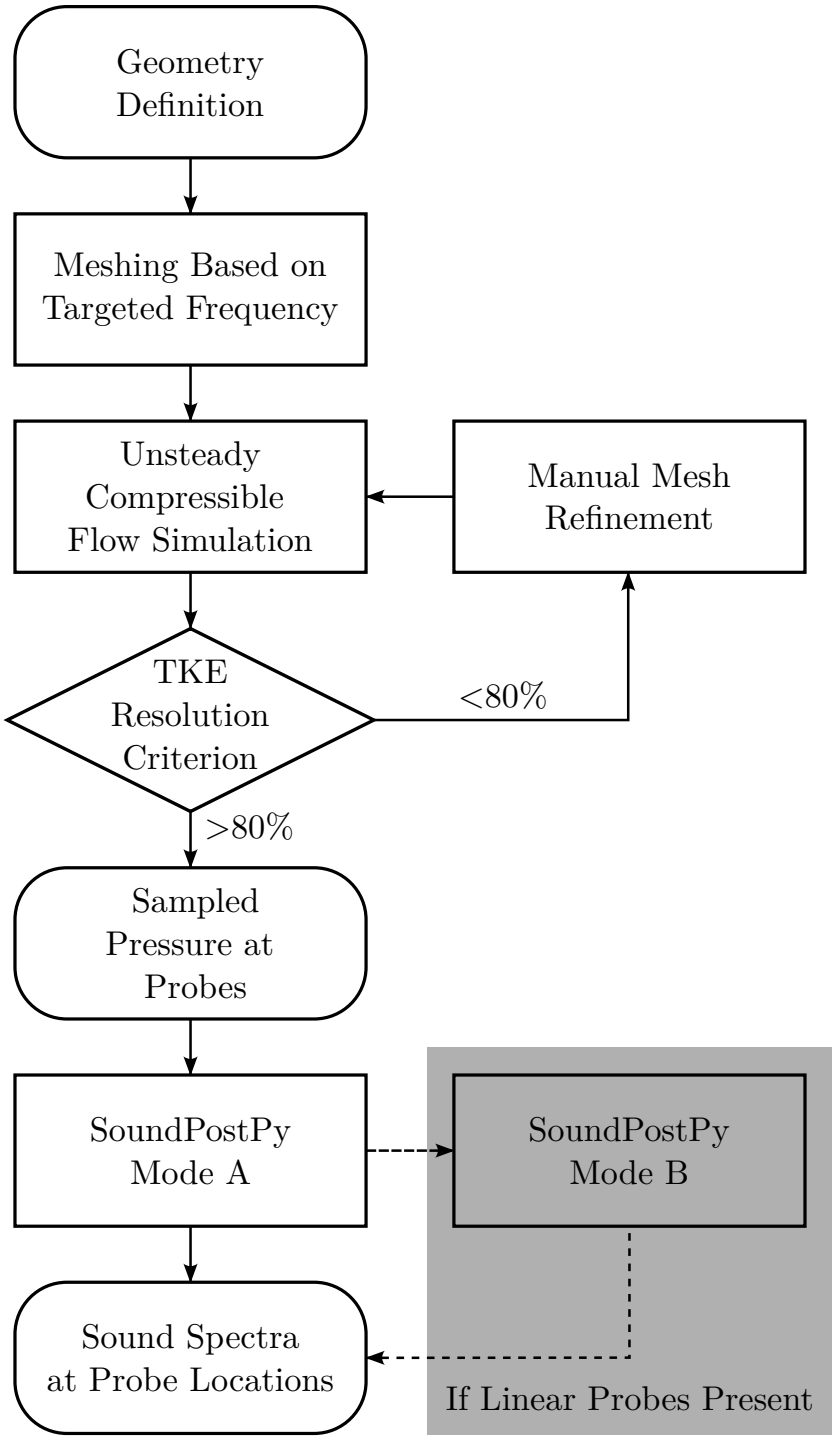

Chapter 5

Experimental Measurements of Aerodynamic Noise in HVAC Blowers

In order to validate the accuracy of the presented CAA method in industrial applications, results should be compared to measurements on real-world production parts. This chapter presents how this is achieved in the present work. Initially, a brief note is provided on measurement techniques usually employed for cabin noise evaluation of production vehicles. Within the scope of the present thesis, a custom measurement setup is devised and implemented, to isolate and measure aerodynamic noise in HVAC ducts. Using this setup, measurements are performed on a passenger car HVAC blower, provided by TME, in various operating conditions, to be compared with their respective numerical predictions in section 6.2.

5.1 Measurements of Vehicle Cabin Noise

In automotive applications, aerodynamic HVAC noise should be evaluated inside the vehicle cabin, in order to account for all the effects supervening on sound transmission. That is to say, absorption and reflection from cabin panelling, seats and even the presence of passengers are expected to contribute to the noise perceived by them. For that matter, passenger head and torso replicas are commonly used (fig. 5.1), positioned on the driver and passenger seats, with microphones on their ear positions. This allows for sound recordings emulating binaural[1] hearing, taking the above factors into account, as well as human noise perception features (directional sensitivity etc.) [55].

Figure 5.1: Binaural head model for noise level measurements in vehicle cabins. (Sourced from [55])

[1] From both ears.

5.2 Proposed Configuration for Isolated Blower

A measurement setup is devised and implemented, with the help of engineers and technicians at TME, to measure the aerodynamic noise generated in HVAC blowers. It involves placing and measuring the testpiece outside the vehicle cabin, in a controlled environment.

5.2.1 Testpiece geometry

The testpiece selected was the driver-side blower located at the instrument panel of a Toyota passenger car (fig. 5.2). It consists of the duct, which channels the air from the central HVAC unit to the register, which features a rotating blade array to direct the flow and adjust the flow rate.

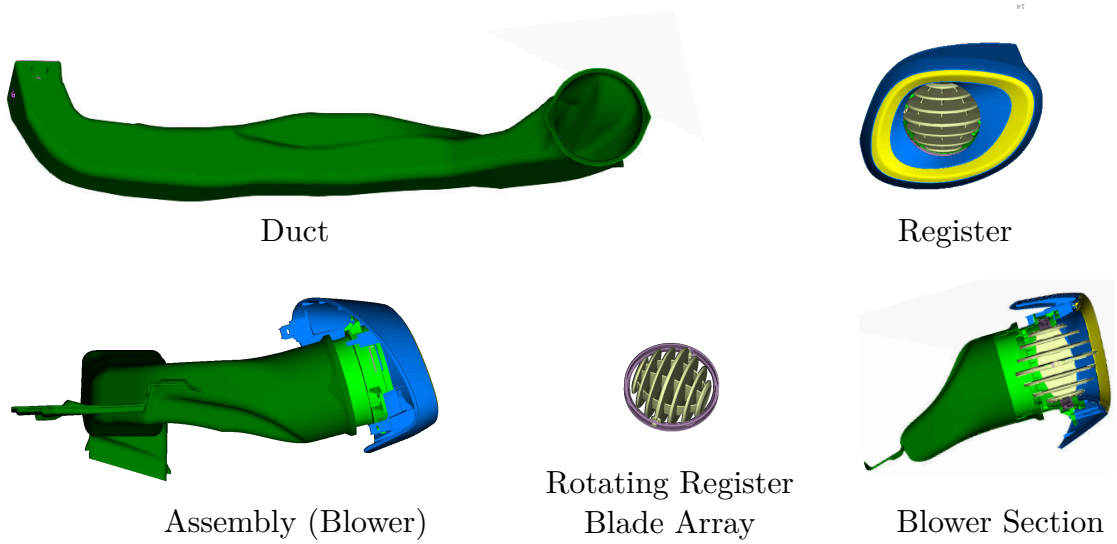

Figure 5.2: Toyota passenger car HVAC blower. The assembly consists of the *duct* (top left) which channels the air from the HVAC unit to the *register* (top right) through which the air is discharged into the cabin. The register features an adjustable blade array (bottom centre), which directs the flow and adjusts the flow rate.

5.2.2 Airflow arrangement and background noise suppression

To isolate and measure only the aerodynamic sound generated by the flow inside the blower, all other background noise sources need to be suppressed. The most significant contribution to *background noise* comes from the equipment required to generate the airflow, in the form of aerodynamic fan noise and mechanical noise due to vibrations (fig. 5.3). The possible transmission paths of background noise towards the receiver locations are the air both inside and outside the ducting, as well as rigid connections between the airflow generator and the testpiece.

In the proposed setup, a simplified representation of which is illustrated in fig. 5.4, the testpiece is placed in an anechoic room, with the airflow generator being located outside. The flow channelling between the two includes flexible piping, in order to avoid noise being transmitted through rigid paths. Furthermore, two sound attenuators are

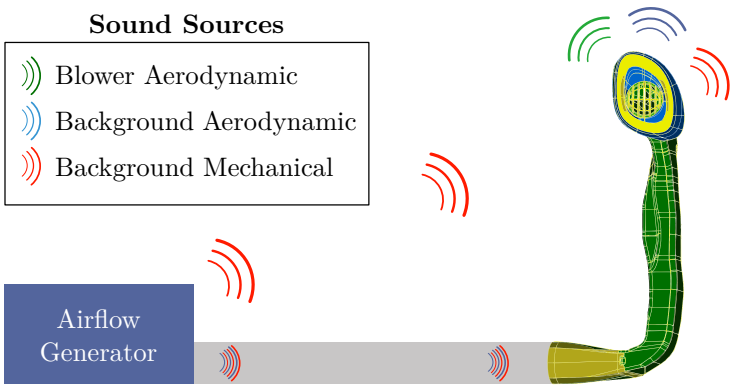

Figure 5.3: Background noise would contaminate the measured sound at the blower outlet. It would be generated by rotating parts in the airflow generator, both as aerodynamic noise caused by the fan, as well as mechanical (harmonic) noise caused by vibrations.

interposed, to dampen the sound travelling within the conducted airflow. To guarantee a fully developed turbulent profile at the blower inlet, a 4 m long, rigid, circular, straight tube is positioned immediately before it, preceded by a cone, to enforce turbulence tripping (fig. 5.6). Finally, the blower is connected to the rigid tube using a customized adapter, created by means of 3D rapid prototyping (fig. 5.5).

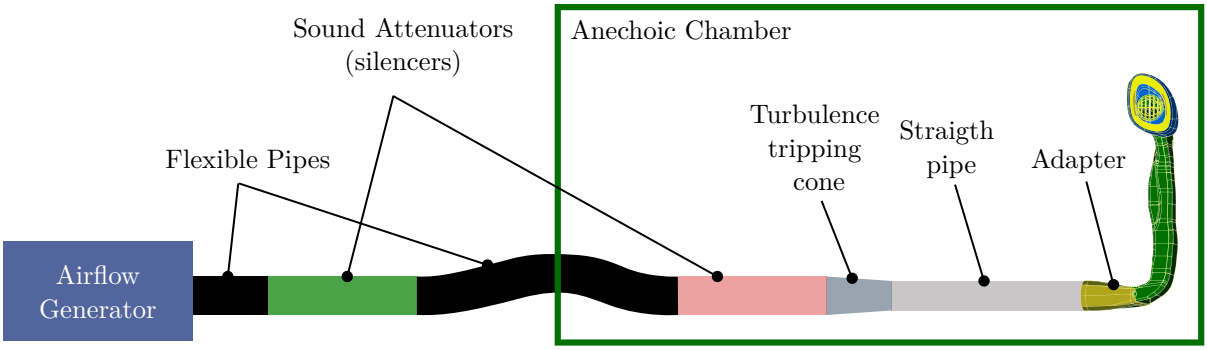

Figure 5.4: Illustration of the proposed layout, for measuring aerodynamic sound generated by the flow inside HVAC Blowers.

5.2.3 Microphone arrangement

A total of 4 1/2 inch omnidirectional[2] condenser microphones [56] were used, to ensure the independence of measurements from the direction they are pointing towards. They were positioned at 4 cardinal locations w.r.t. an axis perpendicular to the centre of the plane defined by a reference face, selected as the outlet section of the duct (fig. 5.7). Moreover, foam covers were utilized, to eliminate *pseudo sound*, meaning recording of pressure fluctuations caused by the non-uniform convected pressure field, a point already discussed in section 4.2. The presented microphone arrangement with the blower positioned as shown in fig. 5.4 and the register blades facing forward, parallel to the x-axis, used for microphone alignment, is hereinafter referred to as **Nominal**.

[2]Responding equally to sound arriving from all directions.

Figure 5.5: Adapter connecting the blower with the straight circular pipe. Left CAD model, right, 3D prototyped part.

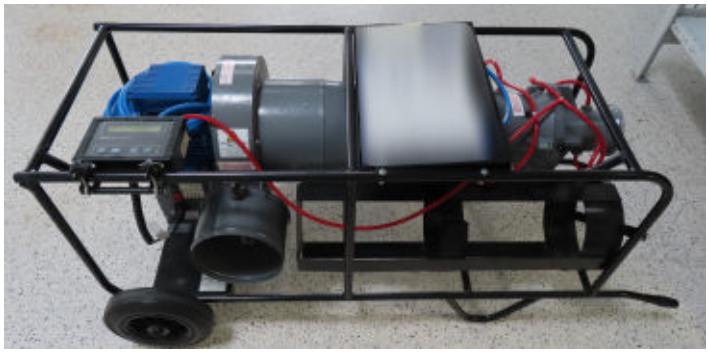

(a) Airflow Generator

(b) Digital Acquisition System

(c) Sound Attenuator (Silencer)

(d) 4 m Straight Circular Pipe

(e) Airflow Inlet to the Anechoic Chamber

Figure 5.6: Components of the proposed measurement setup.

5.2.4 Signal analysis

Recordings were performed using a modular 6-channel analogue-to-digital converter/acquisition system. For each tested configuration, 3 separate measurements were performed for redundancy purposes. Recorded signals from each microphone were processed separately on a DFT basis to extract the sound power spectrum, in Power Spectral Density units (see section 4.1.1). The parameters used for this process, are summarized in table 5.1.

Parameter	Value
Signal length	10 s(×3)
Sampling rate	48000 Hz
Samples per signal	480000
Samples Used	8192
Windowing	Hanning 50% overlap
Frequency resolution	5.859375 Hz

Table 5.1: DFT Processing parameters for each recorded signal.

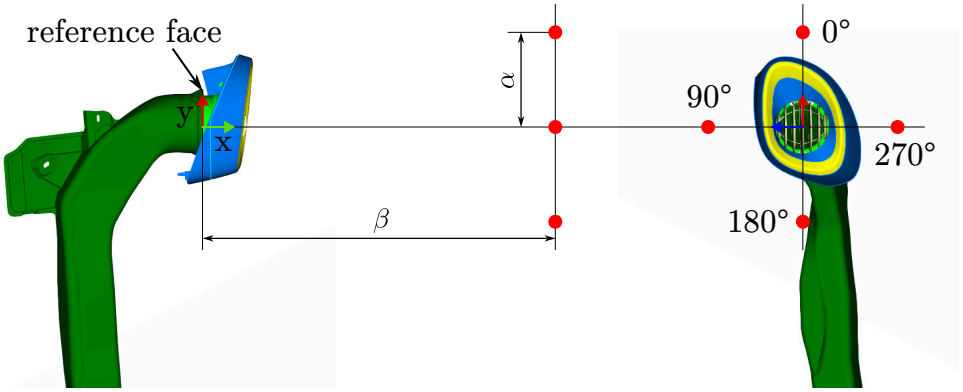

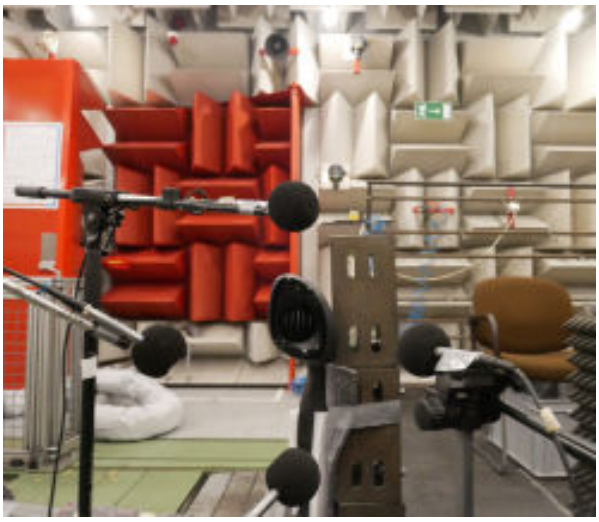

Figure 5.7: Microphone positions for blower noise measurement. Four microphones are used, marked as 0° 90° 180° and 270°.

5.2.5 Background noise evaluation

To evaluate the levels of background noise present in the proposed measurement setup, two additional configurations are used. For the first one, denoted as BG1, the blower (duct and register) are removed and the microphones are retained in their original positions, of fig. 5.7. For the second, deemed BG2, all but the 180° microphone, are placed in the same relative positions to the adapter, as they were to the register in BG1, as shown in fig. 5.8. The purpose of this second setup is to also capture sound travelling through the ducting, not attenuated by the silencers.

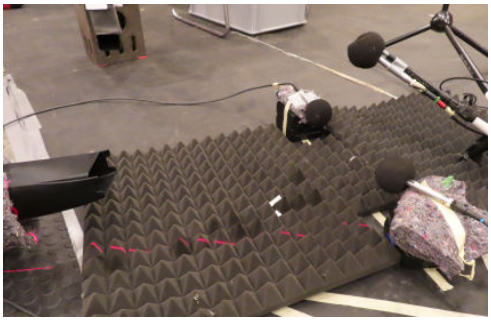

Figure 5.8: Microphone positions for BG2 background noise measurement configuration.

The Nominal configuration, as well as BG1 and BG2 are measured, with the same airflow rate of V_0. The resulting microphone-averaged PSD spectra are sown in fig. 5.9, where a signal-to-background-noise ratio of at least 8 dB, throughout the whole frequency range of interest ($0.4 - 5\,\text{kHz}$), can be observed.

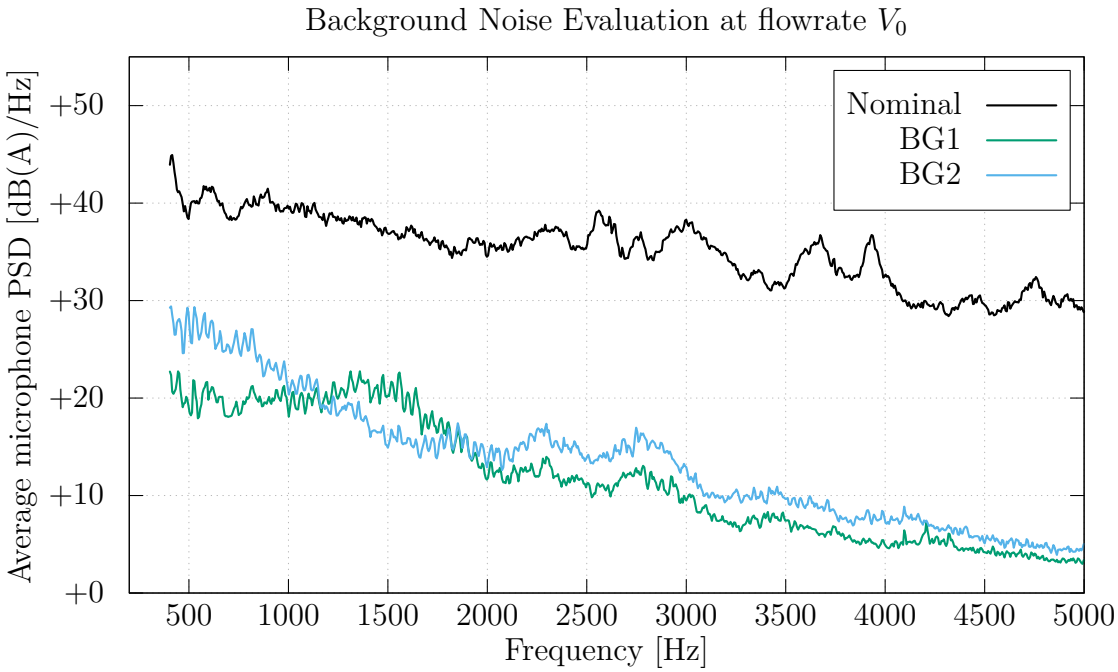

Figure 5.9: Microphone averaged PSD spectra from measurements of the Nominal, BG1 and BG2 configurations for background noise evaluation. Vertical axis values are relative to an undisclosed reference value.

5.3 Measurement Results

The results presented here are attempted to be reproduced in section 6.2, using the DNC CAA method of chapter 3.

5.3.1 Variable Flow Rate

The effect of the volumetric air flow rate that passes through the blower, on the aerodynamic sound it generates is studied. The Nominal configuration is used, with the register blades pointing forward, parallel to the x-axis. The resulting microphone-averaged spectra are displayed in fig. 5.10. As one can observe, the increase in flow rate results in a mostly uniform increase in the sound power, throughout the whole frequency range of interest.

5.3.2 Rotation of register blades

To evaluate the effect of the register blades' position on the resulting sound levels, two additional measurement configurations are employed. The register's blade array is rotated around the y-axis by an angle ϕ, together with the microphone centerline, essentially retaining the same microphone positions w.r.t. the blades (see fig. 5.11). The configurations are referred to as T30 and T45, for $\phi = 30°$ and $45°$ respectively.

The configurations are measured at V_0 and compared with the Nominal measurements for the same airflow. The resulting 1/3 Octave and narrowband microphone-averaged spectra are displayed in figs. 5.12 and 5.13. As expected, greater rotation results in higher sound levels, since constriction of the airflow leads to higher velocities.

Furthermore, two peaks appear at around 1500 and 2750 Hz, which were not visible in the Nominal configuration.

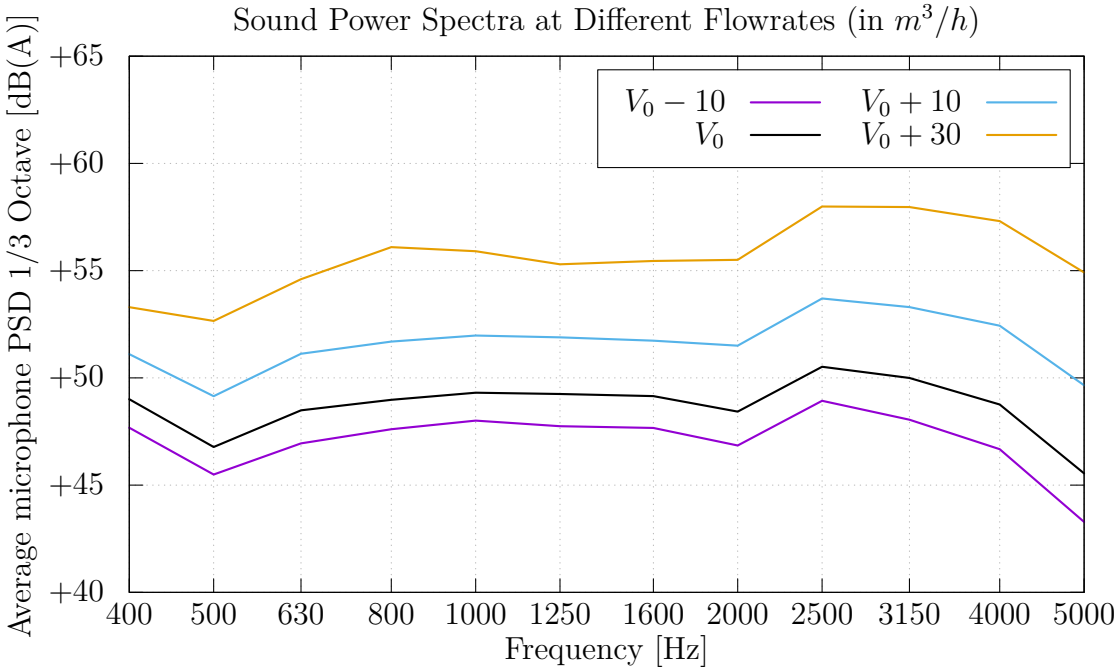

Figure 5.10: 1/3 Octave microphone-averaged spectra for different flow rates. (Relative vertical axis values)

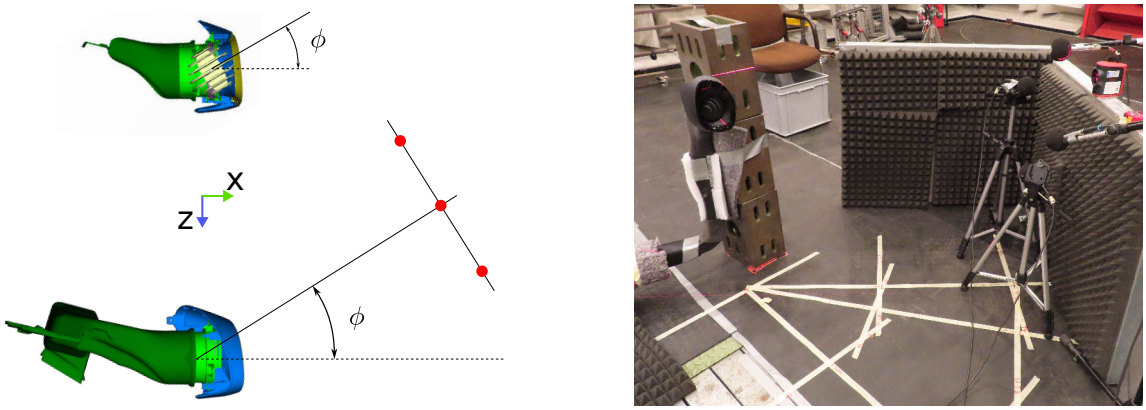

Figure 5.11: The Tϕ measurement configuration for evaluation of the register blades' position effect on the sound levels generated.

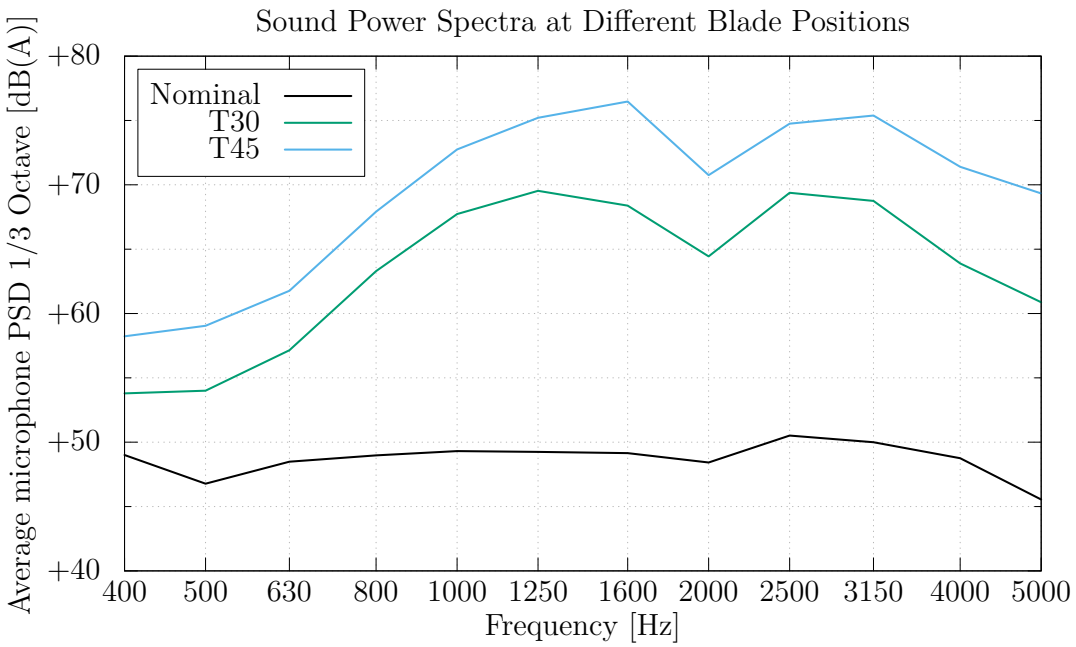

Figure 5.12: 1/3 Octave microphone-averaged spectra for different blade positions. (Relative vertical axis values)

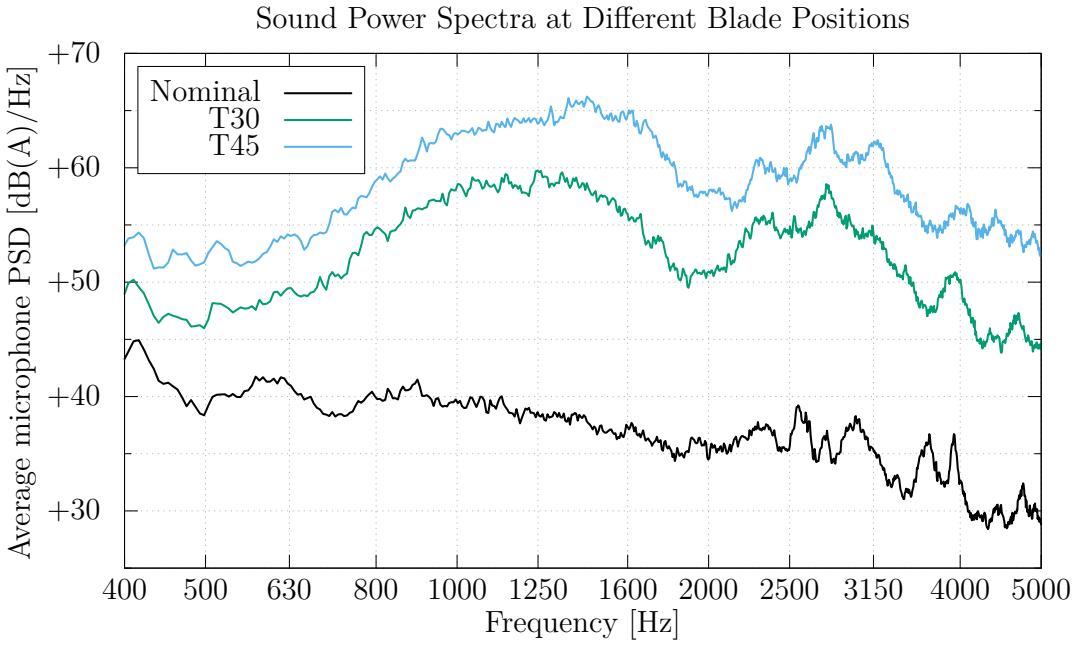

Figure 5.13: Narrowband microphone-averaged spectra for different blade positions. (Relative vertical axis values)

Chapter 6

Validation of DNC Method using Experimental Results

In this chapter, the DNC method presented in chapter 3 is applied to one test case and an industrial case. The test case is the simplified HVAC duct, first studied by Jaeger et. al. [13]. The second consists of the driver-side instrument panel duct and register of a Toyota production car, for which measurements were presented in chapter 5. Numerical results are compared with experimental measurements, to determine aerodynamic noise levels at specific locations downstream of the air outlets. Especially for the simplified HVAC case, the proposed method is contrasted with other approaches, the results of which have been sourced from literature.

6.1 Simplified HVAC Duct

The simplified HVAC duct benchmark case [13] has been used in the past to validate CAA approaches for aerodynamically induced noise prediction in HVAC systems [14–18, to name but a few instances]. The authors have performed and published PIV and sound measurements of this case. Acoustic spectra of those measurements have been digitised from the cited [13, 14] publications and are used to evaluate the performance of the proposed numerical approach.

6.1.1 Geometry Description

The geometry setup, illustrated in fig. 6.1, consists of a square duct with a 90° bend, on the outlet of which a rigid flap is placed at a 30° angle.

In order to define a closed computational domain, additional components are added, as shown in fig. 6.2. The inlet section is extended to a length of $0.5m$, in order to ensure a fully developed flow profile. A bulbous inlet plenum is positioned at the end of the extruded section, to increase the volume on which artificial absorption (See section 3.6.1) is enforced, to avoid reflection of sound waves travelling towards the inlet. Furthermore, a plenum is introduced downstream of the duct exit, for the flow to discharge and also to contain the pressure probes, used to capture the generated sound.

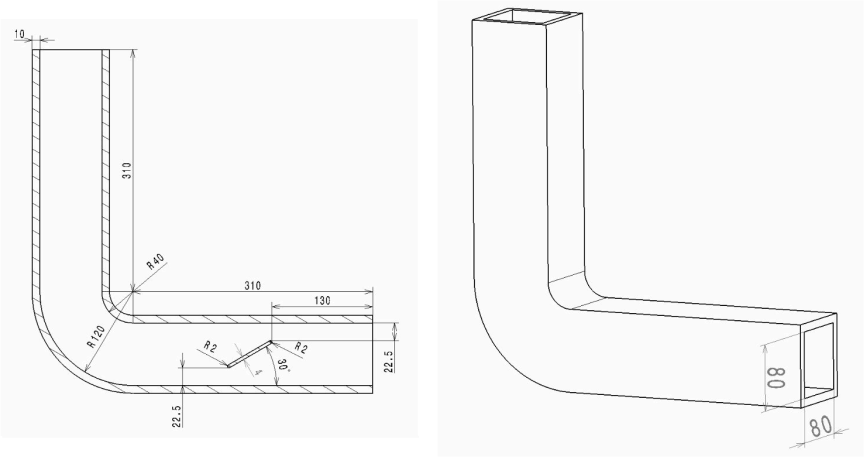

Figure 6.1: The simplified HVAC geometry consists of a square duct with a 90° bend. It also features a rigidly placed flap, placed at an angle of 35 degrees relative to the flow direction. (Graphic sourced from [13], lengths in mm)

6.1.2 Boundary Values and Fluid Properties

The fluid properties of air and boundary values used for the simplified HVAC case are summarized in table 6.1. Except for the inlet velocity, which is explicitly defined in the original publication [13], all values are calculated approximately, based on ambient conditions. The exact boundary conditions can then be derived, according to their definitions in section 3.7.1.

Region	Variable	Symbol	Value
Globally	Dynamic Viscosity	μ	$1.813 \times 10^{-5}\,\mathrm{Kg/(m\,s)}$
	Constant Pressure Heat Capacity	C_p	$1007\,\mathrm{J/(Kg\,K)}$
	Specific Gas Constant	$R_{specific}$	$287.05\,\mathrm{J/(Kg\,K)}$
Inlet	Velocity Magnitude	U	$7.5\,\mathrm{m/s}$
	Turbulent Intensity	I	0.01
	Eddy Viscosity Ratio	μ_t/μ	70
	Static Temperature	T	$288\,\mathrm{K}$
Farfield	Total Pressure	p_t	$10^5\,\mathrm{Pa}$

Table 6.1: Boundary values and fluid properties for air, used in the simplified HVAC Case [13].

6.1.3 Measurement probe locations

The sound generated by the flow was captured at 289 locations, which correspond to the microphone positions used in real-world experimental measurements, performed in [13], on the same geometry [13, 14, 18]. The probes are positioned at a distance of $1m$ from the square duct outlet, forming a hemisphere, as shown in fig. 6.3.

Moreover, pressure fluctuations were captured in 3 positions shown in fig. 6.4, close to the walls on the mid-plane of the geometry, which correspond to the positions of

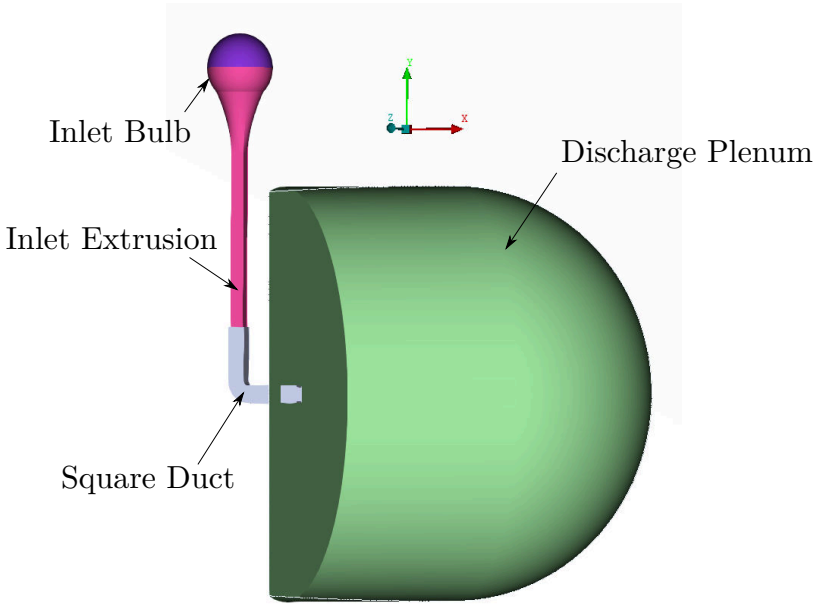

Figure 6.2: Positioning of the components defining the computational domain: the discharge plenum (green), the front part of which has been removed for visual purposes, the inlet extrusion (pink) the inlet bulbous structure (purple) and the actual duct (grey).

wall-flush mounted microphones in the experimental measurements [13]. The maximum frequency for which results are available[1] is 2 kHz [13, 14].

6.1.4 Computational Mesh

The computational mesh (see fig. 6.5) was generated following a surface-to-volume approach, using a commercial mesher, provided by TME. It is composed of regions of locally uniform hexahedral cells. The meshing procedure begins with the generation of a uniform mesh made up of cubes of edge length h_0, which are then refined in specified regions, up to a defined refinement level. Each refinement level n is attained by performing n consecutive subdivisions of the initial cubic cells of edge height h_0 into 4 equal cubic cells. Therefore, the edge length of a cubic cell of refinement level k is equal to $h_k = h_0/2^k$. Inflation layers are introduced in the near wall regions of the duct and the flap, to achieve values of $y^+ \approx 1$ in the first layer. The required cell spacing to accurately resolve sound transmission from the exit of the square duct and the probe dome of fig. 6.3, up to a maximum frequency of $f_{target} = 2\,\text{kHz}$[2], can be calculated using the following expression:

$$\Delta x = \frac{c}{f_{target} n_{PPW}} \tag{6.1}$$

where c stands for the speed of sound, and n_{PPW} is the required number of points to resolve an acoustic wavelength.

The acoustic transmission region is filled with cells of height $h = 5.2\,\text{mm}$, which results in approximately 32 points per minimum acoustic wavelength. The Mesh is

[1] The original publication [13] only presents results up to 1 kHz for the wall-mounted microphones, however farfield measurements up to 2 kHz were provided by the original authors to Kierkegaard et. al. [14], who, in turn, published them, and are sourced from there.

[2] Corresponds to the maximum frequency for which experimental results are available [13, 14].

gradually coarsened towards the domain farfield region, up to a height of 20.8 mm, and refined at the flap region, up to a minimum of 0.65 mm, as shown in fig. 6.5b. The cell height ratio between two neighbouring refinement levels is equal to 2.

Finally, the absorption intensity field w (see section 3.6.1) is defined as shown in fig. 6.6, introducing damping regions both on the inlet and the farfield boundary of the computational domain.

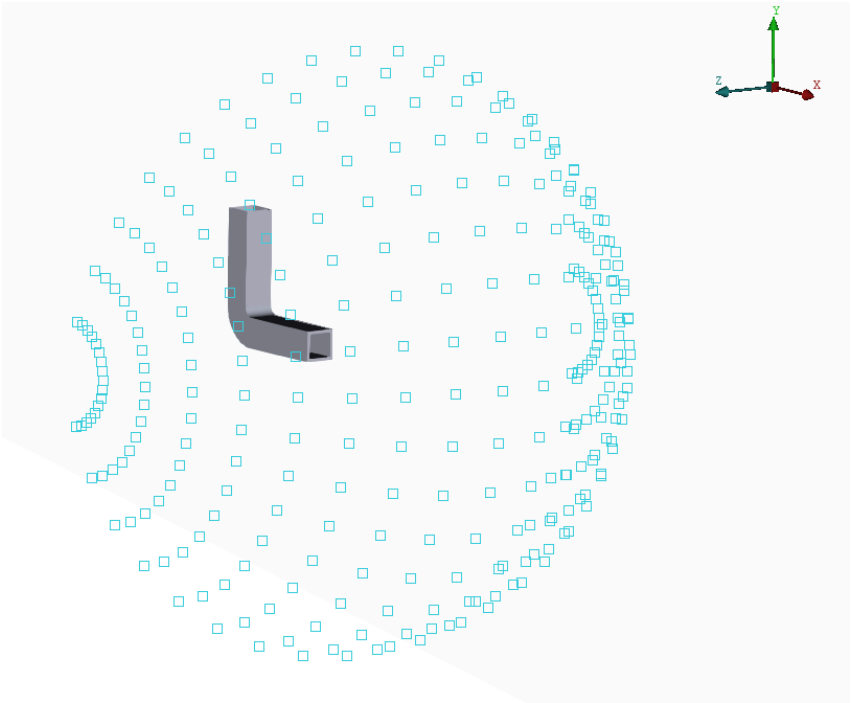

Figure 6.3: Pressure probe locations, corresponding to microphone positions in the experiments performed in [13], forming a hemisphere with a $1m$ radius from the square duct exit.

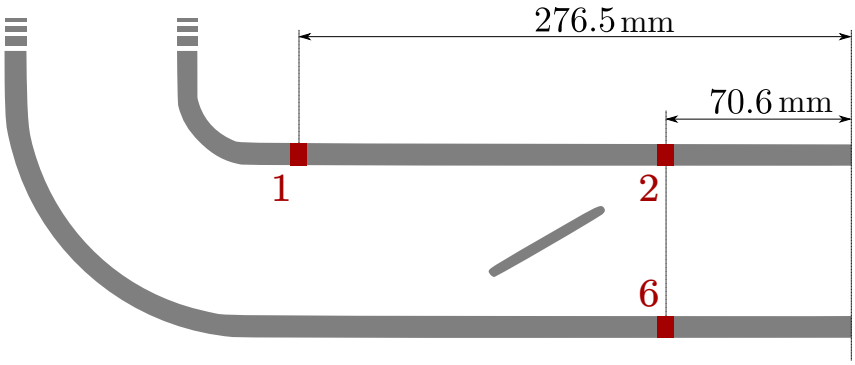

Figure 6.4: Positions of the 3 pressure probes to capture near-wall pressure fluctuations, corresponding to the respective microphone locations. The probes are located on the duct's plane of symmetry (mid-plane). The numbering of the original publication is retained.

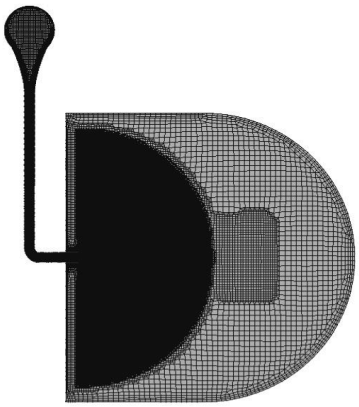

(a) Complete mesh section. Refinement of $h = 5.2\,\text{mm}$ up to the probe locations.

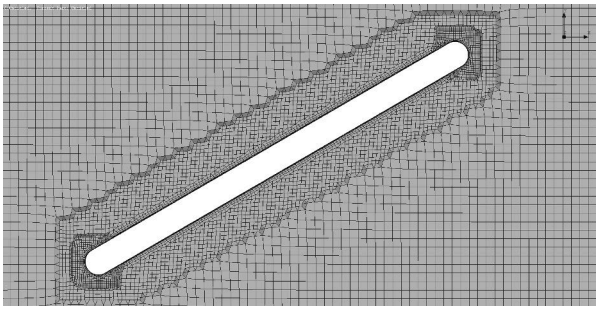

(b) Refinement near the flap surfaces. Highest refinement at flap edges, of $h = 0.65\,\text{mm}$.

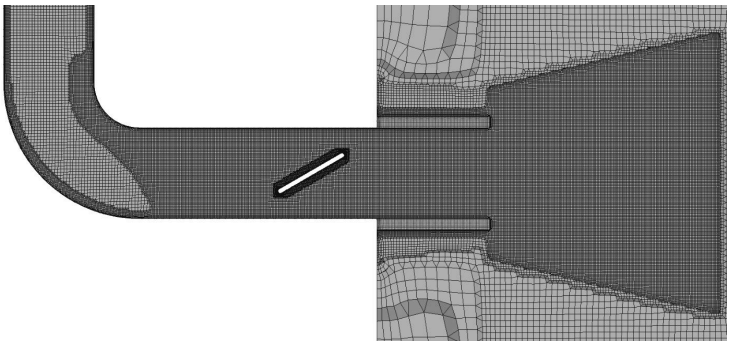

(c) Duct and Flap region

Figure 6.5: Section of the computational Mesh for the simplified HVAC case, at the mid-plane of the duct.

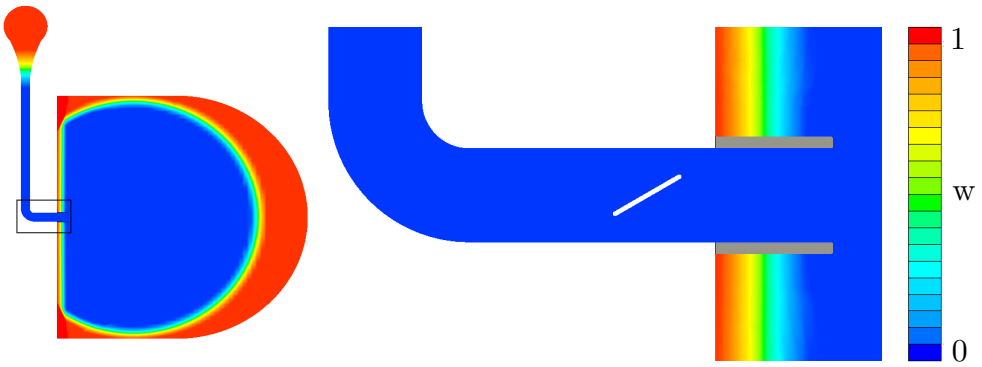

Figure 6.6: Damping intensity field w of the absorption regions. Values of 0 correspond to no damping, whereas values of 1 to maximum damping.

6.1.5 Mesh Refinement based on TKE resolution

In order to ensure at least 90% resolution of the turbulent kinetic energy spectrum, the resolved TKE percentage metric presented in section 3.4.2 is evaluated, according to eq. (3.19). For that matter, a first simulation was performed, for a transient duration of $T = 0.4\,\mathrm{s}$ and the instantaneous percentage of resolved TKE Γ_{RES} field of eq. (3.19) is calculated and stored. An Iso-surface corresponding to 92% TKE resolution is then extracted and used to further refine the volume it encloses[3]. The resulting mesh refinement region (fig. 6.7) leads to an increase in the ratio of resolved to total TKE, as shown in fig. 6.8. The resulting mesh consists of approximately 29.4 million cells, 0.4 million more than before the refinement process.

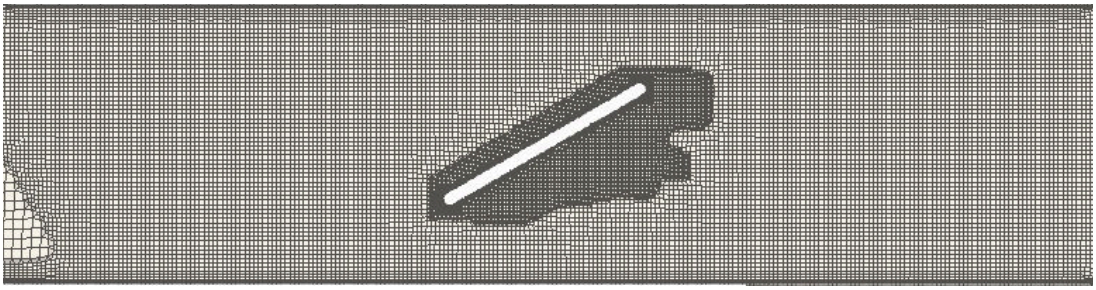

Figure 6.7: Mesh refinement region near the flap. The refinement region is defined using the iso-surface corresponding to 92% resolution of TKE in the initial mesh. The cells enclosed or cut by the iso-surface are refined down to a cell height of 1.3 mm.

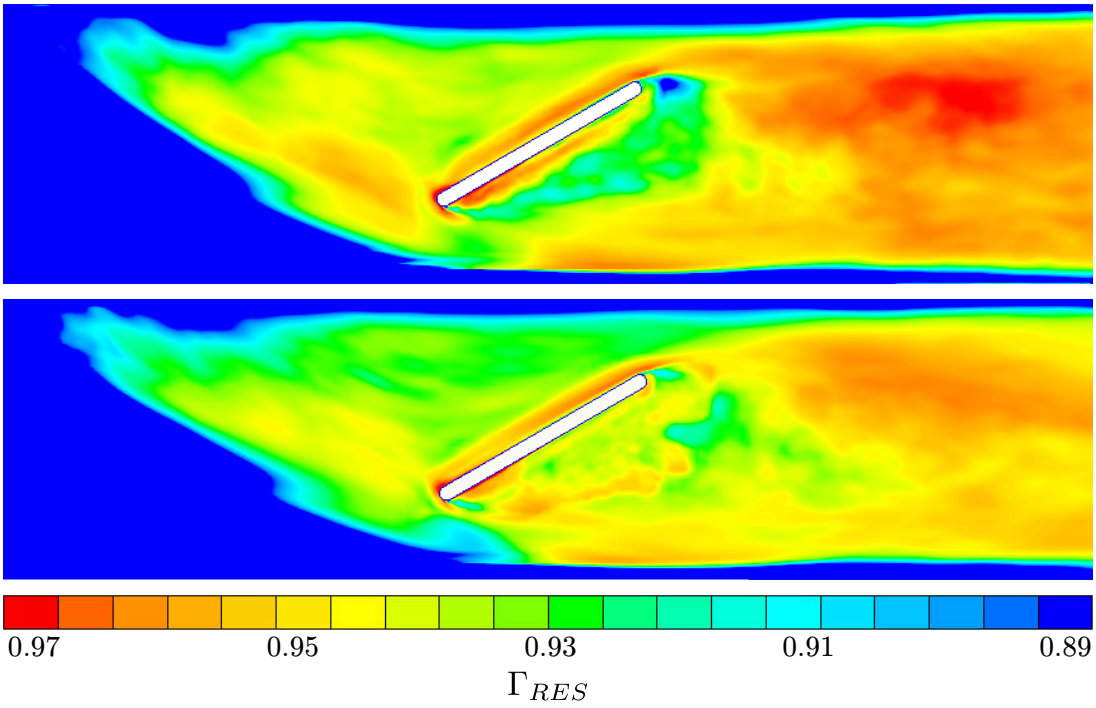

Figure 6.8: Ratio of Resolved to total TKE before (top) and after (bottom) refinement.

[3]The cells enclosed or cut by the iso-surface are refined up to 1.3 mm, which corresponds to the level used on the flap surface.

6.1.6 Results

The flow inside the simplified HVAC duct was simulated for 0.4 s. The simulation step was chosen equal to 2.5×10^{-5} s, resulting in a sampling frequency 20 times the targeted one. A warm-up period of approximately 0.15 s can be observed in the convergence history, presented in fig. 6.9, during which the flow is transitioning from the steady state regime of the precursor RANS simulation to the fully-transient regime.

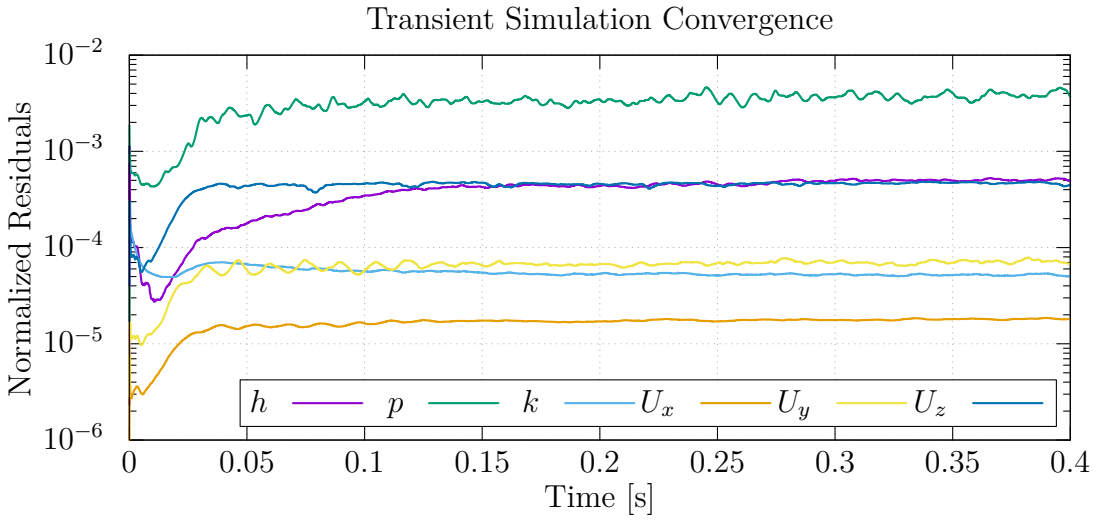

Figure 6.9: Convergence history of the transient flow simulation for the simplified HVAC case. a warm-up period can be observed during the first 0.15 s, during which the transition from the precursor steady-state RANS simulation, is occurring.

A mid-plane section of the x-wise component of the velocity field is illustrated in fig. 6.10. The separation immediately downstream of the elbow bend is greatly under-predicted compared to the PIV measurements published in [13], while a good correlation is observed on the flap wake.

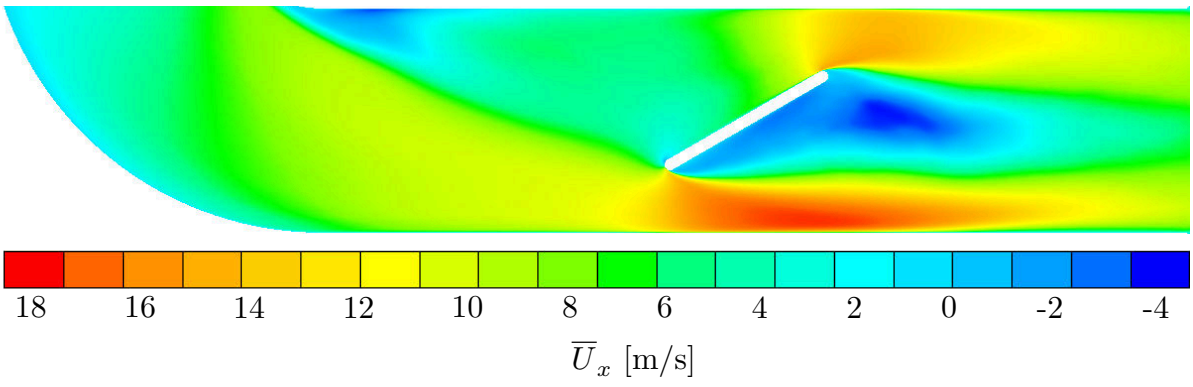

Figure 6.10: The averaged x-velocity (outflow-wise) component at the mid-plane surface. Flow separation is greatly under-predicted, based on the PIV results performed by Jaeger et. al. [13]. However, the region of the flap wake seems accurately predicted.

The pressure field on the mid-plane (meaning the symmetry plane) of the duct was also stored, and processed using FFT for 1/3 octave bands, to identify pressure fluctuation modes of the flow. The resulting fields for 4 different frequency bands are

illustrated in fig. 6.11. The main noise-generating features of the geometry are identified as the edges of the tilted flap.

Wall pressure fluctuations

The pressure field was sampled at the first cell of the inflation layer closest to the probe locations of fig. 6.4. Sampling was initiated at $t = 0.15\,\text{s}$, which corresponds to the end of the warm-up period (see fig. 6.9). The FFT analysis was performed on the last 8192 samples, i.e. the last 0.2048 s of the simulation, well after the warm-up period, using 3 Hanning windows, with a 50% overlap (see section 4.1).

The power spectra were calculated in PSD format using equation eq. (4.8), and then adjusted for the sampling frequency used for the published experimental measurements ($f_s = 4\,\text{Hz}$), using eq. (4.9). They are presented in fig. 6.12 along with the experimental values and results obtained using both a Finite-Volume k-ε DES and a Lattice-Boltzman VLES (Very Large Eddy Simulation) DNC approach [13], as well as a hybrid method based on incompressible CFD [15].

The numerical results at probe 6 (fig. 6.12b), which is located downstream of the flap exhibit a good correlation with the experimental measurements, except for the peak at 8 Hz, which is probably caused by a low-frequency mode of the flow not captured due to the short overall physical time used for the Fourier transform (4096 samples, $T \approx 0.1\,\text{s}$). In the case of probe 1 (fig. 6.12a), the pressure fluctuations seem to be overpredicted throughout the spectrum, by a magnitude of $5 - 15\,\text{dB}$, which can in turn be explained by the underprediction of the flow separation downstream of the elbow (see fig. 6.10), leading to faster-moving air close to the wall at this location. This effect is also thought to be responsible for the under-prediction at probe 6 (fig. 6.12c), since the delayed separation leads to a bigger part of the flow being directed above the flap, contributing to less turbulence in the lower regions.

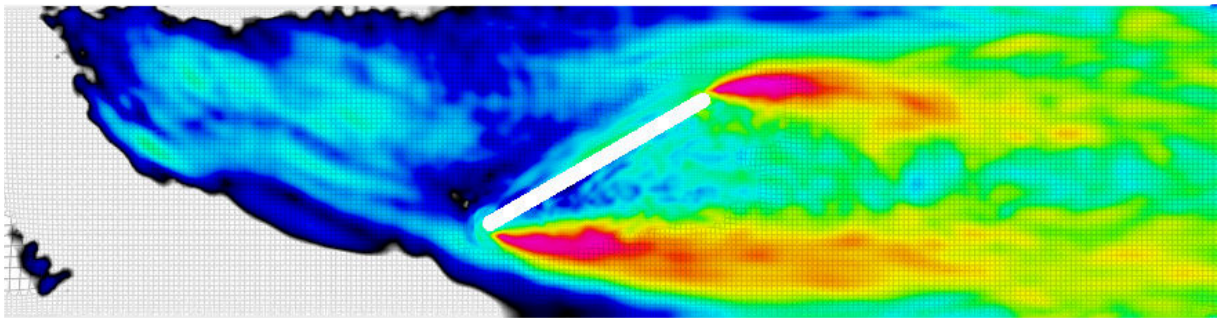

1000 Hz band

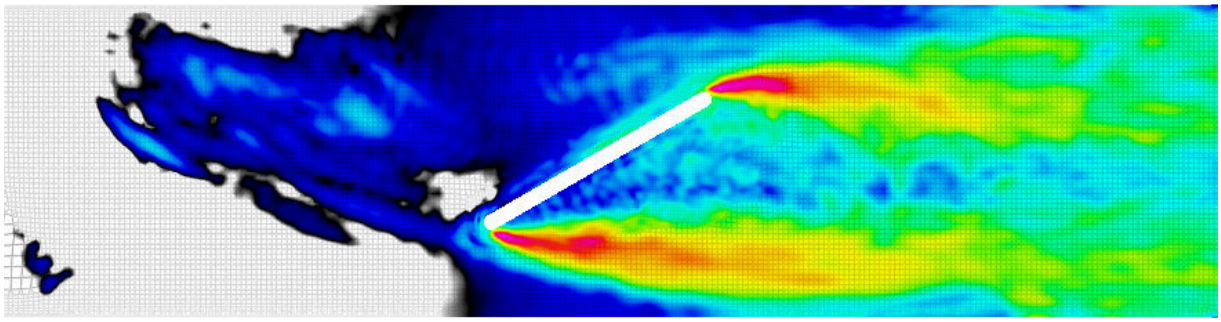

1250 Hz band

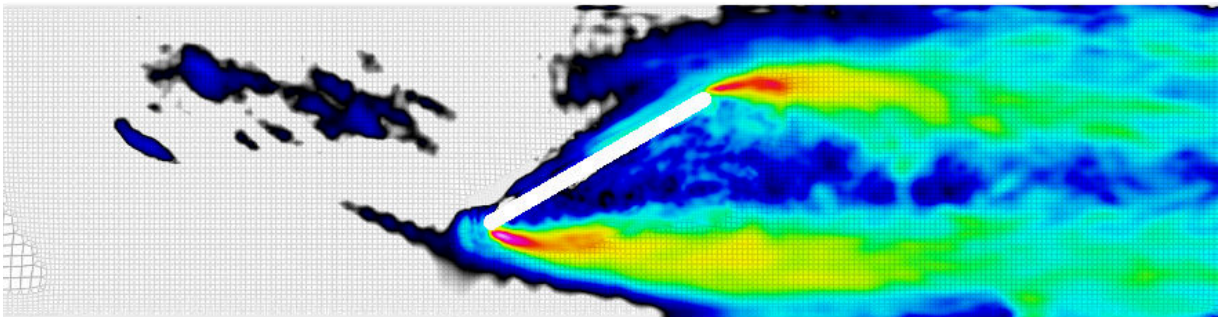

1600 Hz band

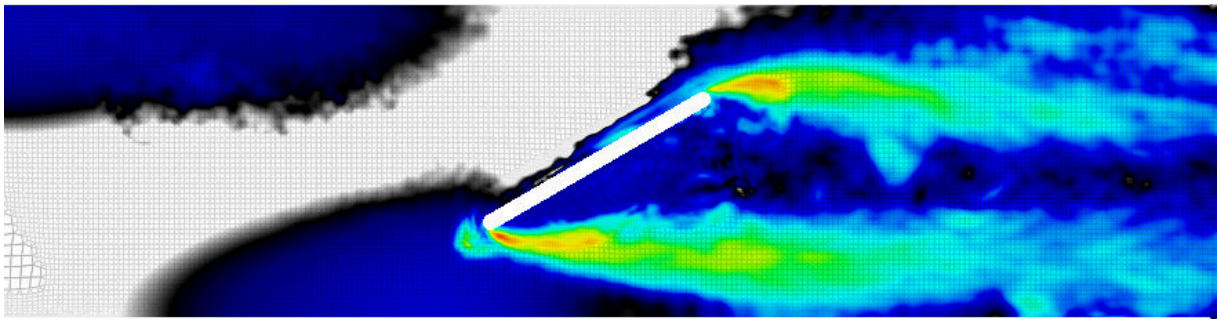

2000 Hz band

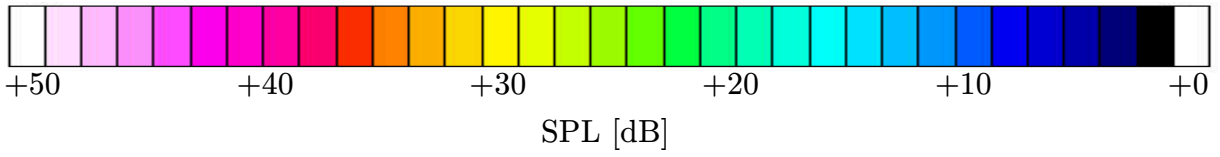

Figure 6.11: Pressure field FFT on the mid-plane, for three 1/3 Octave frequency bands.

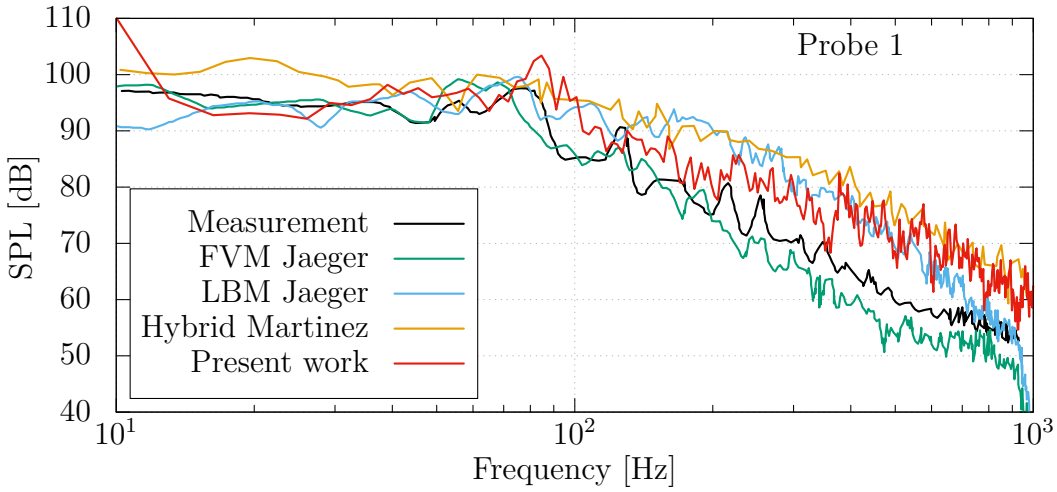

(a) Pressure fluctuation power spectrum at probe 1

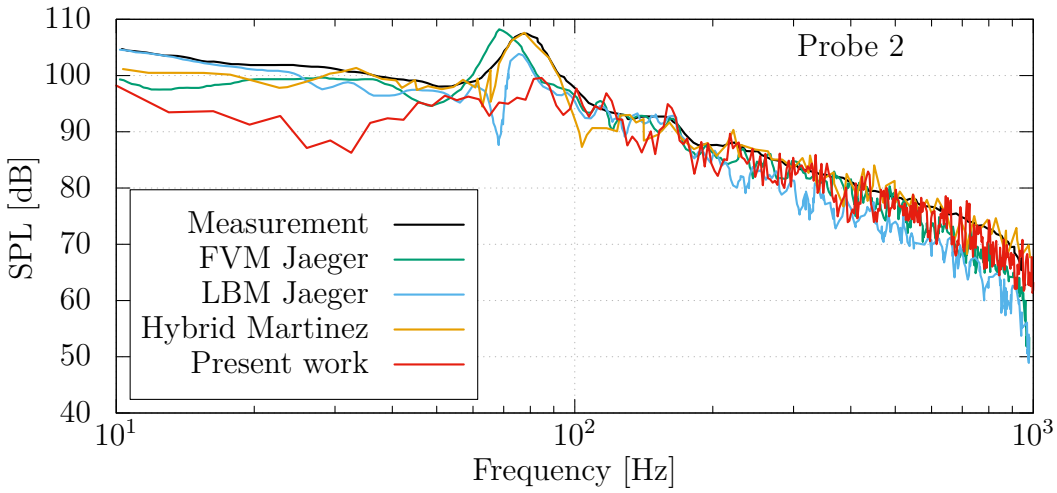

(b) Pressure fluctuation power spectrum at probe 2

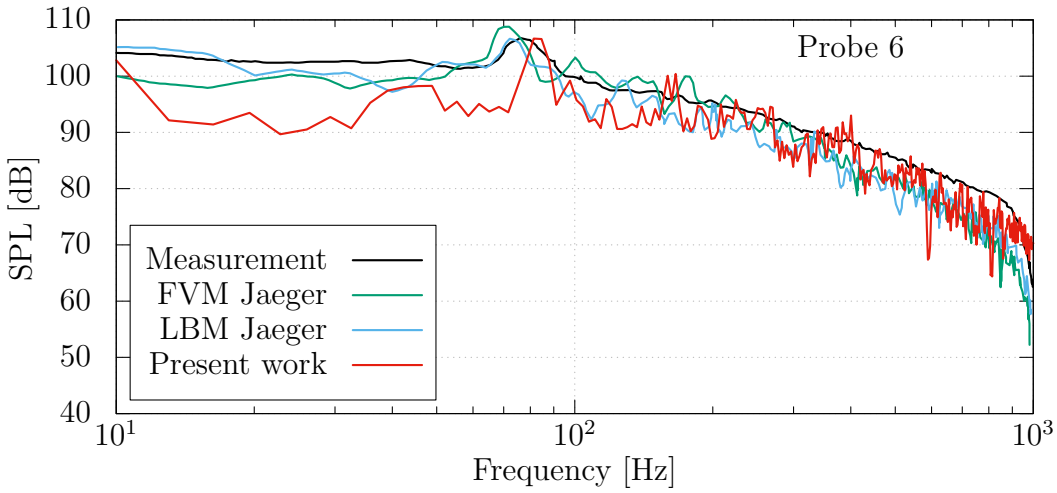

(c) Pressure fluctuation power spectrum at probe 6

Figure 6.12: Pressure fluctuation power spectra of the near-wall probes. Results of the present work are compared with experimental measurements [13], two DNC approaches based on the Finite-Volume (FVM) and Lattice-Boltzman (LBM) Method [13], and a hybrid approach based on incompressible CFD data [15]. (Non A-weighted)

Farfield Probes

The pressure field sampled at the farfield probes, shown in fig. 6.3, is also processed through FFT, using the same configurations as with the wall probes. The resulting Fourier pressure components, expressed in units of power, obtained through eq. (4.7), are then averaged, and converted to standard PSD measures, in dB/Hz units (eq. (4.8)).

The decision not to apply any pseudo-sound filtering procedure, such as the one presented in section 4.2, was made. This was concluded due to the measurement locations, stemming from the experiment publication [18], the majority of which are away from the outflow jet, thus they most possibly only capture sound waves, propagating to all directions. Also, the only results available are those corresponding to the average of all microphones, which would greatly complicate any such attempt.

The resulting spectrum, presented in fig. 6.13, does not correlate well with the published sound measurements. It seems that the frequency PSD components are misaligned with the experimental ones since the form of the two graphs is similar. More specifically, by stretching the DNC graph by multiplying all frequencies by a factor of around 1.25, the peaks at $\approx 1500\,\text{Hz}$ coincide, and the deviation is in the range of $0 - 7\,\text{dB}$. This causes suspicion of inaccuracies in the CFD solution and not in the post-processing tool since the latter was validated by commercial software and found to correlate well.

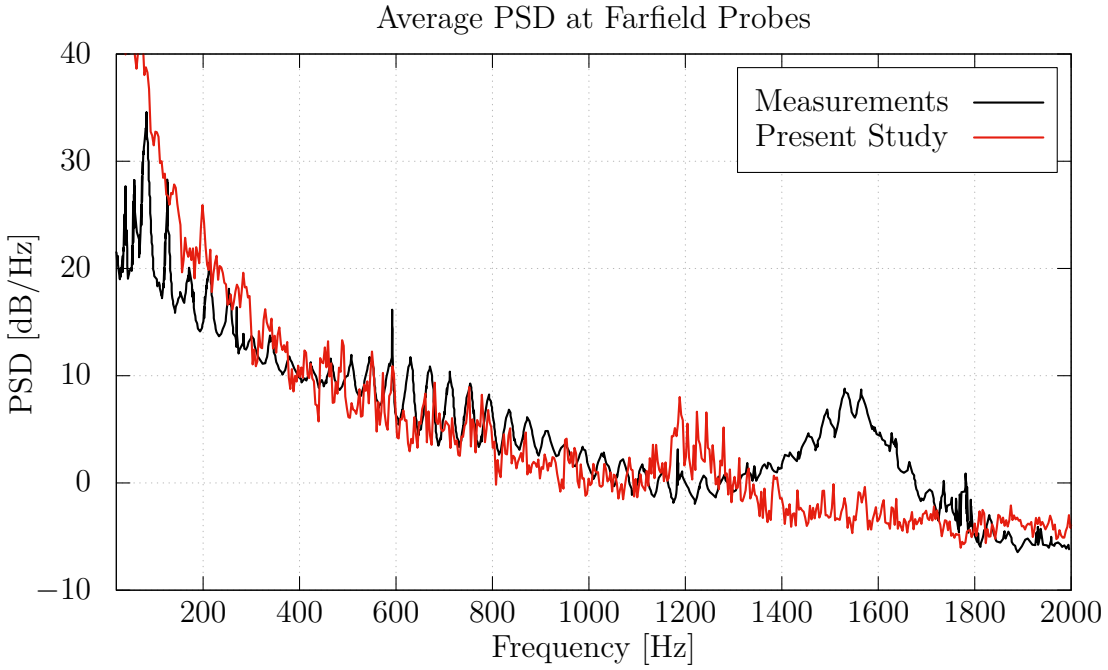

Figure 6.13: Averaged PSD spectrum at the farfield receiver locations, compared with measurements from [13], published in [14]. (Non A-weighted)

6.2 Passenger Car HVAC Blower

The DNC method is applied to the driver-side HVAC blower of a Toyota passenger car, introduced in section 5.2.1. Three of the configurations for which experimental measurements were performed (see chapter 5) are modelled and are summarized in table 6.2. The targeted frequency range is set to $0.4 - 5\,\mathrm{kHz}$.

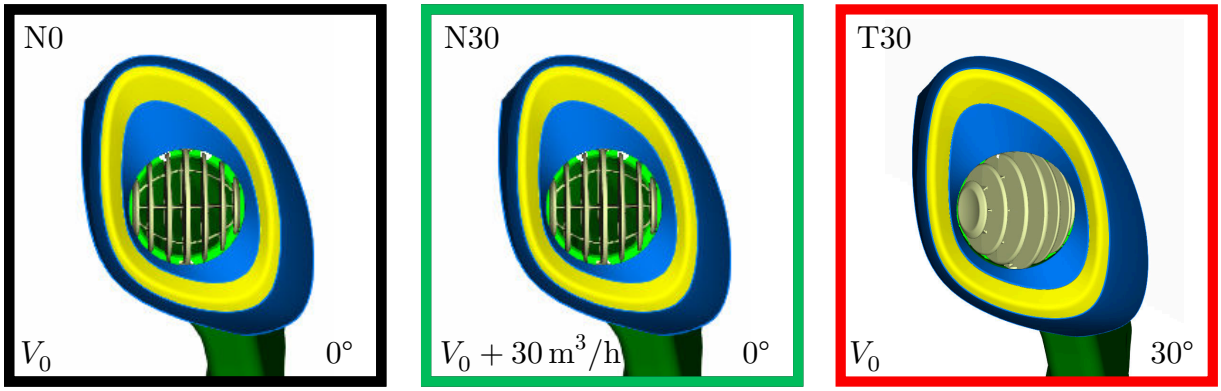

Code	Register rotation	Flowrate	Mesh/Domain
N0	0°	V_0	N
N30	0°	$V_0 + 30\,\mathrm{m}^3/\mathrm{h}$	N
T30	30°	V_0	T

Table 6.2: The three DNC simulated configurations of the isolated HVAC blower, featuring different flow-rates and register rotations.

6.2.1 Computational Domain Definition

Similarly to the simplified HVAC case of section 6.1, the inlet is extended up to a bulbous structure, which helps increase the volume in which absorption layers will be active. Furthermore, a discharge plenum is introduced, for a distance up to 2 m from the blower outlet. In all configurations, the plenum is rotated on par with the register blades, to be aligned with the air jet exiting the blower. The computational domain's defining features are displayed in fig. 6.14.

6.2.2 Pressure Sampling Locations

The pressure fluctuations computed by the CFD solution are captured and stored at 8 linear probe arrays of 512 sampling points and length L each, positioned adjacent to the jet exiting the blower (fig. 6.15). The aim is to filter the acoustic component of these fluctuations, according to the method described in section 4.2. The arrays are positioned so that their centres coincide with those of the microphones used in the experimental measurements. The resulting resolution of the wavenumber space can be derived from eq. (4.14) and is equal to $\Delta k = 1/(512\Delta x)$.

The same pressure probe configuration is used for all cases examined, in the same position relative to the register blade array and the plenum, similar to how the microphones were rotated in the experimental measurements (fig. 5.11).

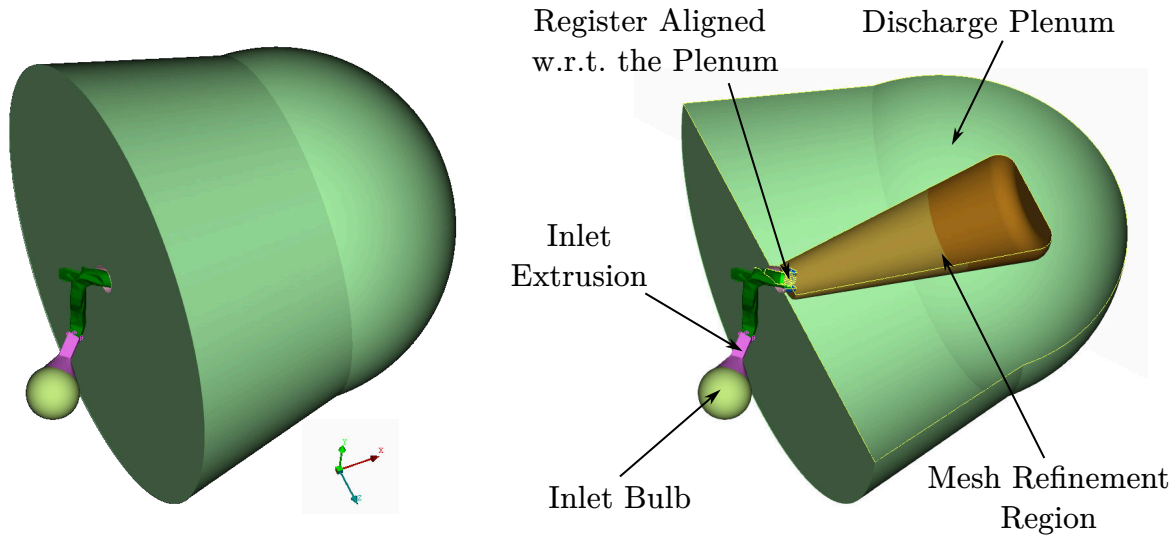

Figure 6.14: Placement of the components defining the computational domain: the inlet extrusion (pink), the inlet bulb (yellow) and the discharge plenum (green). The plenum is aligned parallel to the register both in N and T configurations for the jet exiting the blower to be located at the centre. The brown surfaces define regions of mesh refinement in which the pressure probes are placed.

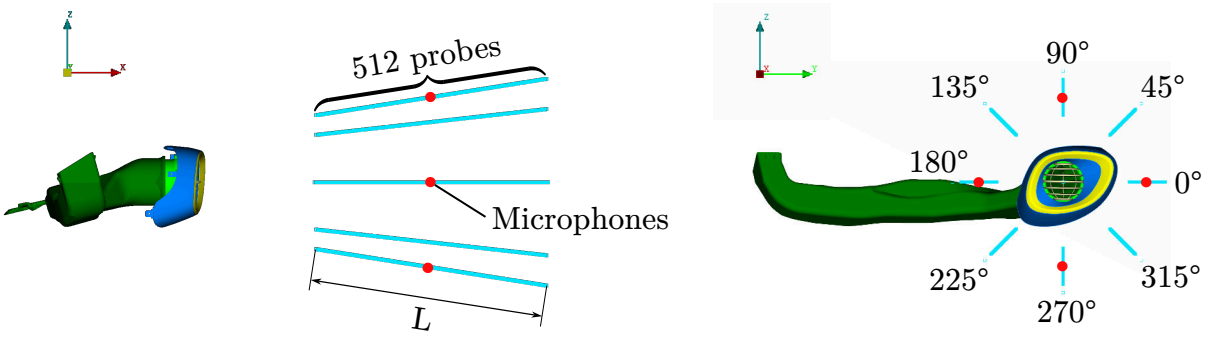

Figure 6.15: Positioning of linear probe arrays to capture the propagation of pressure fluctuations at the discharging region. 8 arrays of length L and 512 probes each were used, the centre of the 4 cardinal ones coinciding with the microphone positions employed in the measurements (see section 4.2).

6.2.3 Computational Mesh

Two different computational meshes were used for the passenger car blower, one for the rotated register case (T) and one for the non-rotated cases (N). Both were generated based on the same volume-to-surface approach described in section 6.1.4 using a commercial mesher, provided by TME. The refinement process follows the same principles in both configurations: the non-subdivided mesh has a cell height of $h_0 = 31.2\,\text{mm}$ (fig. 6.16b), which is gradually refined up to $h_6 = 0.4875\,\text{mm}$ in the region of the register blades (figs. 6.16c and 6.16d). In narrow gaps where less than 4 cells of refinement level 6 are generated, one more refinement level is added, leading to $h_7 = 0.24375\,\text{mm}$ such as in the lower-most right blade in fig. 6.16d. Inflation layers are introduced at the blower walls, with a maximum growth ratio of 1.2, to achieve values of $y^+ \approx 1$ at the first cell centres. Moreover, the region from the blower up to the pressure sampling probes (fig. 6.16a) is refined to at least $h_4 = 1.95\,\text{mm}$, translating to 35 points per acoustic wavelength, for a maximum frequency of 5 kHz.

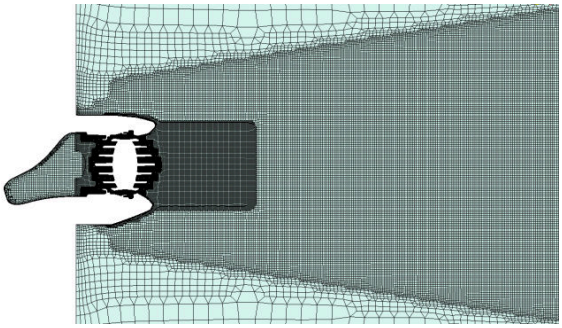

(a) Region leading up to pressure probes

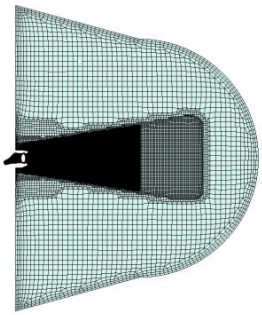

(b) Section of the complete mesh

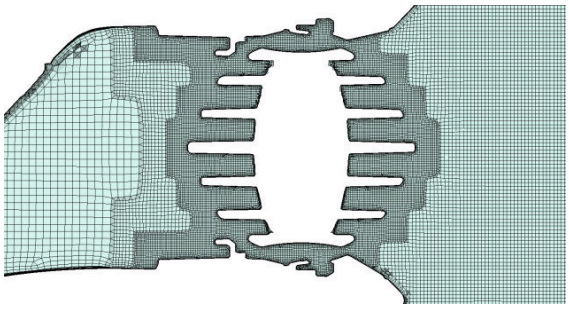

(c) Section of the N mesh at the register

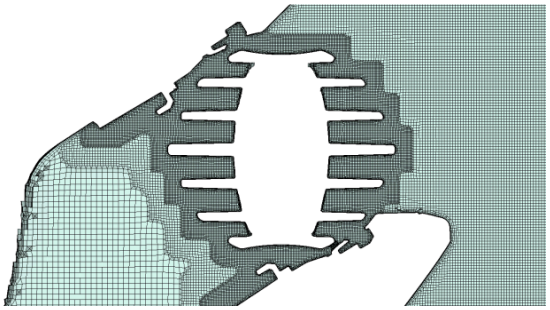

(d) Section of the T mesh at the register

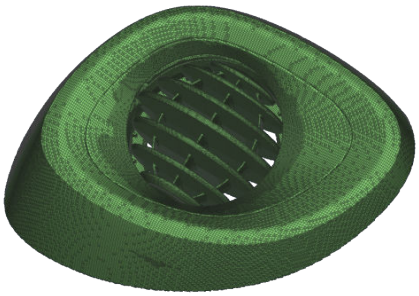

(e) Register surface mesh

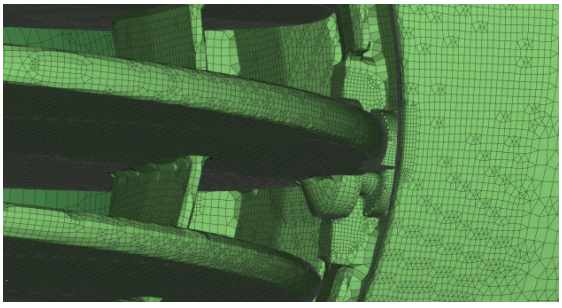

(f) close-up of the register surface mesh

Figure 6.16: Computational Mesh of the Toyota blower, for the N and T configurations.

The resulting N and T meshes are comprised of approximately 35.3 and 33.5 mil-

lion cells respectively. To block fluctuations in the flow field from generating spurious phenomena at the domain boundaries, damping regions are introduced, as discussed in section 3.6.1. The damping intensity scalar field w is defined as shown in fig. 6.17, placing the pressure probes in the non-damped region.

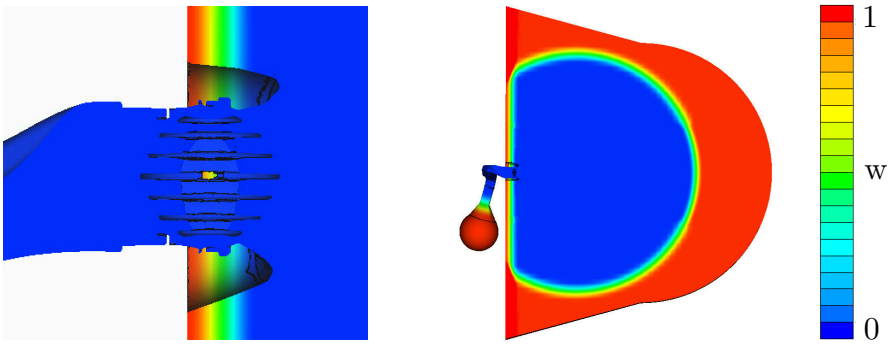

Figure 6.17: Absorption region intensity field w. Values of 1 denote full damping, while values of 0 absence of damping.

6.2.4 Boundary Conditions

The boundary conditions and fluid properties used for all 3 models are derived from section 3.7.1 and summarized in table 6.3. The inlet velocity is defined based on the volumetric flow rate of the inlet and the local density computed via the ideal gas law $\rho = p/RT$.

Region	Variable	Symbol	Value
Globally	Dynamic Viscosity	μ	$1.813 \times 10^{-5}\,\mathrm{Kg/(m\,s)}$
	Constant Pressure Heat Capacity	C_p	$1007\,\mathrm{J/(Kg\,K)}$
	Specific Gas Constant	$R_{specific}$	$287.05\,\mathrm{J/(Kg\,K)}$
Inlet	Volumetric Flow rate	$\dot{V}$	V_0 or $V_0 + 30\,\mathrm{m^3/h}$
	Turbulent Intensity	I	0.01
	Eddy Viscosity Ratio	μ_t/μ	70
	Static Temperature	T	288 K
Farfield	Total Pressure	p_t	$10^5\,\mathrm{Pa}$

Table 6.3: Boundary values and fluid properties for air, used in all configurations of the HVAC blower.

6.2.5 Results

The simulations were run initially using a RANS model for steady-state flow, initialise the flow field, followed by 0.3 s of unsteady flow simulation, with the timestep set to $\Delta t = 2.5 \times 10^{-5}$ s, leading to a sampling frequency 8 times greater than the maximum frequency of interest (5 kHz). The flow solver was run in parallel, leading to a total computational cost of 4800 CPUh for the transient and 2700 CPUh for the precursor steady solution, in 320 cores, per simulation.

The pressure was stored at the probe locations of fig. 6.15 for the last 2048 time-steps, or $T_{sample} = 0.0512\,\text{s}$. Then, the pressure fluctuations were filtered, to extract only their acoustic component, following the procedure described in section 4.2. In this way, the sound power spectra at the locations corresponding to the 4 microphones used for the experimental measurements are computed. The unfiltered and filtered sound power spectra, corresponding to the 4 cardinal microphone positions, of the N0 case are displayed in fig. 6.18. It seems that pseudo-sound is more prominent in lower frequencies, whereas from 2 kHz and higher the sampled pressure contains only acoustic fluctuations and thus filtered and unfiltered spectra coincide. This is because the mesh at the sampling region is only sufficiently refined to capture sound wave propagation and not eddies of the small scales associated with those higher frequencies.

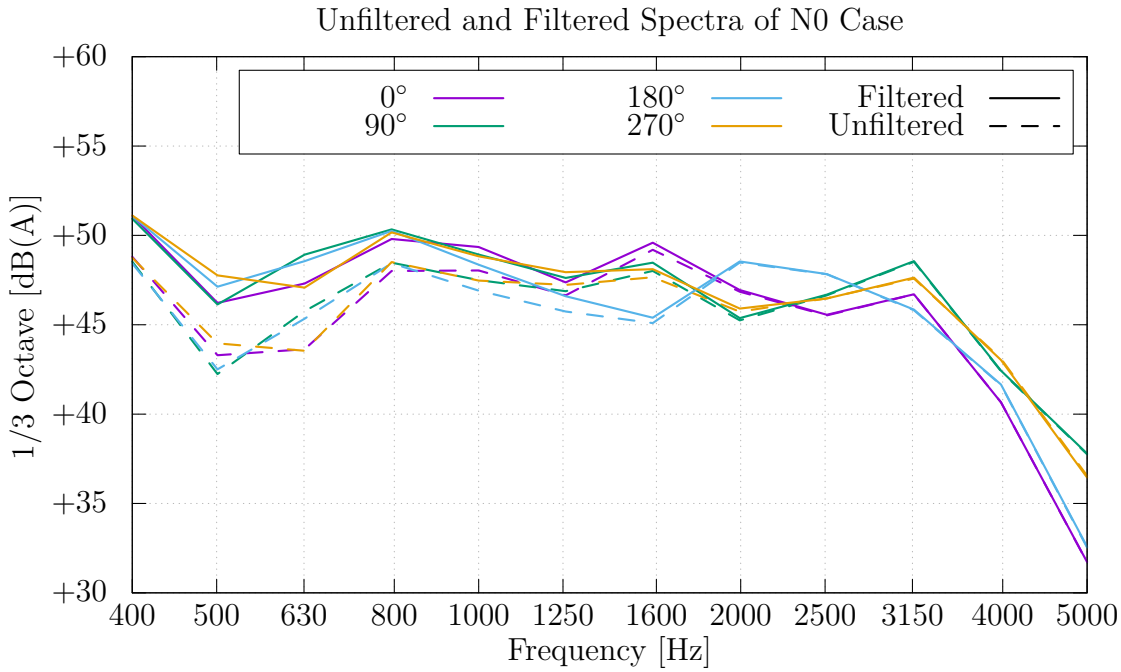

Figure 6.18: Sound power spectra in 1/3 Octave format at the 4 microphone locations for case N0. Dashed lines correspond to the raw unfiltered pressure, whereas solid lines to the filtered acoustic component only. (Relative vertical axis values)

The resulting filtered sound power spectra are averaged over the 4 microphone locations and compared with the respective experimental measurements, all of which are hereupon presented in A-weighted 1/3 Octave format, generated using a 2048 sample DFT in order to be compatible (see appendix A). The comparison between measurements (dashed lines) and numerical predictions using DNC (solid lines) is illustrated in fig. 6.19, in which an extra DNC configuration T32 is included, to be discussed below. Both N0 and N30 cases exhibit a good correlation of $\pm 4\,\text{dB}$ up to 2 kHz, after which the DNC results are increasingly under-predicting sound levels. Moreover, the increase in flow-rate results in a generally uniform increase in DNC-predicted sound, as is the case with the measurements. In the rotated configuration T30, DNC appears to underestimate the high sound-level range of $0.8 - 2\,\text{kHz}$, while completely failing to capture the second peak at around 3 kHz.

To investigate this deviation, a refinement based on the turbulent kinetic energy criterion (TKE), presented in section 3.4.2 and applied in section 6.1.5, was attempted

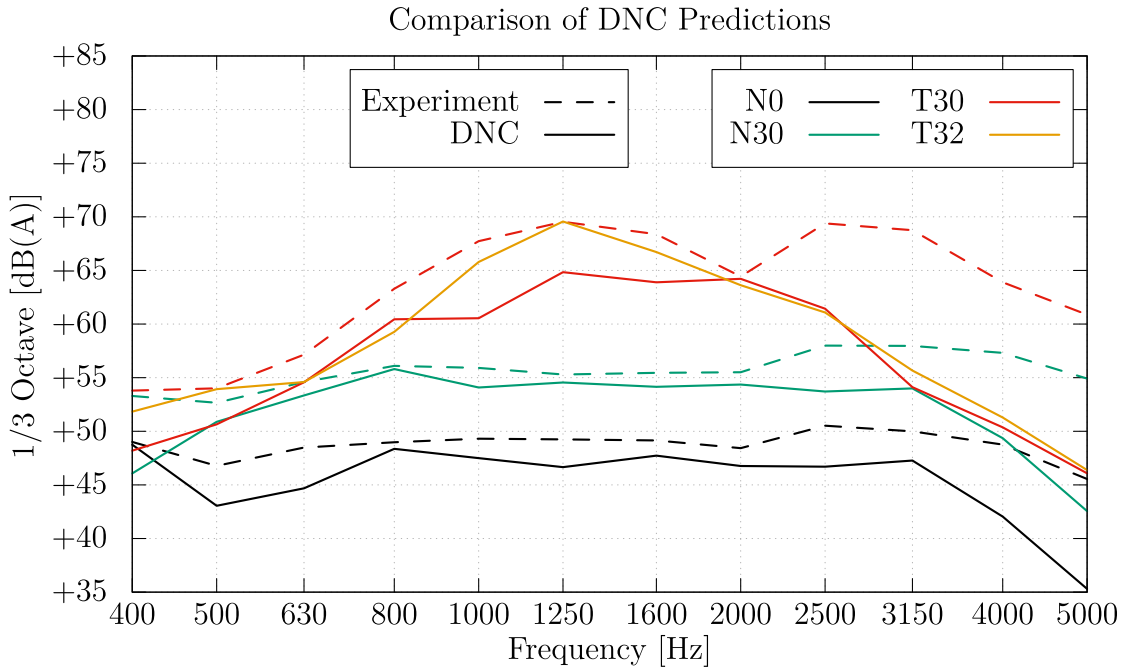

Figure 6.19: Comparison between Experimental measurements (dashed lines) and sound predictions using DNC (solid lines). Each colour corresponds to a different configuration. (Relative vertical axis values)

but did not yield any significant change.

Moreover, to examine the sensitivity w.r.t. the register blades' position, a new rotated configuration at 32°, deemed T32, with the same flowrate V_0, is meshed and simulated. The resulting microphone-averaged filtered spectrum is shown in fig. 6.19 and seems to correlate well to the T30 measurement in the range $0.4 - 2\,\text{kHz}$.

To visualise the difference between the sound-generating regions of the T configurations, the pressure field was sampled at the z-normal mid-plane of the domain and processed using DFT for both T30 and T32 cases. The pressure fluctuation power density is visualised in 1/3 Octave bands at the frequency range of interest, in fig. 6.20. The T32 case exhibits higher values downstream of the gaps between the register blades and housing, owing to the tighter clearance between the two, leading to higher velocities. Therefore, it is sensible to assume that those are the regions contributing the most to the $0.4 - 2\,\text{kHz}$ peak of the T configurations and that sound levels are sensitive to the angle of rotation.

The discrepancy between numerical prediction and experiment of the T30 case can not be coherently justified, as it can be caused both by errors in the experimental procedure, regarding the setting of the angular blade position or the flow-rate, as well as by inaccuracies in the numerical approach.

Mesh Dependency study

In an effort to examine the dependency of DNC sound-level predictions on spatial discretization, two additional meshes are generated for case N0, by increasing the initial cell edge h_0 (see section 6.2.3), leading to uniform coarsening. The coarsened meshes are denoted as NR1 and NR2 with an initial cell edge length of $0.75h_0$ and 0.75^2h_0

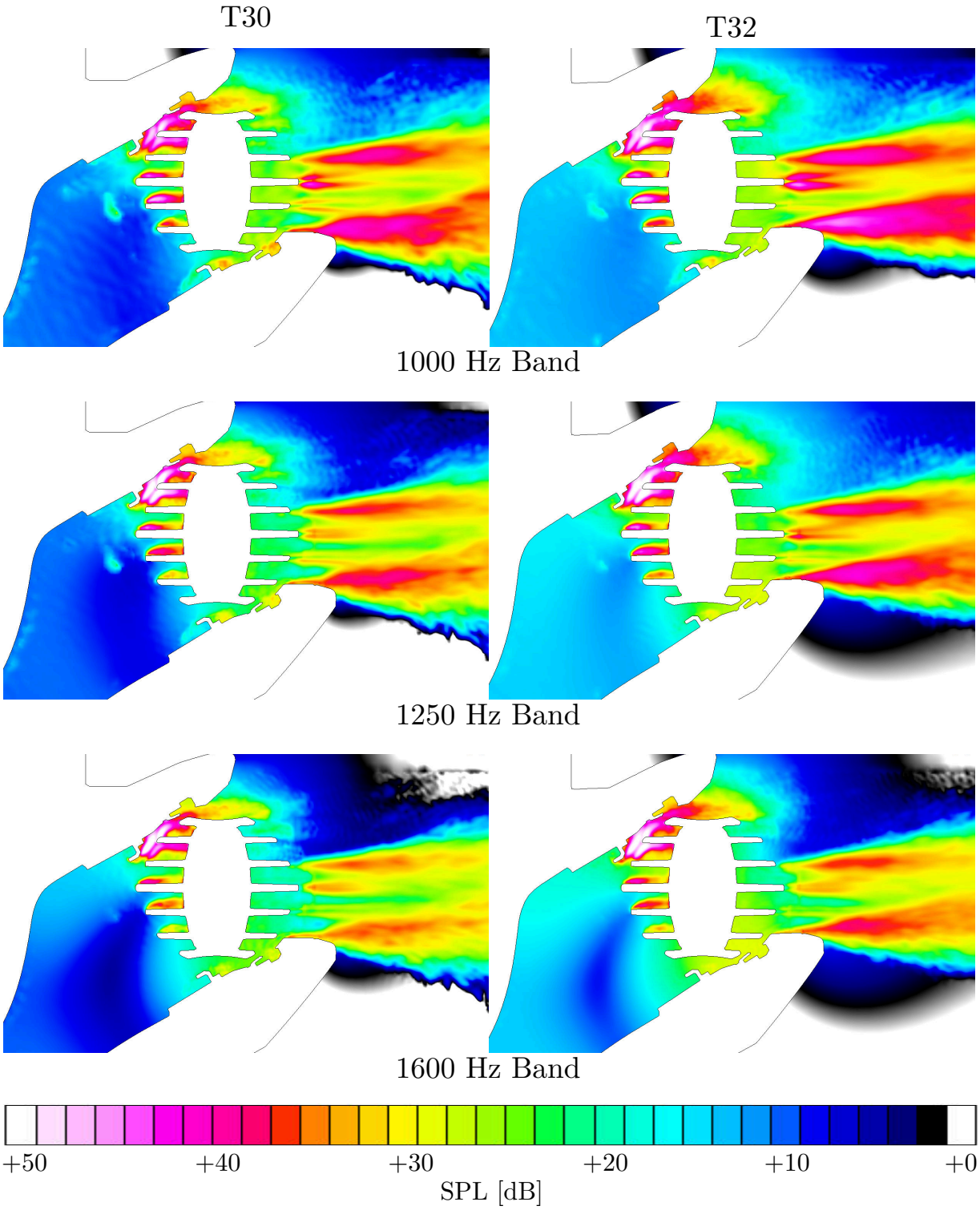

Figure 6.20: 1/3 Octave bands resulting from the DFT of the pressure field on the mid-plane at the register position, for the T30 (left) and T32 (right) configurations. Units are relative.

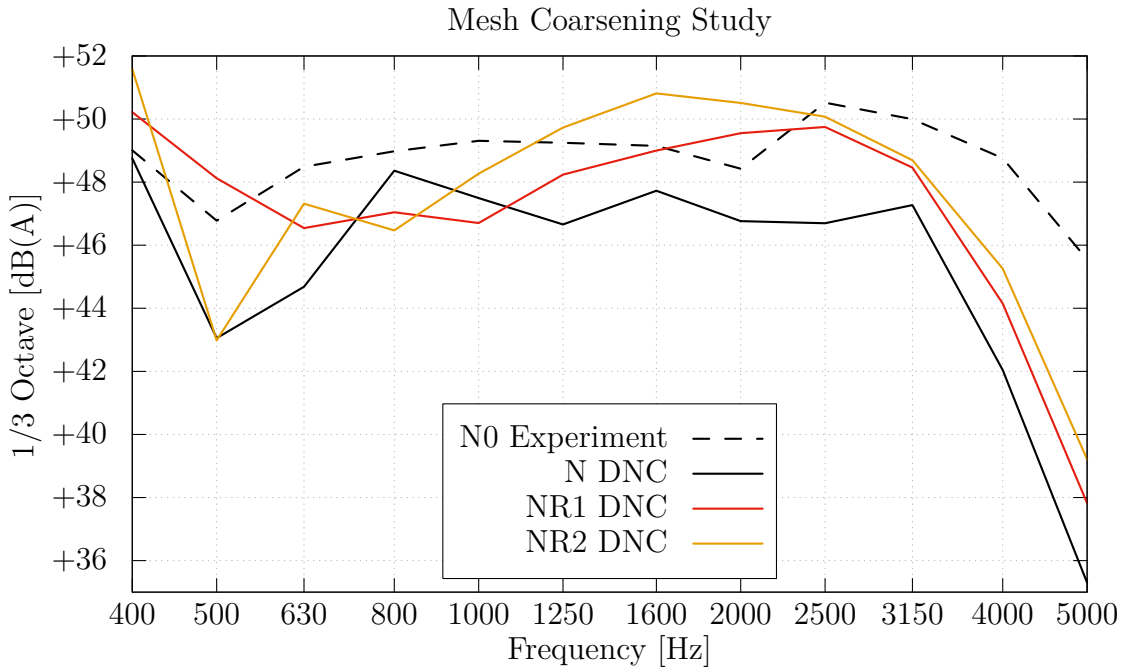

Figure 6.21: Resulting sound power spectra using the coarsened meshes NR1 and NR2. (Relative vertical axis values)

respectively. The N0 case is then simulated, using both meshes and the same constant timestep of $\Delta t = 2.5 \times 10^{-5}$ s. The resulting sound spectra, averaged over the 4 microphone positions, are presented in fig. 6.21. It appears that coarsening of the computational mesh leads to an increase in the predicted sound levels at the $1 - 3$ kHz frequency range, which while being closer to the experimental spectral curve, tends to deviate from it in a non-uniform manner.

Chapter 7

Overview and Conclusions

7.1 Overview

A direct noise computation (DNC) approach using the Finite-Volume method was implemented in OpenFOAM, to directly compute the sound generated by the flow in HVAC blowers. The flow was modelled using the unsteady compressible Navier-Stokes equations, along with the k-ω IDDES turbulence model. Sound levels were extracted using a post-processing utility developed for the needs of this work.

A new setup for the measurement of aerodynamic noise in automotive HVAC blowers was devised and implemented. The background noise present was evaluated and deemed to be at acceptable levels. The setup was then used to produce sound measurements of an industrial case, using a production part in different operating conditions, to be compared with numerical predictions.

The DNC method was applied to a test case from literature and three different operating configurations of the same industrial case. Numerical results for both cases were compared with experimental measurements.

7.2 Conclusions

The proposed DNC approach was implemented successfully and managed to produce good results when applied first in a test case and then in an industrial one. In both, numerical predictions of sound levels were in good agreement with experimental measurements for low frequencies. Furthermore, the ability of the method to predict changes in sound levels due to alterations in operating conditions was demonstrated, in the industrial case.

In the simplified HVAC case, a mismatch of the computed spectral peak between numerical prediction and measurement was observed, located in the highest frequency ranges, which is attributed to the CFD portion of the approach. Possible causes include the choice of turbulence modelling as well as inadequate domain resolution and the discretization process employed. Due to the high computational cost of such an approach, thorough parametric studies of different simulation parameters were not permitted, thus complicating the task of identifying sources of inaccuracies.

In the industrial case, under-estimation of sound levels was observed at frequencies higher than 2 kHz. This is probably attributed to insufficient spatial and temporal

discretization, prohibiting the resolution of smaller flow scales, responsible for the generation of high-frequency sound. However, in frequencies of less than 2 kHz, the DNC method was proven able to predict general trends in sound levels when different flowrates are used and even when the geometry is altered, as demonstrated by rotating the outlet flaps.

7.3 Future work Proposals

Based on the experience gained by conducting this work, proposals on areas for further research can be summarised as follows:

Direct Noise Computation:

- Investigation of the effects of spatial and temporal discretization on maximum resolved frequency, using the same second-order accurate numerical schemes, by performing concise parametric studies.
- Extension to higher order numerical schemes, to better capture the low energy propagation of sound waves in the computation domain.
- Examination of the effects of turbulence modelling on resolving sound-generating flow structures, by employing different turbulence models.
- Develop a method to visualise and recognise regions important to sound generation, through the flow fields computed by the present method.

Alternative methods:

- Application of hybrid methods based on incompressible CFD data, which have the potential to decrease computational cost and numerical complexity of the flow solution, while not significantly impacting accuracy.

Appendix A

Narrowband to 1/b Octave Conversion

Fractional Octave bands, offer a useful way to divide the frequency scale into a finite number of bins, i.e. ranges of frequencies. 1/b Octave bands are defined by three frequencies, the lower f_l, the middle f_m and the upper one f_u, following

$$\frac{f_u}{f_l} = 2^{1/b} \tag{A.1}$$

$$\left(f_u f_l\right)^{1/2} = f_m \tag{A.2}$$

Where $1/b$ stands for the octave order. Owing to their geometrically scaling nature, Octave bins appear equidistant and with equal length in logarithmically spaced plots. Nominal Octave and 1/3 Octave mid-band frequencies are defined in IEC 61260 [57] and presented in table A.1.

Octave	1/3 Octave	Octave	1/3 Octave	Octave	1/3 Octave
	16		200		1600
31.5	31.5	250	250	2000	2000
	40		315		2500
	50		400		3150
63	63	500	500	4000	4000
	80		630		5000
	100		800		6300
125	125	1000	1000	8000	8000
	160		1250		10000

Table A.1: Nominal Octave and 1/3 Octave mid-band frequencies in Hz, as defined in IEC 61260 [57].

Narrowband spectra, with frequency bins of constant width, such as the ones generated by DFT, essentially represent the content of each frequency bin by a single value. Similarly, octave spectra use one value for each octave band. Conversion from narrowband spectra, to 1/b Octave spectra, can be done using band bass filters, appropriately weighing and summing the energy content of the narrowband frequency bins that fall into each octave band.

The 1/b octave filter for mid-band frequency f_m is defined as a gain function both in absolute g and logarithmic units G:

$$G(f, f_m, b) = 10 \log_{10}(g^2(f, f_m, b)) \tag{A.3}$$

$$g(f, f_m, b) = \left[1 + \left(\left[\frac{f}{f_m} - \frac{f_m}{f}\right] 1.507b\right)^6\right]^{-\frac{1}{2}} \tag{A.4}$$

Some of the 1/3 Octave band-pass filters are displayed in fig. A.1 in dB units.

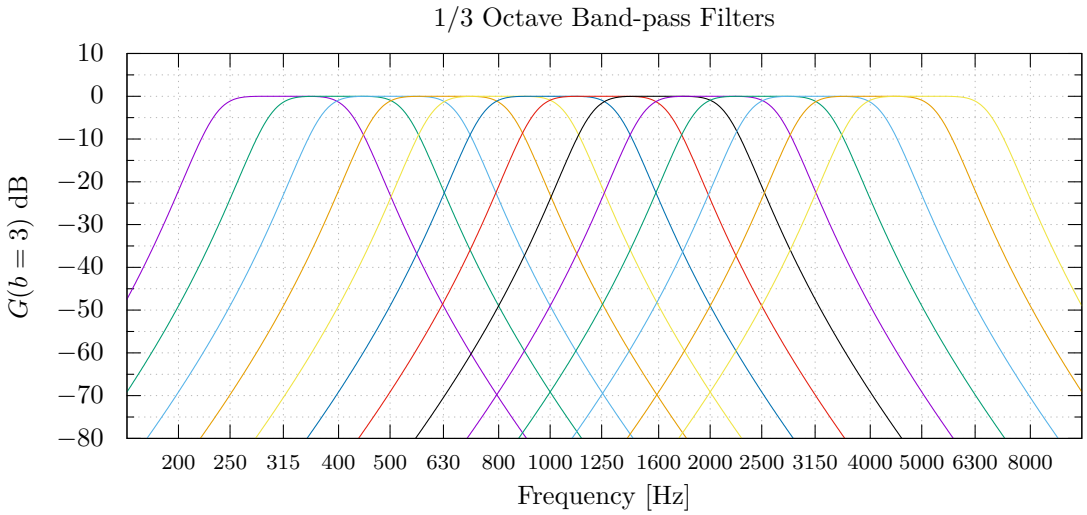

Figure A.1: 1/3 Octave band-pass filters for some mid-band frequencies, in dB units.

To convert narrowband spectra to 1/b Octave ones, the power of each frequency band with mid-frequency f_m is calculated as:

$$\hat{p}'^2_{f_m} = \sum_{n=0}^{N} \hat{p}'^2_{f_n} g(f_n, f_m, b) \tag{A.5}$$

where f_n is the central frequency of each narrowband bin. The reader should note that the above definition leads to 1/b Octave spectral values dependent on the number of discrete frequency values of the initial narrowband spectrum. Hence, for any comparison between two 1/b Octave spectra to be meaningful, the same number of narrowband frequency bands should be used for their generation.

Εκτενής Περίληψη Διπλωματικής Εργασίας

1 Εισαγωγή

Η συνεχόμενη βελτίωση της ακουστικής συμπεριφοράς των επιβατικών αυτοκινήτων, φέρνει στο προσκήνιο πηγές ηχητικής όχλησης μικρής, μέχρι τώρα, σημασίας, όπως τα συστήματα κλιματισμού [1, 2].

Ο θόρυβος στο εσωτερικό ενός επιβατικού οχήματος προέρχεται, μεταξύ άλλων από τη ροή του αέρα στο εξωτερικό του, την κύλιση των ελαστικών, την κινητήρια μηχανή, και το σύστημα κλιματισμού [2]. Ειδικότερα όσον αφορά τα ηλεκτρικά αυτοκίνητα, υπάρχουν περιπτώσεις όπου ο εκπεμπόμενος ήχος από το σύστημα κλιματισμού, αποτελεί τη μοναδική πηγή θορύβου στο εσωτερικό του οχήματος, ιδιαιτέρως αν αυτό είναι ακινητοποιημένο (σχ. 1).

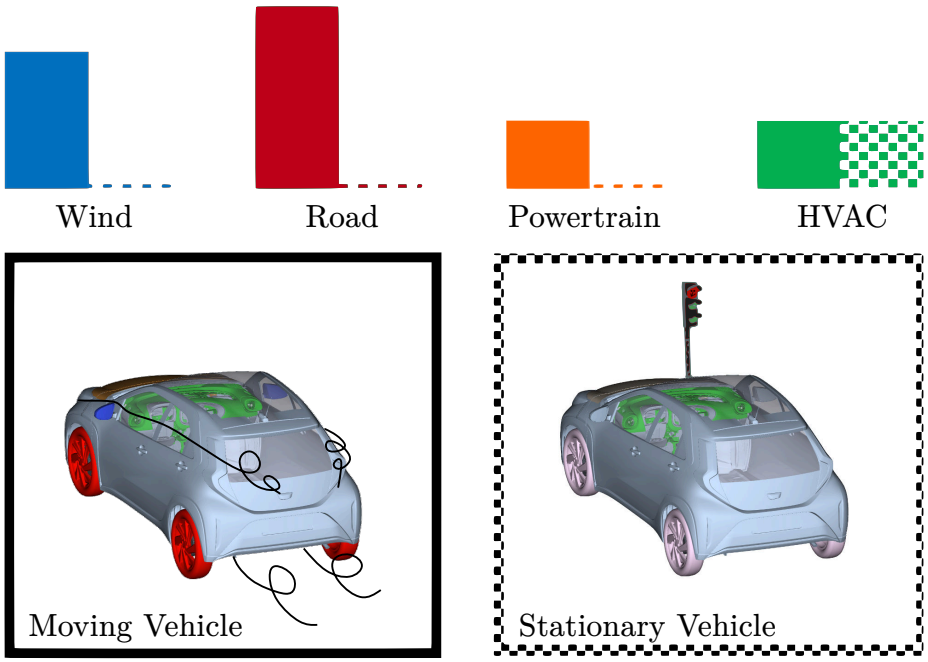

Σχήμα 1: Σύνθεση πηγών ηχητικής όχλησης στην καμπίνα ηλεκτρικού αυτοκινήτου όταν αυτό κινείται (αριστερά) και όταν είναι ακινητοποιημένο (δεξιά). (από TME)

Ως αποτέλεσμα, παρατηρείται ενδιαφέρον πολλών αυτοκινητοβιομηχανιών για υπολογιστικές μεθόδους πρόβλεψης θορύβου, ικανών να προσφέρουν χρήσιμες πληροφορίες για τα χαρακτηριστικά τέτοιων συστημάτων, ακόμα και κατά τη φάση σχεδιασμού.

2 Μέθοδοι Υπολογιστικής Αεροακουστικής για συστήματα Κλιματισμού

Σημαντικό μέρος του παραγόμενου θορύβου σε συστήματα κλιματισμού, οφείλεται στη ροή αέρα μέσα σε αυτά και στον επαγόμενο αεροδυναμικό ήχο από τη ροή [2], στον οποίο εστιάζεται αποκλειστικά η εργασία αυτή.

Αεροδυναμικός είναι ο ήχος που παράγεται από μη-μόνιμες ροές [4]. Οφείλεται σε τυρβώδεις και στροβιλώδεις διαταραχές, λόγω ασταθειών και αλληλεπιδράσεων του ρευστού με στερεά τοιχώματα, οι οποίες γεννούν ηχητικά κύματα, δηλαδή διαδιδόμενες διαταραχές πίεσης και πυκνότητας [5].

Η μελέτη και προσομοίωση αυτού του αντικειμένου υπάγεται στον κλάδο της Υπολογιστικής Αεροακουστικής και είναι ιδιαίτερα απαιτητική, καθώς πραγματεύεται δύο διαφορετικούς φυσικούς μηχανισμούς σε σύζευξη, ήτοι την ακουστική και την αεροδυναμική. Αυτό οφείλεται σε θεμελιώδεις διαφορές μεταξύ των δύο, χαρακτηριστικό παράδειγμα οι αρκετά διαφορετικές φυσικές κλίμακες στις οποίες εκφράζονται [5, 9–11], ιδιαίτερα σε εφαρμογές χαμηλών αριθμών Mach [5].

Οι υπολογιστικές μέθοδοι πρόβλεψης αεροδυναμικά επαγόμενου ήχου χωρίζονται σε δύο γενικές κατηγορίες, τις άμεσες (direct) και τις υβριδικές (hybrid) [10]. Οι άμεσες μέθοδοι αντιμετωπίζουν ταυτόχρονα τη διάδοση του ήχου και τη ροή που επιφέρει τη γένεσή του, μέσω μεθόδων Υπολογιστικής Ρευστοδυναμικής, επιλύοντας τις εξισώσεις Navier-Stokes για μη-μόνιμες συμπιεστές ροές. Στις υβριδικές μεθόδους, με γνώμονα τις διαφορές μεταξύ ακουστικής και αεροδυναμικής, οι δύο αυτοί κλάδοι αντιμετωπίζονται [11] με διαφορετικά μοντέλα, τα οποία δύνανται να είναι καλύτερα προσαρμοσμένα στα χαρακτηριστικά του εκάστοτε φυσικού προβλήματος [10]. Πιο συγκεκριμένα, πραγματοποιείται προσομοίωση της συμπιεστής ή ασυμπίεστης ροής απ' όπου υπολογίζονται τα μεγέθη της, που μέσω μεθόδων βασισμένων σε ακουστικές αναλογίες μετατρέπονται σε ισοδύναμες ηχητικές πηγές. Βάσει αυτών, επιλύεται (σε τελευταίο στάδιο) το πρόβλημα της διάδοσης του ήχου, ώστε να προκύψει η τελική ακουστική πρόβλεψη (σχ. 2). Για περισσότερες λεπτομέρειες σχετικά με μεθόδους Υπολογιστικής Αεροακουστικής, ο αναγνώστης παραπέμπεται στα υποκεφάλαια 1.3 και 2.3 του πρωτότυπου κειμένου, στην αγγλική.

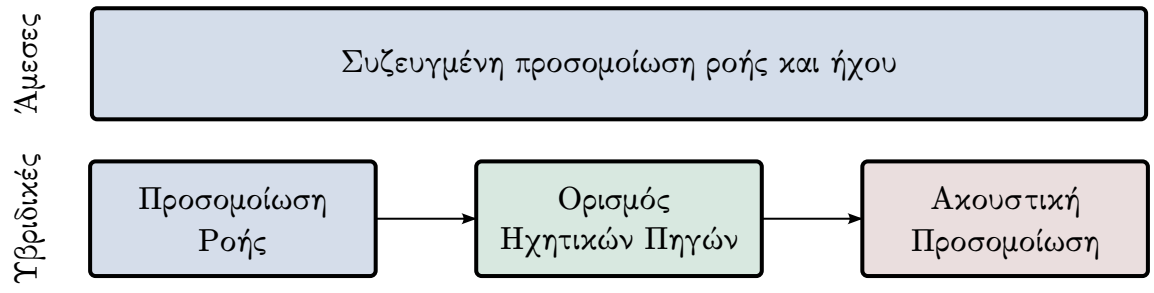

Σχήμα 2: Διαφορετική αντιμετώπιση ροής και ακουστικής μεταξύ άμεσων και υβριδικών μεθόδων.

3 Άμεσος Υπολογισμός Θορύβου με Χρήση της Μεθόδου Πεπερασμένων Όγκων

Στην εργασία αυτή υλοποιείται μία άμεση προσέγγιση, βασισμένη σε μεθόδους Υπολογιστικής Ρευστοδυναμικής (ΥΡΔ) για συμπιεστές μη-μόνιμες ροές. Για αυτόν τον σκοπό, γίνεται χρήση του ανοιχτού λογισμικού OpenFOAM® [22] με το οποίο επιλύονται οι εξισώσεις ροής με τη μέθοδο των πεπερασμένων όγκων.

Για τον υπολογισμό του παραγόμενου από τη ροή ήχου, είναι αναγκαία η αποτύπωση των μη-μόνιμων χαρακτηριστικών της ροής, μεταξύ των οποίων είναι και τυρβώδεις δίνες [10]. Αυτή η απαίτηση εισάγει δυσκολίες, καθώς ο τυρβώδης χαρακτήρας της ροής εκφράζεται σε μεγάλο εύρος χρονικών και χωρικών κλιμάκων. Πιο συγκεκριμένα, ο Kolmogorov [26] έδειξε ότι ο λόγος των μεγαλύτερων L προς τις μικρότερες η κλίμακες τοπικά ισοτροπικής τύρβης, ισούται με $L/\eta \sim \mathrm{Re}^{3/4}$, όπου Re ο αριθμός Reynolds της ροής. Επιπρόσθετα, η συχνότητα του παραγόμενου ήχου από τυρβώδεις δίνες είναι αντιστρόφως ανάλογη του χαρακτηριστικού τους μήκους [5]. Ως εκ τούτου, προσομοίωση της γένεσης ήχου υψηλών συχνοτήτων, μεταφράζεται σε υψηλές υπολογιστικές απαιτήσεις, λόγω απαραίτητης εκλέπτυνσης του υπολογιστικού πλέγματος.

Γι' αυτόν τον λόγο, στην εργασία, χρησιμοποιούνται τεχνικές μοντελοποίησης τύρβης. Ειδικότερα, εφαρμόζεται ένα μοντέλο της κατηγορίας προσομοίωσης αποκολλημένων δινών (Detached Eddy Simulation) και συγκεκριμένα το k-ω IDDES [44], το οποίο επιτρέπει την αποτύπωση των μεγαλύτερων κλιμάκων τυρβωδών διαταραχών, ενώ παράλληλα οι μικρότερες μοντελοποιούνται παρόμοια με τις εξισώσεις RANS (Reynolds-Averaged Navier-Stokes) [10]. Με αυτόν τον τρόπο, αγνοείται ο ήχος που οφείλεται σε πολύ μικρές κλίμακες, ενώ επιλύονται άμεσα οι μικρότερης συχνότητας διαταραχές και ο παραγόμενος από αυτές ήχος.

Το όριο μεταξύ μοντελοποιημένης και επιλυμένης τύρβης δεν είναι ρητά ορισμένο, και εξαρτάται από παράγοντες όπως η χωρική και η χρονική διακριτοποίηση των ροϊκών εξισώσεων [10]. Ένα κριτήριο που χρησιμοποιήθηκε για την αξιολόγηση της καταλληλότητας του υπολογιστικού πλέγματος, ως προς το περιθώριο που αυτό προσφέρει για την αποτύπωση των τυρβωδών δινών, είναι το ποσοστό της τυρβώδους κινητικής ενέργειας που αντιστοιχεί στην πλήρως επιλυμένη τύρβη [12]. Συνοπτικά, αναφέρεται ότι πραγματοποιώντας μία αρχική προσομοίωση της ροής, μπορεί να υπολογιστεί μία μετρική, η οποία υποδηλώνει τις περιοχές που χρήζουν εκλέπτυνσης του πλέγματος. Περισσότερες λεπτομέρειες σχετικά με τις τεχνικές αυτές, μπορούν να αναζητηθούν στα υποκεφάλαια 3.3 και 3.4.2.

Ακόμα ένα σημείο ενδιαφέροντος στον Άμεσο Υπολογισμό Θορύβου, είναι οι απαιτήσεις διακριτοποίησης του υπολογιστικού χώρου που μεσολαβεί μεταξύ των περιοχών γένεσης και των σημείων λήψης των διαταραχών πίεσης, δηλαδή του ήχου. Πολύ αραιή διακριτοποίηση μπορεί να επιφέρει εξασθένηση και διαστρέβλωση των ηχητικών κυμάτων, καθώς αυτά διαδίδονται στο υπολογιστικό χωρίο [10, 35] (βλέπε κεφάλαιο 3).

Η ακριβής διατύπωση των εξισώσεων που διέπουν τη ροή, των οριακών συνθηκών, των μεθόδων διακριτοποίησης, καθώς και άλλα σχετικά ζητήματα της προτεινόμενης προσέγγισης, παρουσιάζονται στο κεφάλαιο 3 του πρωτότυπου κειμένου.

3.1 Μετα-επεξεργασία υπολογιζόμενων ηχητικών σημάτων

Στη μέθοδο του άμεσου υπολογισμού θορύβου (DNC), οι ακουστικές διαταραχές που συ-

ντελούν τον ήχο εκφράζονται ως διαταραχές στο πεδίο πίεσης, υπολογιζόμενες μέσω της επίλυσης του προβλήματος Υπολογιστικής Ρευστοδυναμικής. Για την αξιολόγηση των επιπέδων θορύβου, καθώς και της κατανομής του στο φάσμα συχνοτήτων, πραγματοποιείται επεξεργασία των υπολογισμένων χρονοσειρών πίεσης μέσω ανάλυσης Fourier [24], και συγκεκριμένα, χρήση του διακριτού μετασχηματισμού Fourier (Discrete Fourier Transform) [48, 49] . Η εν λόγω επεξεργασία έγινε με λογισμικό που αναπτύχθηκε σε γλώσσα προγραμματισμού Python™, στο πλαίσιο της παρούσας εργασίας. Η σχετική μεθοδολογία παρουσιάζεται αναλυτικά στο κεφάλαιο 4.

4 Πειραματικές Μετρήσεις σε Αγωγούς Κλιματιστικών Αυτοκινήτων

Με στόχο την αξιολόγηση των αριθμητικών προβλέψεων, προτείνεται και υλοποιείται, στο πλαίσιο της παρούσας εργασίας, μια νέα πειραματική διάταξη για τη λήψη ηχητικών μετρήσεων σε αγωγούς συστημάτων κλιματισμού επιβατικών αυτοκινήτων. Χρησιμοποιείται για λήψη μετρήσεων σε πραγματικό αγωγό αυτοκινήτου, εξομοιώνοντας διαφορετικές καταστάσεις λειτουργίας του.

Η γεωμετρία που χρησιμοποιήθηκε παραχωρήθηκε από την TME και αποτελείται από έναν αγωγό κλιματισμού επιβατικού αυτοκινήτου στην πλευρά του οδηγού (σχ. 3).

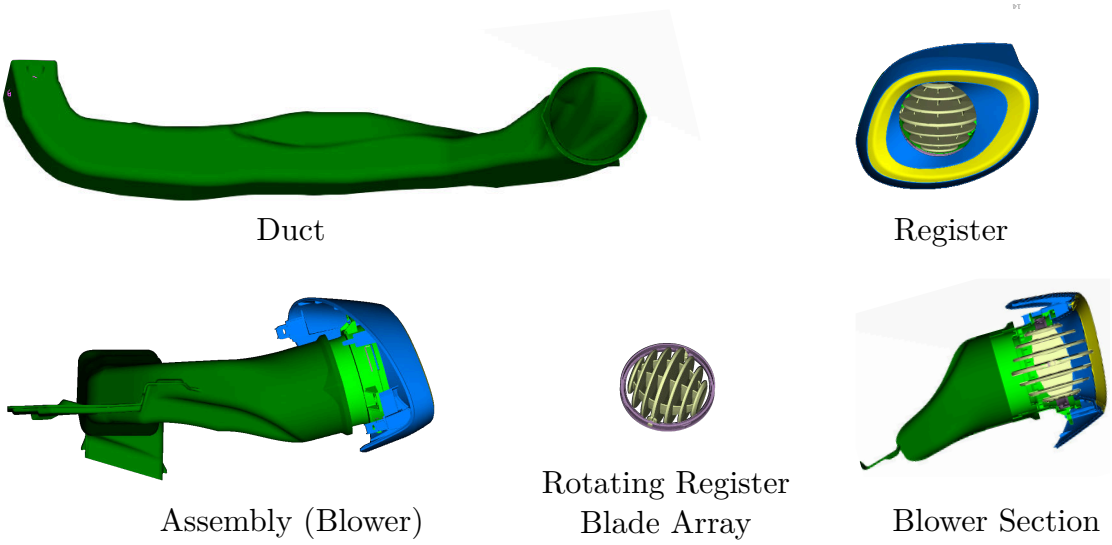

Σχήμα 3: Αγωγός συστήματος κλιματισμού επιβατικού αυτοκινήτου της Toyota. Τα επιμέρους εξαρτήματα είναι: ο *κύριος αγωγός* (πάνω αριστερά) και το *ακροφύσιο* (πάνω δεξιά) μέσω του οποίου ο αέρας εισέρχεται στην καμπίνα. Το ακροφύσιο διαθέτει ενιαίο μηχανισμό διεύθυνσης της ροής (*περσίδες*) (κάτω κεντρικά).

Για να είναι σκόπιμη οποιαδήποτε σύγκριση μεταξύ πειραματικών και αριθμητικών αποτελεσμάτων, πρέπει να εξασφαλισθούν τα χαμηλά επίπεδα θορύβου βάθους στη μετρητική διάταξη. Κυριότερη πηγή τέτοιου θορύβου αποτελεί, εν δυνάμει, το μηχάνημα παροχής αέρα, ο ήχος από το οποίο θα μπορούσε να φτάσει στα μετρητικά μικρόφωνα είτε μέσω των οδηγών σωληνώσεων, είτε άμεσα μέσω του περιβάλλοντος αέρα. Για την εξασφάλιση χαμηλών επιπέδων θορύβου βάθους, προτάθηκε και κατασκευάστηκε, στο πλαίσιο της εργασίας, η διάταξη του σχήματος 4. Ο μετρούμενος αγωγός βρίσκεται σε ανηχωικό θάλαμο,

ενώ ο παρέχων τη ροή φυσητήρας βρίσκεται εκτός του. Μεταξύ των δύο, παρεμβάλλονται δύο σιγαστήρες ροής, με στόχο την εξασθένηση-απορρόφηση του ήχου που ταξιδεύει μέσω του αγωγού. Ακόμα, παρεμβάλλονται εύκαμπτοι συνδετήριοι αγωγοί, ώστε να εμποδιστεί η διάδοση κραδασμών μέσω των τοιχωμάτων των σωλήνων.

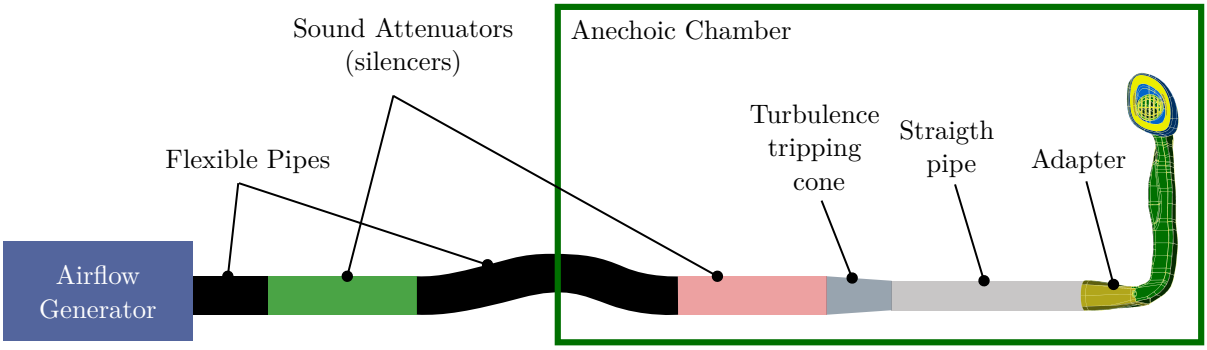

Σχήμα 4: Γραφική απεικόνιση της πειραματικής διάταξης.

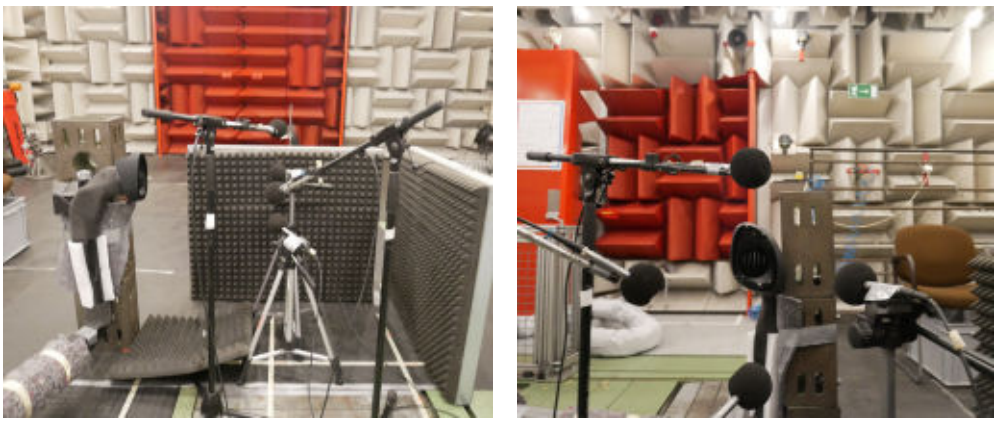

Σχήμα 5: Θέσεις των τεσσάρων μικροφώνων.

Ο θόρυβος στην έξοδο του αγωγού μετράται με χρήση τεσσάρων πυκνωτικών μικροφώνων (σχ. 5). Ακριβέστερη περιγραφή της διάταξης καθώς και των αποτελεσμάτων της διερεύνησης του θορύβου βάθους μπορούν να αναζητηθούν στο κεφάλαιο 5 του πρωτότυπου.

Πραγματοποιήθηκαν διαφορετικές μετρήσεις, προσομοιώνοντας διάφορες καταστάσεις λειτουργίας του αγωγού, οι οποίες θα χρησιμοποιηθούν για αξιολόγηση των αριθμητικών αποτελεσμάτων στην ίδια γεωμετρία. Ενδεικτικά, στο σχ. 6 παρουσιάζονται τα υπολογισθέντα φάσματα ηχητικής ισχύος, για μετρήσεις υπό διαφορετικές παροχές αέρα στον αγωγό (σε μονάδες m^3/h).

5 Εφαρμογές

Η προτεινόμενη αριθμητική μέθοδος της άμεσης πρόβλεψης θορύβου, εφαρμόζεται πρώτα σε μία απλοποιημένη γεωμετρία αγωγού κλιματισμού εκ της βιβλιογραφίας. Σε αυτή έχουν πραγματοποιηθεί και δημοσιευθεί μετρήσεις [13, 14], οι οποίες ψηφιοποιήθηκαν και χρησιμοποιήθηκαν για τη σύγκριση με τα αριθμητικά αποτελέσματα που προέκυψαν κατά

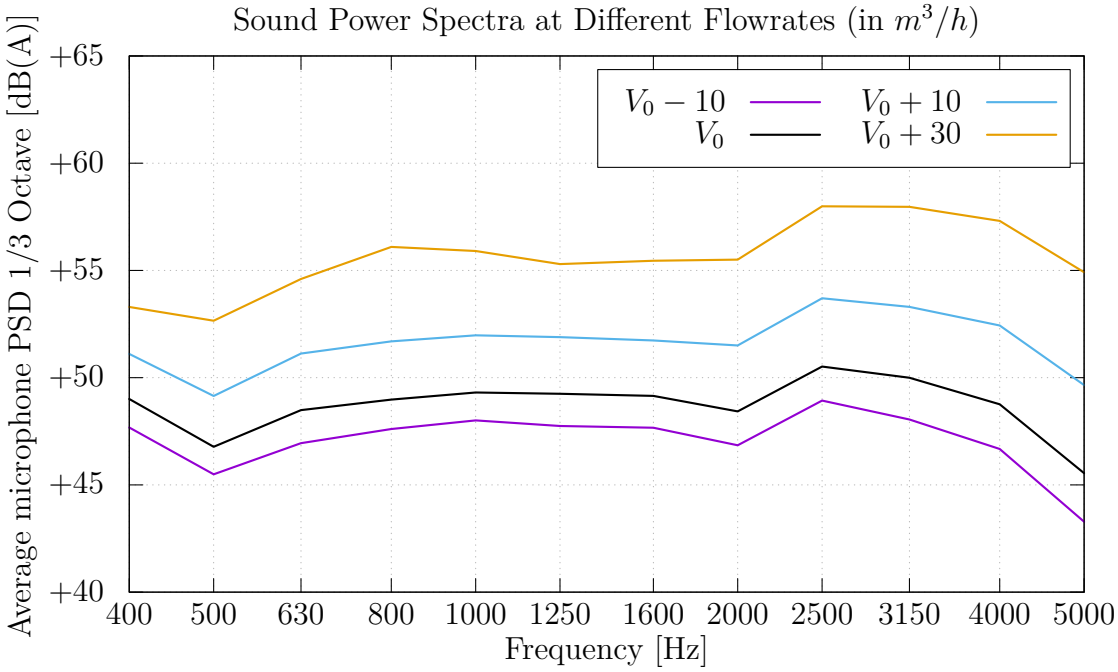

Σχήμα 6: Ηχητικό φάσμα 1/3 Οκτάβας για μετρήσεις υπό διαφορετικές τιμές παροχής αέρα. (Κατακόρυφος άξονας σε σχετικές τιμές)

την παρούσα εργασία. Ύστερα, εφαρμόζεται στην προαναφερθείσα πραγματική γεωμετρία και τα αποτελέσματα συγκρίνονται με τις μετρήσεις που έγιναν χρησιμοποιώντας την προαναφερθείσα πειραματική διάταξη.

5.1 Απλοποιημένος αγωγός συστήματος κλιματισμού

Η διάταξη αποτελείται από έναν τετραγωνικής διατομής αγωγό σε σχήμα L (σχ. 7), ο οποίος διαθέτει ένα πτερύγιο προσαρμοσμένο στο οριζόντιο τμήμα του, σε γωνία 30°.

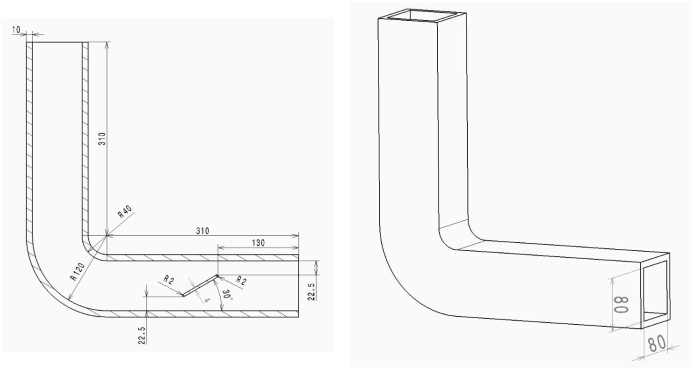

Σχήμα 7: Η γεωμετρία του απλοποιημένου αγωγού. (Σχέδιο από [13], μήκη σε mm)

Αέρας εισέρχεται από την πάνω πλευρά με μέση ταχύτητα ίση με $\overline{U} = 7.5\,\mathrm{m/s}$ και εκβάλλει από τη διατομή εξόδου, κατάντι της οποίας είχαν τοποθετηθεί 289 μικρόφωνα (σχ. 8), στη σχετική δημοσιευμένη έρευνα [13, 18]. Οι διαθέσιμες μετρήσεις αφορούν τον μέσο όρο των φασμάτων ηχητικής ισχύος όλων των μικροφώνων, μέχρι τη συχνότητα των 2 kHz.

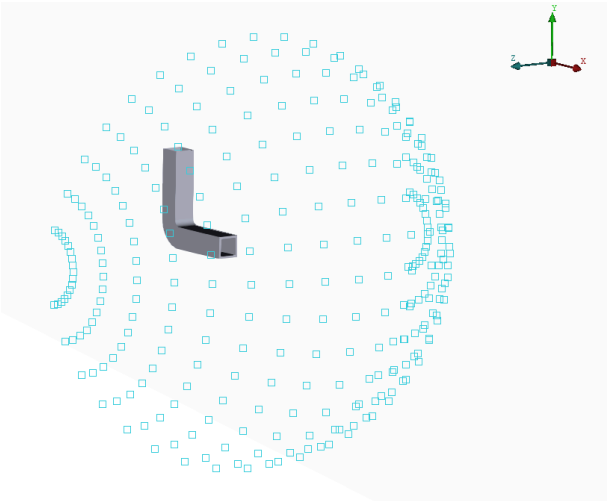

Σχήμα 8: Οι θέσεις λήψης των σημάτων πίεσης, όπως ορίστηκαν στην [13], σχηματίζουν έναν σφαιρικό θόλο με ακτίνα $1m$ από τη διατομή εξόδου του αγωγού.

Το υπολογιστικό χωρίο ορίζεται κατασκευάζοντας τον χώρο για την εκροή του αέρα και την τοποθέτηση των σημειακών δειγματοληπτών της πίεσης ενώ επεκτείνεται επίσης η διατομή εισόδου κατά 0.5 m (σχ. 9). Ο ορισμός και η γένεση του υπολογιστικού πλέγματος πραγματοποιείται βάσει ορισμένων κριτηρίων για την ικανοποιητική αποτύπωση του τυρβώδους χαρακτήρα της ροής και της διάδοσης των διαταραχών της πίεσης ως τις θέσεις των μικροφώνων. Το πεδίο ροής αρχικοποιείται μέσω της επίλυσης των εξισώσεων RANS για μόνιμη ροή και, στη συνέχεια, πραγματοποιείται η μη-μόνιμη προσομοίωση, με σταθερό χρονικό βήμα ίσο με $\Delta t = 2.5 \times 10^{-5}$ s, για 0.4 s. Για περισσότερες λεπτομέρειες σχετικά με τη διαδικασία, ο αναγνώστης παραπέμπεται στο υποκεφάλαιο 6.1 του πρωτοτύπου.

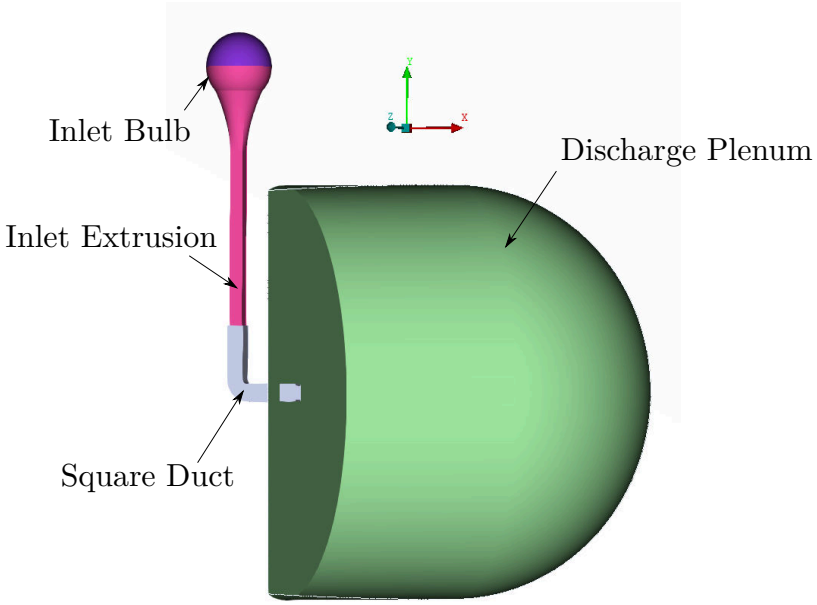

Σχήμα 9: Επιμέρους τμήματα για τον σχηματισμό ενός πεπερασμένου κλειστού υπολογιστικού χωρίου.

Στο σχ. 10 παρουσιάζεται η σύγκριση του υπολογιζόμενου φάσματος ηχητικής ισχύος, με τις μετρήσεις που ελήφθησαν από την [14]. Όπως φαίνεται, τα δύο φάσματα είναι

σε κοντινές τιμές έως περίπου τα 1000 Hz, ενώ παρατηρείται ασυμφωνία στη θέση των κορυφών στα 1200 και 1500 Hz, αντίστοιχα. Η αστοχία αυτή αφορά το τμήμα της προσομοίωσης της ροής, καθώς το χρησιμοποιούμενο λογισμικό για τη μετα-επεξεργασία των ηχητικών σημάτων, ελέγχθηκε για την ακρίβειά του, μέσω σύγκρισης με εμπορικό λογισμικό. Μία ακόμα παρατήρηση είναι πως το προβλεπόμενο φάσμα φαίνεται να είναι όμοιο με το πειραματικό, αλλά μετατοπισμένο ως εάν οι συχνότητές του έχουν πολλαπλασιαστεί με σταθερό συντελεστή μικρότερο της μονάδας. Οι αιτίες δεν έχουν εξακριβωθεί. Ωστόσο, η πρόβλεψη της γενικής τάσης του φάσματος μέχρι τα 1000 Hz είναι ικανοποιητική.

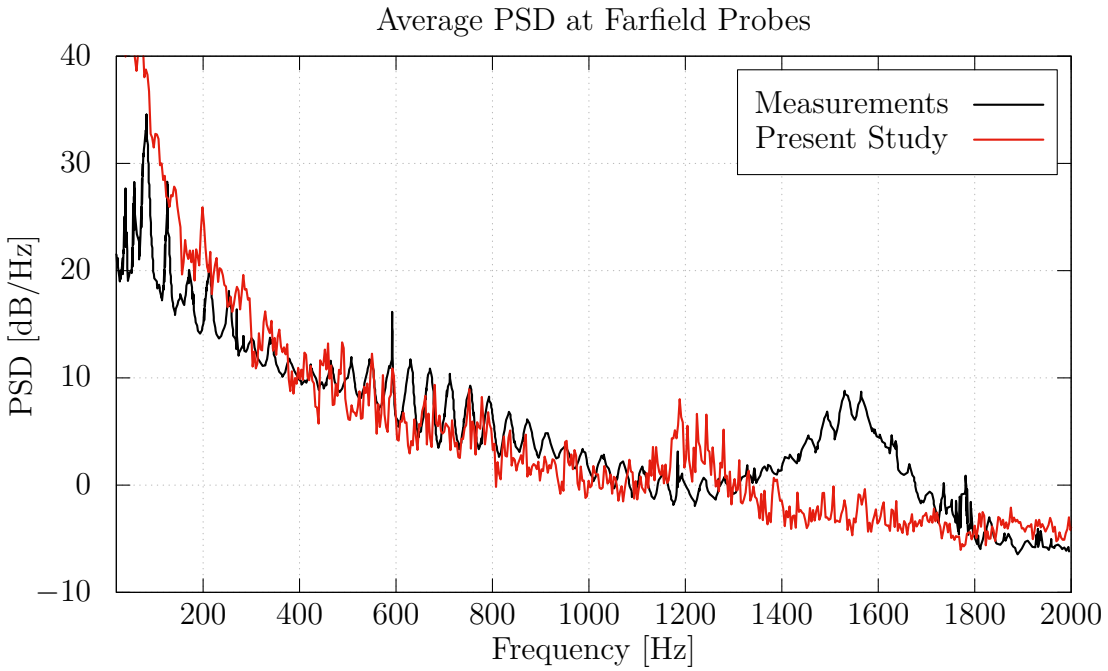

Σχήμα 10: Μέσο φάσμα ηχητικής ισχύος για όλα τα μικρόφωνα όπως προέκυψε από την αριθμητική μέθοδο, σε σύγκριση με μετρήσεις δημοσιευμένες στην [14]. (Χωρίς A-Στάθμιση)

5.2 Αγωγός επιβατικού αυτοκινήτου

Εδώ μελετάται η συμπεριφορά της μεθόδου σε γεωμετρίες βιομηχανικού ενδιαφέροντος. Για αυτόν τον σκοπό, χρησιμοποιείται η ίδια γεωμετρία (σχ. 3) στην οποία πραγματοποιήθηκαν μετρήσεις. Προσομοιώθηκαν τρεις διαφορετικές καταστάσεις λειτουργίας, με διαθέσιμες σχετικές πειραματικές μετρήσεις, για διαφορετική παροχή και κλίση των πτερυγίων των περσίδων του αγωγού, οι οποίες συνοψίζονται στο σχ. 11.

Το υπολογιστικό χωρίο και πλέγμα ορίζονται σύμφωνα με όσα αναφέρθηκαν στην προηγούμενη εξεταζόμενη περίπτωση, αυτήν τη φορά για μέγιστη απαιτούμενη συχνότητα ίση με 5000 Hz. Η προσομοίωση για κάθε περίπτωση πραγματοποιείται για 0.3 s χρόνου ροής με σταθερό χρονικό βήμα $\Delta t = 2.5 \times 10^{-5}$ s, έχοντας προηγηθεί μία προσομοίωση μόνιμης ροής (επίλυση εξισώσεων RANS) για την αρχικοποίηση του πεδίου. Οι χρονοσειρές της πίεσης λαμβάνονται σε θέσεις που αντιστοιχούν στα μικρόφωνα των αντίστοιχων πειραματικών μετρήσεων. Ολόκληρη η διαδικασία περιγράφεται αναλυτικά στο υποκεφάλαιο 6.2 του πρωτότυπου κειμένου.

Η σύγκριση των αριθμητικών φασμάτων με τα πειραματικά, σε μορφή 1/3 Οκτάβας (βλέπε παράρτημα A) παρουσιάζεται στο σχ. 12. Τα αριθμητικά αποτελέσματα για τις

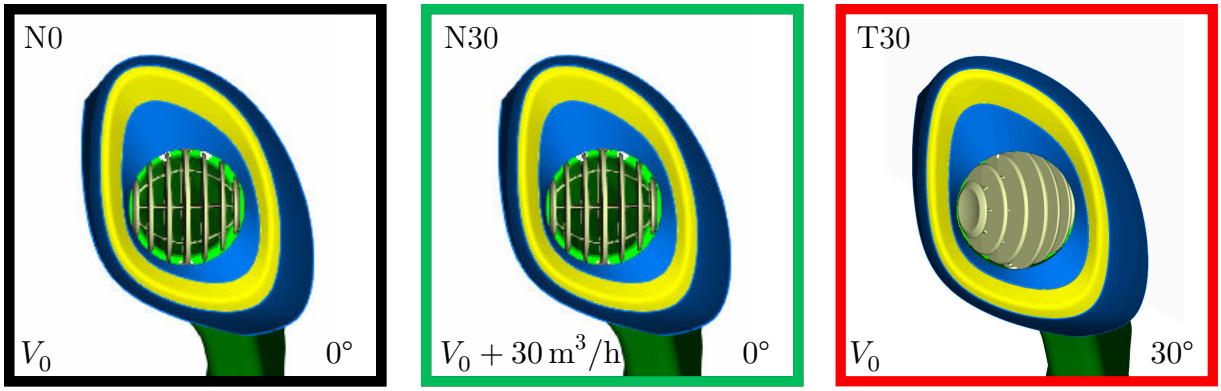

Σχήμα 11: Οι τρεις καταστάσεις που προσομοιώθηκαν πειραματικά. Πάνω αριστερά η κωδική ονομασία, κάτω δεξιά η γωνία των πτερυγίων και κάτω αριστερά η ογκομετρική παροχή σε m^3/h.

περιπτώσεις N0 και N30 ακολουθούν την ίδια τάση με τα πειραματικά, καθ' όλο το εύρος συχνοτήτων, με απόκλιση ±4dB έως τα 2000 Hz, με αυξανόμενες όμως αποκλίσεις σε μεγαλύτερες συχνότητες. Αντίθετα, στην περίπτωση της περιεστραμμένης κατά 30° διάταξης, οι αποκλίσεις αυξάνονται.

Για τη διερεύνηση της τελευταίας παρατήρησης, πραγματοποιείται η προσομοίωση μίας νέας διάταξης, της T32, στην οποία οι περσίδες έχουν στραφεί κατά 32°. Όπως φαίνεται στο σχ. 12, η νέα διάταξη παρουσιάζει πολύ καλύτερη συσχέτιση με τις μετρήσεις που αντιστοιχούσαν στην T30. Αυτό μπορεί να οφείλεται είτε σε ανακρίβειες της θέσης της γωνίας των περσίδων πριν τη μέτρηση, είτε σε γενικευμένη αδυναμία του υπολογιστικού κώδικα να προβλέψει τον ήχο σε περιοχές αυξημένης ταχύτητας ροής, όπως στην εν λόγω διάταξη. Η γενική ελλειμματική πρόβλεψη της έντασης του ήχου στις μεγαλύτερες των 2000 Hz συχνότητες εικάζεται πως οφείλεται σε ανεπαρκή διακριτοποίηση του χωρίου. Ωστόσο, σε μικρότερες συχνότητες τα επίπεδα του προβλεπόμενου ήχου ακολουθούν ικανοποιητικά τις πειραματικές μετρήσεις ακόμα και σε περιπτώσεις αλλαγής των συνθηκών λειτουργίας, όπως με αύξηση της παροχής και στροφής των περσίδων.

6 Συμπεράσματα

Η μέθοδος άμεσου υπολογισμού θορύβου εφαρμόστηκε με επιτυχία μέσω του περιβάλλοντος OpenFOAM και τα αποτελέσματα των υπολογισμένων σταθμών ήχου είναι συγκρίσιμα με τα πειραματικά.

Στην περίπτωση του απλοποιημένου αγωγού παρατηρήθηκαν ανακρίβειες στις συχνότητες μεμονωμένων κορυφών του φάσματος, που μάλλον οφείλονται στη διαδικασία επίλυσης των εξισώσεων ροής. Ακόμα, παρατηρήθηκε αδυναμία για πρόβλεψη ήχου σε συχνότητες μεγαλύτερες των 2000 Hz, πιθανόν λόγω ανεπαρκούς χωρικής διακριτοποίησης του χωρίου.

Η μέθοδος δύναται να προβλέψει ικανοποιητικά τα επίπεδα του αεροδυναμικού ήχου σε χαμηλές συχνότητες, έως τα 1000-2000 Hz. Ακόμα, η εφαρμογή στον αγωγό επιβατικού αυτοκινήτου έδειξε πως η γενική τάση του ηχητικού φάσματος που προκύπτει λόγω αλλαγών στη γεωμετρία και στις συνθήκες λειτουργίας ακολουθείται και από τα αριθμητικά αποτελέσματα.

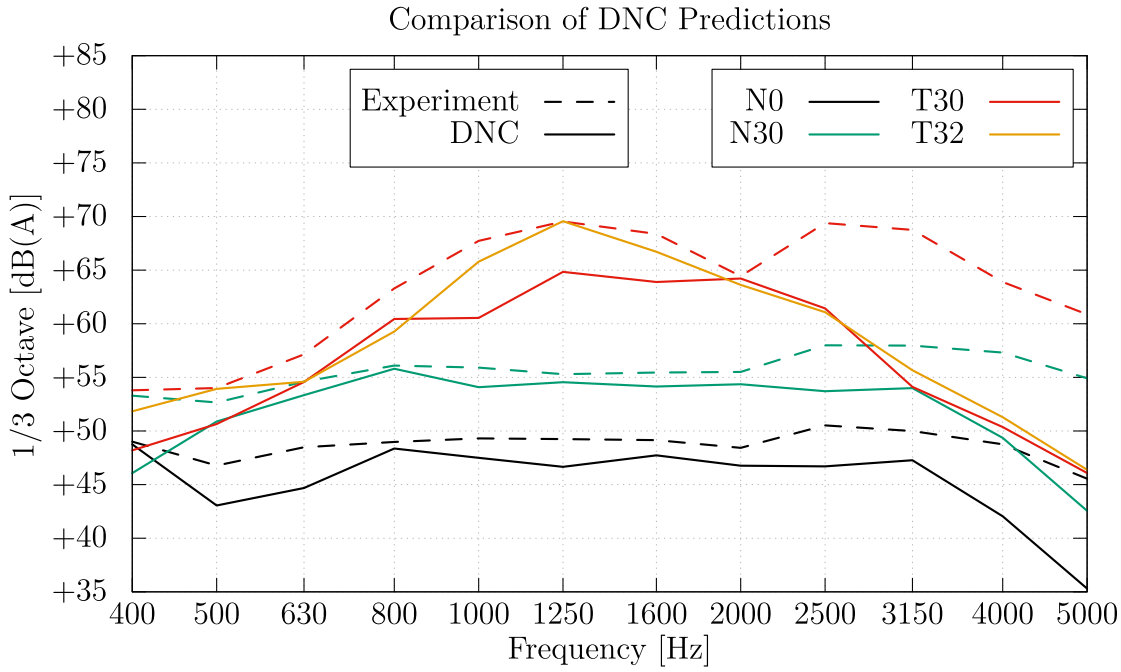

Σχήμα 12: Σύγκριση μεταξύ πειραματικών (διακεκομμένες) και αριθμητικών προβλέψεων (συμπαγείς). Κάθε χρώμα αντιστοιχεί σε διαφορετική διάταξη. (Κατακόρυφος άξονας με σχετικές τιμές)

Bibliography

[1] S. Bennouna, T. Matharan, and O. Cheriaux, "Automotive HVAC noise reduction", in *SAE Technical Paper Series*, SAE International, Jun. 2018. DOI: 10.4271/2018-01-1519.

[2] V. Madani and S. Ziada, "Aeroacoustic characteristics of automotive HVAC systems", SAE Technical Paper, Tech. Rep. 2008-01-0406, Apr. 2008. DOI: 10.4271/2008-01-0406.

[3] M. Li and L. Huang, "CFD design tool improves HVAC design and cuts product development cycle time", *SAE International Journal of Passenger Cars - Mechanical Systems*, vol. 1, no. 1, pp. 150–155, Apr. 2008. DOI: 10.4271/2008-01-0238.

[4] M. Kaltenbacher, *Computational Acoustics*, M. Kaltenbacher, Ed. Springer International Publishing, Jul. 2018, vol. 27, pp. 22–23, 251 pp., ISBN: 978-3-319-59038-7. DOI: 10.1007/978-3-319-59038-7.

[5] W. D. Stewart Glegg, *Aeroacoustics of Low Mach Number Flows: Fundamentals, Analysis and Measurement, Fundamentals, Analysis and Measurement*. Academic Press Elsevier, 2017, pp. 76, 89–90, 254–261, ISBN: 9780128096512. DOI: 10.1016/b978-0-12-809651-2.00011-4.

[6] M. Sah, K. Srinivasan, F. Mendonca, *et al.*, "Prediction of HVAC system aero/acoustic noise generation and propagation using CFD", in *SAE Technical Paper Series*, SAE International, Apr. 2013. DOI: 10.4271/2013-01-0856.

[7] ISO 389-7:2005, "Acoustics – Reference zero for the calibration of audiometric equipment. Part 7: Reference threshold of hearing under free-field and diffuse-field listening conditions", International Organization for Standardization, Geneva, CH, Standard, Nov. 2005. [Online]. Available: https://www.iso.org/standard/38976.html.

[8] M. C. Killion, "Revised estimate of minimum audible pressure: Where is the missing 6 dB?", *The Journal of the Acoustical Society of America*, vol. 63, no. 5, pp. 1501–1508, 1978. DOI: 10.1121/1.381844.

[9] J. C. Hardin and M. Y. Hussaini, *Computational Aeroacoustics*. Springer, 2012, pp. 52–54, ISBN: 9781461383444. DOI: 10.1007/978-1-4613-8342-0.

[10] C. Wagner, T. Hüttl, and P. Sagaut, *Large-Eddy Simulation for Acoustics*. Cambridge University Press, 2007, vol. 20, pp. 7–14, 59–60, 89–90, 218–220, 222–225, 360–362, ISBN: 978-0-511-29466-2.

[11] M. Wang, J. B. Freund, and S. K. Lele, "Computational prediction of flow - generated sound", *Annual Review of Fluid Mechanics*, vol. 38, no. 1, pp. 483–512, Jan. 2006. DOI: 10.1146/annurev.fluid.38.050304.092036.

[12] M. Tautz, "Aeroacoustic noise prediction of automotive HVAC systems", en, PhD thesis, FAU Forschungen, 2019, pp. 27, 114. DOI: 10.25593/978-3-96147-216-1.

[13] A. Jäger, F. Decker, M. Hartmann, *et al.*, "Numerical and experimental investigations of the noise generated by a flap in a simplified HVAC duct", in *14th AIAA/CEAS Aeroacoustics Conference (29th AIAA Aeroacoustics Conference)*, American Institute of Aeronautics and Astronautics, May 2008. DOI: 10.2514/6.2008-2902.

[14] A. Kierkegaard, A. West, and S. Caro, "HVAC noise simulations using direct and hybrid methods", in *22nd AIAA/CEAS aeroacoustics conference*, American Institute of Aeronautics and Astronautics, May 2016, p. 2855. DOI: 10.2514/6.2016-2855.

[15] P. Martínez-Lera, R. Hallez, H. Beriot, *et al.*, "Computation of sound in a simplified HVAC duct based on aerodynamic pressure", in *18th AIAA/CEAS Aeroacoustics Conference (33rd AIAA Aeroacoustics Conference)*, American Institute of Aeronautics and Astronautics, Jun. 2012. DOI: 10.2514/6.2012-2070.

[16] S. Caro, Y. Detandt, J. Manera, *et al.*, "Validation of a new hybrid CAA strategy and application to the noise generated by a flap in a simplified HVAC duct", in *15th AIAA/CEAS Aeroacoustics Conference (30th AIAA Aeroacoustics Conference)*, American Institute of Aeronautics and Astronautics, May 2009, p. 3352. DOI: 10.2514/6.2009-3352.

[17] C. C. D. Wiart, P. Geuzaine, Y. Detandt, *et al.*, "Validation of a hybrid CAA method: Noise generated by a flap in a simplifed HVAC duct", in *16th AIAA/CEAS Aeroacoustics Conference*, American Institute of Aeronautics and Astronautics, Jun. 2010. DOI: 10.2514/6.2010-3995.

[18] F. Pérot, M. Meskine, and J. Ocker, "Direct flow-induced noise prediction of a simplified HVAC duct using a Lattice Boltzmann method", May 2013. DOI: 10.2514/6.2013-2265.

[19] E. Gren, M. Farrall, F. Mendonça, *et al.*, "CFD prediction of aeroacoustic noise generation in a HVAC duct", in *18th AIAA/CEAS Aeroacoustics Conference (33rd AIAA Aeroacoustics Conference)*, American Institute of Aeronautics and Astronautics, Jun. 2012. DOI: 10.2514/6.2012-2068.

[20] F. Pérot, M. Meskine, V. LeGoff, *et al.*, "HVAC noise predictions using a Lattice Boltzmann method", May 2013. DOI: 10.2514/6.2013-2228.

[21] O. M. Mohamud and P. Johnson, "Broadband noise source models as aeroacoustic tools in designing low NVH HVAC ducts", SAE Technical Paper, Tech. Rep. 2006-01-1192, Apr. 2006. DOI: 10.4271/2006-01-1192.

[22] *OpenFOAM: User Guide v2112*, OpenCFD Ltd, Dec. 2021. [Online]. Available: https://www.openfoam.com/documentation/guides/v2112/doc/.

[23] A. D. Pierce, *Acoustics*. Springer-Verlag GmbH, Jun. 2019, pp. 18–20, 768 pp., ISBN: 978-3-030-11214-1.

[24] T. D. Rossing, *Springer Handbook of Acoustics*, 2nd ed., T. D. Rossing, Ed. Springer, 2014, pp. 51–52, 183–185, 1005–1010, ISBN: 978-1-4939-0754-0. DOI: 10.1007/978-1-4939-0755-7.

[25] F. Fahy, *Foundations of engineering acoustics*. Academic, 2001, pp. 98–103, 406–410, ISBN: 0122476654.

[26] A. N. Kolmogorov, "The local structure of turbulence in incompressible viscous fluid for very large Reynolds numbers", *Proceedings of the Royal Society of London. Series A: Mathematical and Physical Sciences*, vol. 434, no. 1890, pp. 9–13, Jul. 1991. DOI: 10.1098/rspa.1991.0075.

[27] M. J. Lighthill, "On sound generated aerodynamically I. General theory", *Proceedings of the Royal Society of London. Series A. Mathematical and Physical Sciences*, vol. 211, no. 1107, pp. 564–587, Mar. 1952. DOI: 10.1098/rspa.1952.0060.

[28] N. Curle, "The influence of solid boundaries upon aerodynamic sound", *Proceedings of the Royal Society of London. Series A. Mathematical and Physical Sciences*, vol. 231, no. 1187, pp. 505–514, Sep. 1955. DOI: 10.1098/rspa.1955.0191.

[29] P. Martínez-Lera, C. Schram, H. Bériot, *et al.*, "An approach to aerodynamic sound prediction based on incompressible-flow pressure", *Journal of Sound and Vibration*, vol. 333, no. 1, pp. 132–143, Jan. 2014. DOI: 10.1016/j.jsv.2013.08.033.

[30] P. Martínez-Lera, K. Kucukcoskun, M. Shur, *et al.*, "Hybrid aeroacoustic computations for flows in ducts with single and tandem diaphragms", in *22nd AIAA/CEAS Aeroacoustics Conference*, American Institute of Aeronautics and Astronautics, May 2016. DOI: 10.2514/6.2016-2796.

[31] Y. Khalighi, A. Mani, F. Ham, *et al.*, "Prediction of sound generated by complex flows at low Mach numbers", *AIAA Journal*, vol. 48, no. 2, pp. 306–316, Feb. 2010. DOI: 10.2514/1.42583.

[32] P. Martínez-Lera, R. Hallez, M. Tournour, *et al.*, "Improved simulation technique for predicting the noise radiated by a flap in a simplified HVAC duct", in *JSAE Annual Congress*, vol. 20115259, 2011, p. 20.

[33] N. Papaxanthos, E. Perrey-Debain, S. Bennouna, *et al.*, "Pressure-based integral formulations of Lighthill-Curle's analogy for internal aeroacoustics at low Mach numbers", *Journal of Sound and Vibration*, vol. 393, pp. 176–186, Apr. 2017. DOI: 10.1016/j.jsv.2017.01.030.

[34] P. Martínez-Lera, "Modeling of aerodynamic noise production and flow-acoustic feedback for wall-bounded low Mach number flows", PhD thesis, Katholieke Universiteit Leuven – Faculty of Engineering, Leuven, Belgium, Aug. 2010, pp. 61–75, 77–69, ISBN: 9789460182365.

[35] C. Bailly, C. Bogey, and O. Marsden, "Progress in direct noise computation", *International Journal of Aeroacoustics*, vol. 9, no. 1-2, pp. 123–143, Jan. 2010. DOI: 10.1260/1475-472X.9.1-2.123.

[36] A. H. Dawi and R. A. Akkermans, "Spurious noise in direct noise computation with a finite volume method for automotive applications", *International Journal of Heat and Fluid Flow*, vol. 72, pp. 243–256, Aug. 2018. DOI: 10.1016/j.ijheatfluidflow.2018.06.008.

[37] F. Moukalled, L. Mangani, and M. Darwish, *The Finite Volume Method in Computational Fluid Dynamics, An Advanced Introduction with OpenFOAM® and Matlab*. Springer International Publishing, 2016, pp. 57–64, 621–627, 722–723, ISBN: 9783319168746. DOI: 10.1007/978-3-319-16874-6.

[38] P. Sagaut, *Large Eddy Simulation for Incompressible Flows*. Springer Berlin Heidelberg, 2002, pp. 1–8, ISBN: 978-3-662-04697-5. DOI: 10.1007/978-3-662-04695-1.

[39] B. Chaouat, "The state of the art of hybrid RANS/LES modeling for the simulation of turbulent flows", *Flow, Turbulence and Combustion*, vol. 99, no. 2, pp. 279–327, Jul. 2017. DOI: 10.1007/s10494-017-9828-8.

[40] S.-H. Peng, P. Doerffer, and W. Haase, Eds., *Progress in Hybrid RANS-LES Modelling*. Springer Berlin Heidelberg, 2010, pp. 58–73. DOI: 10.1007/978-3-642-14168-3.

[41] U. Piomelli and E. Balaras, "Wall-layer models for large-eddy simulations", *Annual Review of Fluid Mechanics*, vol. 34, no. 1, pp. 349–374, Jan. 2002. DOI: 10.1146/annurev.fluid.34.082901.144919.

[42] P. R. Spalart, W.-H. Jou, M. Strelets, *et al.*, "Comments on the feasibility of LES for wings, and on a hybrid RANS/LES approach", in *Advances in DNS/LES: Direct numerical simulation and large eddy simulation*, Greyden Press, Colombus, OH, USA, 1997, pp. 137–148.

[43] T. M. Farabee and M. J. Casarella, "Spectral features of wall pressure fluctuations beneath turbulent boundary layers", *Physics of Fluids A: Fluid Dynamics*, vol. 3, no. 10, pp. 2410–2420, Oct. 1991. DOI: 10.1063/1.858179.

[44] M. S. Gritskevich, A. V. Garbaruk, J. Schütze, *et al.*, "Development of DDES and IDDES formulations for the k-ω shear stress transport model", *Flow, Turbulence and Combustion*, vol. 88, no. 3, pp. 431–449, Nov. 2011. DOI: 10.1007/s10494-011-9378-4.

[45] F. Menter and T. Esch, "Elements of industrial heat transfer predictions", in *16th Brazilian Congress of Mechanical Engineering (COBEM)*, vol. 109, 2001, p. 650.

[46] M. L. Shur, P. R. Spalart, M. K. Strelets, *et al.*, "A hybrid RANS-LES approach with delayed-DES and wall-modelled LES capabilities", *International Journal of Heat and Fluid Flow*, vol. 29, no. 6, pp. 1638–1649, Dec. 2008. DOI: 10.1016/j.ijheatfluidflow.2008.07.001.

[47] H. Nyquist, "Certain topics in telegraph transmission theory", *Transactions of the American Institute of Electrical Engineers*, vol. 47, no. 2, pp. 617–644, Apr. 1928. DOI: 10.1109/T-AIEE.1928.5055024.

[48] P. Welch, "The use of fast Fourier transform for the estimation of power spectra: A method based on time averaging over short, modified periodograms", *IEEE Transactions on Audio and Electroacoustics*, vol. 15, no. 2, pp. 70–73, Jun. 1967. DOI: 10.1109/TAU.1967.1161901.

[49] F. Harris, "On the use of windows for harmonic analysis with the discrete Fourier transform", *Proceedings of the IEEE*, vol. 66, no. 1, pp. 51–83, 1978. DOI: 10.1109/PROC.1978.10837.

[50] IEC 61672-1:2013, "Electroacoustics - Sound level meters - Part 1: Specifications", International Electrotechnical Commission, Geneva, CH, Standard, Sep. 2013. [Online]. Available: https://webstore.iec.ch/publication/5708.

[51] Y. He, S. Schröder, Z. Shi, *et al.*, "Wind noise source filtering and transmission study through a side glass of DrivAer model", *Applied Acoustics*, vol. 160, p. 107 161, Mar. 2020. DOI: 10.1016/j.apacoust.2019.107161.

[52] F. van Herpe, S. Vergne, and E. Gaudard, "Wavenumber-frequency analysis of the wall pressure fluctuations in the wake of a rear view mirror using a Lattice Boltzmann model", in *Acoustics 2012*, S. F. d'Acoustique, Ed., Nantes, France, Apr. 2012. [Online]. Available: https://hal.archives-ouvertes.fr/hal-00810780.

[53] D. G. Crighton, A. P. Dowling, J. E. F. Williams, *et al.*, *Modern Methods in Analytical Acoustics*. Springer London, 1992, pp. 323–324. DOI: 10.1007/978-1-4471-0399-8.

[54] P. Virtanen, R. Gommers, T. E. Oliphant, *et al.*, "SciPy 1.0: Fundamental Algorithms for Scientific Computing in Python", *Nature Methods*, vol. 17, pp. 261–272, 2020. DOI: 10.1038/s41592-019-0686-2.

[55] S. P. Mavuri, S. Watkins, X. Wang, *et al.*, "An investigation of vehicle HVAC cabin noise", SAE Technical Paper, Tech. Rep. 2008-01-0836, Apr. 2008. DOI: 10.4271/2008-01-0836.

[56] X. Wang, *Vehicle noise and vibration refinement*. CRC Press, 2010, pp. 68–92, ISBN: 9781439831335.

[57] IEC 61260-1:2014, "Electroacoustics - Octave-band and fractional-octave-band filters - Part 1: Specifications", International Electrotechnical Commission, Geneva, CH, Standard, Feb. 2014. [Online]. Available: https://webstore.iec.ch/publication/5063.